

**The First measurements of J/ψ production in proton-proton collisions at $\sqrt{s}=13$ TeV and study of the $B \rightarrow \mu\mu\pi\pi$ decays at LHCb:
two tests of QCD predictions**

THÈSE N° 7081 (2016)

PRÉSENTÉE LE 15 JUILLET 2016

À LA FACULTÉ DES SCIENCES DE BASE
LABORATOIRE DE PHYSIQUE DES HAUTES ÉNERGIES 3
PROGRAMME DOCTORAL EN PHYSIQUE

ÉCOLE POLYTECHNIQUE FÉDÉRALE DE LAUSANNE

POUR L'OBTENTION DU GRADE DE DOCTEUR ÈS SCIENCES

PAR

Ilya KOMAROV

acceptée sur proposition du jury:

Prof. F. Mila, président du jury
Prof. T. Nakada, directeur de thèse
Prof. S. Hansmann-Menzemer, rapporteuse
Prof. F. Forti, rapporteur
Prof. C. Grab, rapporteur



ÉCOLE POLYTECHNIQUE
FÉDÉRALE DE LAUSANNE

Suisse
2016

Acknowledgements

A doctoral thesis is a document which has only one name in its author list but, in fact, should be authored by many people. Here I would like to remedy this blatant injustice as much as I can, and thank people who made this work possible.

First of all, I really appreciate my thesis director, professor Nakada, for his supervision during these four years. Under his guidance, I felt a taste of independent research, but always had a strong support in case of need.

I would like to thank all Swiss people for creation of society which respects science, in word and in deed. I would like to thank professors Tatsuya Nakada, Aurelio Bay and Olivier Schneider for brilliantly heading the laboratory of the High Energy Physics (LPHE) at EPFL, and for giving me a chance to join their team as a doctoral student. Many thanks to our secretaries, Erika Luthi and Esther Hoffman, for their great organisation of work and for bringing a warming atmosphere to the laboratory. Thanks to all my friends and colleagues at LPHE for maintaining a very friendly, family-like environment.

I would like to acknowledge the great spirit of LHCb people, and sincerely thank those of them who worked closely with me during these years. I am proud to call you my colleagues, and happy to call you my friends. Thanks to Yanxi and Svende for a great time of working on early measurement analysis, I will never forget this epic action. To Nikolai Victorovich for the help with the theory of rare decays and good, friendly advices. To Elena for her enthusiasm in the implementation of the new ST software and her help with the writing of the internal note. To Mark and Maurizio for their support during the work on the tracker. Many thanks to Fred Blanc for his support, advices and good ideas in a very wide range of topics. Being limited in space, I can't list here all of my LHCb friends, but I should stress the fact that it was a honor and pleasure to be part of this collaboration during my doctoral studies.

I want to express especial acknowledgement to people who did the hard job of helping me with the editing of this manuscript. Mark, Fred and Preema - thank you for your patient fixing of my grammatical errors, and all those "a" and "the" I lost in the first drafts. Thanks to Violaine for her help with the french version of the abstract. Many thanks to Francesco Forti and Diego Tonelli for their patient reading and useful comments to the text, which improved a lot this manuscript.

Acknowledgements

I would like to give a cordial thanks to Mirco Dorigo, my colleague and friend. He played a huge role in the search for rare decays presented here and spent enormous efforts helping me to improve this thesis. His door was always open for me, and he was always ready to help me with any questions. Many thanks, Mirco.

Finally, I would like to express my gratitude to my family, who give me very strong support in my obsession for physics and make me proud of my work. Mother and Father, Nina, Kolya and Vitya, even through miles which separate us, your love is warming my heart and gives me strength to live and work, thank you.

Inna, my beloved wife, you are my blessing and my inspiration. Without you nothing would have any sense. Thank you, my dear Inna.

Lausanne, 1 Juillet 2016

I. K.

Abstract

We present a search for the $B_s^0 \rightarrow \pi^+ \pi^- \mu^+ \mu^-$ and $B^0 \rightarrow \pi^+ \pi^- \mu^+ \mu^-$ decays using data collected by the LHCb detector in proton-proton collisions at centre-of-mass energies of 7 and 8 TeV and corresponding to an integrated luminosity of 3 fb^{-1} . We obtain the first observation of the $B_s^0 \rightarrow \pi^+ \pi^- \mu^+ \mu^-$ decay with a statistical significance of 7.2σ and the first evidence of the $B^0 \rightarrow \pi^+ \pi^- \mu^+ \mu^-$ decay with a statistical significance of 4.8σ . The branching ratios of these decays are measured to be $\mathcal{B}(B_s^0 \rightarrow \pi^+ \pi^- \mu^+ \mu^-) = (8.6 \pm 1.5 \text{ (stat)} \pm 0.7 \text{ (syst)} \pm 0.7 \text{ (norm)}) \times 10^{-8}$ and $\mathcal{B}(B^0 \rightarrow \pi^+ \pi^- \mu^+ \mu^-) = (2.11 \pm 0.51 \text{ (stat)} \pm 0.15 \text{ (syst)} \pm 0.16 \text{ (norm)}) \times 10^{-8}$, where the third uncertainty is due to the branching fraction of the decay $B^0 \rightarrow J/\psi (\rightarrow \mu^+ \mu^-) K^*(892)^0 (\rightarrow K^+ \pi^-)$, used as a normalisation.

We present also the first measurement of the production cross-section of J/ψ mesons in proton-proton collisions at centre-of-mass energy of 13 TeV using the data collected by LHCb in 2015 and corresponding to an integrated luminosity of $3.02 \pm 0.12 \text{ pb}^{-1}$. The production cross-section is measured as a function of the transverse momentum p_T and the rapidity y of the J/ψ meson in the region $p_T < 14 \text{ GeV}/c$ and $2.0 < y < 4.5$, for both prompt J/ψ mesons and J/ψ mesons from b -hadron decays. The production cross-sections integrated over the kinematic coverage are found to be $15.30 \pm 0.03 \text{ (stat)} \pm 0.86 \text{ (syst)} \mu\text{b}$ for prompt J/ψ and $2.34 \pm 0.01 \text{ (stat)} \pm 0.13 \text{ (syst)} \mu\text{b}$ for J/ψ from b -hadron decays, assuming zero polarisation of the J/ψ meson. The ratios between these cross sections and the ones measured at the centre-of-mass-energy of 8 TeV are also determined and compared with theoretical expectations. This measurement also validated a novel approach for online collection of ready-to-use data, which was implemented for the first time.

The study of the performances of the Silicon Tracker of the LHCb experiment during the 2012 and 2015 years of operation is also reported, and my contribution to a novel monitoring system of this sub-detector is presented.

Key words: LHC, LHCb, particle physics, heavy flavour, b hadrons, rare decays, silicon detectors, alignment, performance, monitoring, charmonium, QCD

Résumé

Nous présentons les recherches des désintégrations $B_s^0 \rightarrow \pi^+ \pi^- \mu^+ \mu^-$ et $B^0 \rightarrow \pi^+ \pi^- \mu^+ \mu^-$ en utilisant les données recueillies par le détecteur LHCb dans les collisions proton-proton à des énergies dans le centre de masse de 7 et 8 TeV et correspondant à une luminosité intégrée de 3 fb^{-1} . On obtient la première observation des désintégrations $B_s^0 \rightarrow \pi^+ \pi^- \mu^+ \mu^-$ avec une signifiante statistique de $7,2\sigma$, et une indication de désintégration $B^0 \rightarrow \pi^+ \pi^- \mu^+ \mu^-$ avec une signifiante statistique de $4,8\sigma$. Les mesures des taux d'embranchement pour ces décroissances ont donné respectivement $\mathcal{B}(B_s^0 \rightarrow \pi^+ \pi^- \mu^+ \mu^-) = (8,6 \pm 1,5 \text{ (stat)} \pm 0,7 \text{ (syst)} \pm 0,7 \text{ (norm)}) \times 10^{-8}$ et $\mathcal{B}(B^0 \rightarrow \pi^+ \pi^- \mu^+ \mu^-) = (2,11 \pm 0,51 \text{ (stat)} \pm 0,15 \text{ (syst)} \pm 0,16 \text{ (norm)}) \times 10^{-8}$, où la troisième incertitude citée est liée au taux d'embranchement de la décroissance $B^0 \rightarrow J/\psi (\rightarrow \mu^+ \mu^-) K^* (892)^0 (\rightarrow K^+ \pi^-)$ qui est utilisée pour la normalisation.

Nous présentons aussi la première mesure de la section efficace de production des mésons J/ψ dans les collisions proton-proton avec une énergie de 13 TeV dans le centre de masse en utilisant les données recueillies par le détecteur LHCb en 2015 et correspondant à une luminosité intégrée de $3,02 \pm 0,12 \text{ pb}^{-1}$. La section efficace des J/ψ prompts et des J/ψ issus de désintégrations de hadrons b a été mesurée en fonction de la quantité de mouvement transverse p_T et de la rapidité y des mésons J/ψ dans la région $p_T < 14 \text{ GeV}/c$ et $2,0 < y < 4,5$. Les sections efficaces de production intégrées sur l'ouverture cinématique du détecteur sont $15,30 \pm 0,03 \pm 0,86 \text{ } \mu\text{b}$ pour les J/ψ prompts et $2,34 \pm 0,01 \pm 0,13 \text{ } \mu\text{b}$ pour les J/ψ issus de désintégrations de hadrons b , en faisant l'hypothèse d'une polarisation nulle pour les J/ψ . Les premières incertitudes citées sont statistiques et les secondes systématiques. Les rapports de section efficace par rapport aux résultats obtenus à $\sqrt{s} = 8 \text{ TeV}$ ont été déterminés et sont comparés aux prédictions théoriques. Cette mesure a permis de valider la nouvelle technique *Turbostream* qui a été utilisée pour la première fois dans le cadre de cette analyse.

L'étude des performances du Silicon Tracker du détecteur LHCb au cours des années 2012 et 2015 est rapportée. Un nouvel outil de contrôle de ce sous-détecteur est présenté.

Mots clefs : LHC, LHCb, physique des particules, saveurs lourdes, hadrons b , Turbostream, désintégrations rares, détecteurs au silicium, l'alignement, la performance, suivi, charmonium, QCD

Contents

Acknowledgements	i
Abstract	iii
List of figures	ix
List of tables	xv
1 Introduction	1
2 Introduction to the Standard Model	3
2.1 Flavor changing neutral currents	6
2.2 QCD effects	8
3 Overview of the LHCb detector	11
3.1 LHCb performance overview	12
3.2 Data processing	14
3.3 Simulations at LHCb	15
4 Search for $B \rightarrow \pi\pi\mu\mu$ decays	17
4.1 Introduction	17
4.1.1 Theoretical motivation	17
4.1.2 Choice of the dipion mass range	19
4.1.3 The main observables	19
4.2 Data samples and selection	20
4.2.1 Preselection	20
4.2.2 Sample composition	21
4.2.3 Selection strategy	22
4.2.4 Multivariate selection	22
4.2.5 Misidentified decays	25
4.2.6 Wrongly reconstructed decays	29
4.2.7 Selection efficiencies	30
4.3 Study of misidentified backgrounds	33
4.3.1 Selection of a clean $B^0 \rightarrow J/\psi K^*(892)^0$ sample	35
4.3.2 sWeights for further background suppression	35

Contents

4.3.3	Emulation of misidentification	35
4.3.4	Extraction of the background shape	36
4.3.5	Uncertainty of the method	37
4.4	Fits to the data	38
4.4.1	Fit to the normalisation channel	39
4.4.2	Likelihood of the $\pi\pi\mu\mu$ and $J/\psi\pi\pi$ sample	40
4.4.3	Fit results	43
4.4.4	Systematic uncertainties	47
4.5	Fit model validation	50
4.6	Pseudo-experiment studies	52
4.7	Results	53
5	Measurement of the J/ψ production cross-section	55
5.1	Introduction	55
5.2	Cross-section determination	57
5.2.1	Selection of the J/ψ candidates	58
5.2.2	Efficiency determination	59
5.2.3	Fit model	61
5.2.4	Validation of the novel data processing model	62
5.2.5	Overview of the systematic uncertainties	64
5.3	Results	68
5.3.1	Comparison with theoretical results	73
5.4	Conclusion	74
6	LHCb Silicon Tracker - Performance and monitoring	77
6.1	Performance of the LHCb ST	78
6.1.1	Description of the data sets	80
6.1.2	Results	80
6.2	ST software development	86
6.2.1	STTrackTuple algorithm	86
6.2.2	ST Interactive Map	87
6.3	ST performance monitoring	89
6.3.1	Data manager monitoring	90
6.3.2	Expert monitoring	90
7	Conclusions and Outlook	95
	Bibliography	97
	Appendices	105
A	Summary of the LHCb ST performance in 2012/2015	105
B	Numerical results of the measurement of the J/ψ production cross-section	113

C Pseudo-experiments studies in searches for $B \rightarrow \pi\pi\mu\mu$ decays	119
Curriculum Vitae	123

List of Figures

2.1	Experimental constraints for the unitarity of the CKM matrix [1].	6
2.2	Example of FCNC transitions of b quark through (a) penguin diagram with change of flavour $\Delta F = 1$ and (b) box diagram with $\Delta F = 2$	6
2.3	Summary of measurements of α_s as a function of the energy scale Q [2].	8
3.1	Layout of the LHCb detector	11
3.2	Tracking efficiency as function of the momentum, p and the total number of tracks in the event, N_{track} [3]. The error bars indicate the statistical uncertainty	12
3.3	Relative momentum resolution versus momentum for long tracks in data obtained using J/ψ decays (left) and mass resolution (σ_m) (right) as a function of the mass (m) of the dimuon resonance [3].	13
3.4	Kaon identification efficiency and pion misidentification rate as a function of track momentum [4](left) and background misidentification rates versus muon identification efficiency [3] (right).	13
3.5	Schematic diagram of the overall data processing in Run-II, where the blue solid line represents data flow, and the red dashed line the propagation of calibrations. [5]	14
3.6	Outline of the LHCb data processing. On the left in blue the processing of Monte Carlo samples, the Data Taking in orange on the right. The Reconstruction and Stripping for both the MC and the data collected by the DAQ of the experiment are in green. [6]	16
4.1	Example of (a) penguin and (b) box Feynman diagrams for $B_{(s)}^0 \rightarrow \rho(770)(f_0(980))\mu^+\mu^-$ processes.	17
4.2	Mass distributions of the resonant (left) and the signal (right) samples after the stripping selection.	23
4.3	Comparison of the BDT output for test and training distributions for 2011 (left) and 2012 (right) data sets.	24
4.4	Optimisation of the BDT cut-point for 2011 (left) and 2012 (right) data sets. The figure of merit $\varepsilon/(\alpha/2 + \sqrt{B})$ is shown with the dashed red line.	25
4.5	Left: signal efficiencies for the 2011 and 2012 BDTs selection. Right: background efficiencies for the 2011 and 2012 BDTs.	25

List of Figures

4.6	Comparison of BDT input variables distributions for data (black) and simulations (red) samples	26
4.7	Comparison of BDT output distributions for data (black) and simulations (red) samples	27
4.8	BDT output variable versus the PID criteria for the signal (left) and background (right) samples. Distribution of candidates on these plots evidence negligibly small correlation between the two variables for examined samples.	28
4.9	Distributions of MC data for partially- and over-reconstructed decays with fit projections overlaid. The left plot shows $B_s^0 \rightarrow J/\psi\phi$, the middle plot $B_s \rightarrow J/\psi\eta'$, and the right plot the $B^+ \rightarrow J/\psi K^+$ decays. The distributions are fitted with Argus functions convolved with a Gaussian with width fixed to the value found for the signal decays ($\approx 20 \text{ MeV}/c^2$).	29
4.10	Dependence of the selection efficiency (for different steps of the selection) as a function of the $\pi^+\pi^-$ mass for MC data. Here, with "preselection" we consider the $\mu^+\mu^-$ mass requirements, while the BDT is applied in the last step (Total).	33
4.11	Mass distributions of $B^0 \rightarrow J/\psi K^*(892)^0$ with fit projections overlaid (left), background PDF obtained with misidentification emulation (center) and position dependence of the yield of corresponding background to the fit of the resonance sample. All plots are obtained with for the 2012 data set.	38
4.12	Mass distributions of $B^0 \rightarrow K^*(892)^0\mu^+\mu^-$ with fit projections overlaid (left), background PDF obtained with misidentification emulation (center) and position dependence of the yield of corresponding background to the fit of the resonance sample. All plots are obtained for the 2012 data set.	39
4.13	Mass distribution of $B^0 \rightarrow J/\psi K^*(892)^0$ candidates with fit projections overlaid. Left and right plots are respectively the 2011 and 2012 data sets.	41
4.14	Mass distributions of the $J/\psi\pi^+\pi^-$ and $\pi^+\pi^-\mu^+\mu^-$ sample with fit projections overlaid. Left and right columns are respectively the 2011 and 2012 data sets.	45
4.15	Mass distributions of the $J/\psi\pi^+\pi^-$ (top) and $\pi^+\pi^-\mu^+\mu^-$ (bottom) sample with fit projections overlaid, combining 2011 and 2012 data sets, zoomed in the region $[5.19, 5.99] \text{ GeV}/c^2$	46
4.16	Dipion mass distributions of the $J/\psi\pi^+\pi^-$ and $\pi^+\pi^-\mu^+\mu^-$ samples. Left and right plots are respectively resonant and non-resonant data sets.	47
4.17	Likelihood profile of \mathcal{R}_s (left) and \mathcal{R}_d (right). The red line corresponds to the profile-likelihood, where, for each point probed in \mathcal{R}_i , all other parameters are floating; the blue line corresponds to the likelihood scan along to \mathcal{R}_i , where all the others parameters are fixed to their values at the minimum of the likelihood.	48
4.18	Likelihood profile in the $[\mathcal{R}_s, \mathcal{R}_d]$ plane, showed as contours levels corresponding to regions of 68.2%, 95.5%, 99.7% C.L. ($n = 1, \dots, 5\sigma$ region for a 2-dimensional χ^2).	49

4.19	Mass distributions of the $J/\psi \pi^+ \pi^-$ and $\pi^+ \pi^- \mu^+ \mu^-$ sample with fit projections overlaid, for: top row, extending the low mass region; middle row: fixing the exponential function from a fit the side band data; bottom, using a linear function for the combinatorial background. Left and right columns are respectively the 2011 and 2012 data sets.	51
4.20	Comparison of SM theoretical expectations obtained with various phenomenological techniques (points with errors) with our measurement (red line).	54
5.1	FONLL predictions of the charm quark rapidity distribution at $\sqrt{s} = 13$ TeV normalised to the central theoretical prediction (a), and ratio of the charm quark rapidity distribution in pp collisions at $\sqrt{s} = 13$ TeV and $\sqrt{s} = 7$ TeV at LHC (b) [7] .	57
5.2	Total efficiency ϵ_{tot} calculated using simulated events as a function of p_T in bins of y . The numbers of acceptance efficiency, muon ID efficiency and trigger efficiency for prompt J/ψ and J/ψ -from- b are taken to be the same.	61
5.3	Example of the fit of the mass and t_z distributions. Black points correspond to data, the prompt J/ψ contribution is shown in the shaded blue, the J/ψ -from- b contribution is shown as a black line, the wrong PV contribution is shown in shaded magenta and the combinatorial fraction is represented in shaded green.	63
5.4	Comparison of the kinematical distribution for the online (blue) and offline (red) reconstructed samples. Normalisation is arbitrary.	65
5.5	Double differential cross-sections of the the J/ψ -from- b mesons in bins of p_T and y	69
5.6	Double differential cross-sections of the prompt J/ψ mesons in bins of p_T and y .	69
5.7	Fraction of the J/ψ -from- b mesons in bins of p_T and y	70
5.8	The J/ψ -from- b production cross-section as a function of pp collision energy in the LHCb fiducial region compared to the FONLL calculation [8].	70
5.9	The prompt J/ψ production cross-section as a function of pp collision energy in the LHCb fiducial region.	71
5.10	Production cross-section of the b -quark is extrapolated to the full solid angle and compared to the FONLL predictions [8].	71
5.11	The J/ψ production cross-section for the prompt J/ψ and the J/ψ -from- b mesons as a functions of p_T and y measured at the energies of 13 TeV (back) and 8 TeV (red).	72
5.12	Ratio of the double differential production cross-section of the prompt J/ψ and the J/ψ -from- b mesons measured at the energy of pp collisions of 13 TeV to that at 8 TeV.	73
5.13	Comparison of the production cross-section of the prompt J/ψ and the J/ψ -from- b mesons in bins of p_T with the theoretical predictions.	73
5.14	The J/ψ production cross-section for the prompt J/ψ and the J/ψ -from- b mesons as a functions of p_T and y measured at the energies of 13 TeV (back) and 8 TeV (red) compared to the theoretical predictions of the NRQCD and the FONLL. Systematical uncertainty of the NRQCD prediction is not shown.	75

List of Figures

5.15	Measurements and predictions of the prompt D^0 (left) and D^+ (right) cross-section ratios. The dash-dotted lines indicate the unit ratio for each of the rapidity intervals and the dashed lines indicate a ratio of two. Each set of measurements and predictions in a given rapidity bin is offset by an additive constant m , which is shown on the plot [9].	76
6.1	Comparison of dimuon mass distribution before (left) and after (right) online-alignment procedure. Usage of outdated alignment information deteriorates mass resolution by a factor of two.	77
6.2	Layout of the (a) IT and (b) TT. Readout sectors in the IT consist of one (upper and lower boxes) or two (left and right boxes) sensors, while the sectors of the TT have one to four vertically grouped sensors according to the color scheme.	78
6.3	Interception of charged track with ST sector.	79
6.4	Map of the ratio of hit efficiency in 2015 data to that in 2012 data.	82
6.5	Map of the difference of absolute bias of residual distribution between 2015 and 2012.	82
6.6	Map of the ratio of resolution in 2015 data to that in 2012 data.	83
6.7	Hit detection efficiency map of IT sectors in 2012 (left) and in 2015 (right). Hashed regions are out of colour scheme.	83
6.8	Map of the ratio of hit detection efficiency of IT sectors found in simulation to that found in data for 2012(left) and for 2015 (right). Hashed regions are out of colour scheme.	84
6.9	Hit resolution (r.m.s. of the residual distribution) map of IT sectors in 2012 (left) and in 2015 (right). Hashed regions are out of colour scheme.	84
6.10	Map of the ratio of hit resolution of IT sectors found in simulation to that found in data for 2012(left) and for 2015 (right). Hashed regions are out of colour scheme.	85
6.11	Screenshots of STIM on the file management page (left) and the histogram configuration page (right).	87
6.12	Screenshot of STIM on home page during histogram selection.	88
6.13	Screenshots of STIM with the TT map coloured with the mean hit efficiency, obtained from efficiency trends. Such a trend is presented for readout sector “TTbVRegionCSector23” on the right side of plot, and it appears there when moving cursor over this sector.	88
6.14	Screenshots of STIM with the IT map coloured with the r.m.s. of the hit residual histogram.	89
6.15	Functional scheme of ST interactive monitor. Gray area contain instances running on LHCb online machine.	91
6.16	Relation between documents in the database.	92
6.17	Screen shots of the ST interactive monitor web page. Database used for these screen shots was filled with random data.	93

A.1	Summary distributions of the ST performance variables in 2015 for TT (left column) and IT (right column).	106
A.2	Summary distributions of the ST performance variables in 2012 for TT (left column) and IT (right column).	107
A.3	ST performance values for 2015 data-taking conditions. Hashed regions are sectors where the measured value is out of the colour scheme scale.	108
A.4	ST performance values for 2012 data-taking conditions. Hashed regions are sectors where the measured value is out of the colour scheme scale.	109
A.5	Comparison of ST performance between 2012 and 2015 data-taking conditions. Hashed regions are sectors where the measured value is out of the colour scheme scale.	110
A.6	Comparison between ST performance in simulation and data for 2015 data-taking conditions. Hashed regions are sectors where the measured value is out of the colour scheme scale.	111
A.7	Comparison between ST performance in simulation and data for 2015 data-taking conditions. Hashed regions are sectors where the measured value is out of the colour scheme scale.	112
C.1	Results of pseudo-experiments generated with signal yields according to the values found in data. Distributions of pull, error and significance of B_s^0 and B^0 signals (left an right columns, respectively).	120
C.2	Results of pseudo-experiments generated without $B^0 \rightarrow \pi^+ \pi^- \mu^+ \mu^-$ events. Distributions of pull, error and significance of B_s^0 and B^0 signals (left an right columns, respectively).	121
C.3	Results of pseudo-experiments without $B_s^0 \rightarrow \pi^+ \pi^- \mu^+ \mu^-$ events. Distributions of pull, error and significance of B_s^0 and B^0 signals (left an right columns, respectively).	122

List of Tables

4.1	Predictions of the $B_s^0 \rightarrow f_0(980)\mu^+\mu^-$ decay in the SM and in extension of it. . .	18
4.2	Predictions of the $B^0 \rightarrow \rho(770)\mu^+\mu^-$ decay in the SM and in extensions of it. . .	19
4.3	Simulation samples used in the analysis	20
4.4	Variables used as inputs in the BDT classification.	24
4.5	Additional selection requirements applied.	27
4.6	Yields of partially- and over-reconstructed decays.	30
4.7	Efficiencies of the signal and normalisation decays. The column ε_{PID} does not include the efficiency of the ProbNN(μ) requirement, which is included in $\varepsilon_{\text{pres}}$ (see Table 4.8).	31
4.8	Detailed efficiency table for $\varepsilon_{\text{trig}} \varepsilon_{\text{pres}} \varepsilon_{\text{BDT}}$ (see Table 4.7); with “Binning scheme” we consider the effect of removing the events that are out of the kinematical range that can be used in the PIDCalib package.	34
4.9	Parameters of the mis-identified $B^0 \rightarrow J/\psi K^*(892)^0$ PDF.	37
4.10	Parameters of the mis-identified $B^0 \rightarrow K^*(892)^0 \mu^+ \mu^-$ PDF.	37
4.11	Results of the fit to the $B^0 \rightarrow J/\psi K^*(892)^0$ data.	40
4.12	Parameters of the partially and over- reconstructed decays PDF.	43
4.13	Results of the fit to the data.	44
4.14	Values of $\min[-2 \log \mathcal{L}]$ and $\min[-2 \log \mathcal{L}_0]$	44
4.15	Comparison of MIGRAD and MINOS errors for \mathcal{R}_s' and \mathcal{R}_d'	47
4.16	Summary of systematic uncertainties on \mathcal{R}_s and \mathcal{R}_d	50
4.17	Values of \mathcal{R}_s and \mathcal{R}_d from the fit to data in different configurations to check the stability of the results.	52
4.18	Values of \mathcal{R}_s' and \mathcal{R}_d' from the fit to 2011 and 2012 data separately. The measured values are in agreement in the two sub-samples. The row “W.A.” reports the weighted mean of the 2011 and 2012 results; the row “default” reports the result of the simultaneous fit to the two sub-samples. All numbers are in units of 10^{-3}	52
4.19	Results of the pseudo-experiments. The second column report the values used in the generation of the pseudo-experiments for \mathcal{R}_s and \mathcal{R}_d ; all other parameters are generated with values close to the ones found in the fit to data, see the table. 4.13.	53
5.1	Hlt1DiMuonHighMass selection criteria	58

List of Tables

5.2	Hlt2DiMuonJPsiTurbo selection criteria	58
5.3	Offline selection criteria	59
5.4	Numbers of offline and online (Turbostream) candidates on each step of the reconstruction and selection sequences. Overlap is taken as a fraction of common hits within the LHCb detector between the two candidates. MC-matching procedure selects decay candidates which were correctly reconstructed from the generated decay.	64
5.5	Comparison of fit results obtained from the fit of the online and offline candidates.	64
5.6	Summary of the systematic uncertainties for the measurement of the double differential production cross-section of the J/ψ mesons at the energies of proton-proton collisions of 13 TeV. For sources marked with * we present limits of systematic uncertainty, while its exact value depends on (p_T, y) bin.	66
5.7	Summary of the systematic uncertainties for the measurement of the ratio of the double differential production cross-section of the J/ψ mesons at the energies of proton-proton collisions of 13 TeV to that at 8 TeV. Cancellation shows how the correlation of the uncertainties between the two measurements reduced the systematic uncertainty comparing to the quadratic sum of these uncertainties from these two measurements (totally uncorrelated uncertainties).	66
5.8	Production cross-sections of prompt J/ψ and J/ψ -from- b mesons, integrated over LHCb fiducial region, in pp collisions at various center-of-mass energies. The first is the total uncorrelated uncertainty, and the second the total correlated uncertainty.	72
6.1	Requirements for tracks used in the ST performance analysis. The quantity $\chi^2_{\text{system}}/\text{ndf}$ refers to the track χ^2/ndf contribution from the specific subset of the tracking stations defined in Ref. [10].	80
6.2	Summary of averaged ST performance during the 2012 and 2015 data-taking. Performance variables were weighted with the number of hits during the averaging between the sectors.	81
6.3	Changes of hit detection efficiency of TTbXRegionBSector18 during the 2015 caused by progressive malfunctioning of the bond wires.	81
B.1	Double differential production cross-section in bins of (p_T, y) in nb for J/ψ -from- b mesons. The first uncertainty is statistical, the second is the correlated systematic uncertainty shared between the bins and the last one is the uncorrelated systematic uncertainty.	114
B.2	Double differential production cross-section in bins of (p_T, y) in nb for prompt J/ψ mesons. The first uncertainty is statistical, the second is the correlated systematic uncertainty shared between the bins and the last one is the uncorrelated systematic uncertainty.	115
B.3	The ratio of cross-sections between measurements at 13 TeV and 8 TeV in different bins of p_T and y for J/ψ -from- b mesons.	116

B.4	The ratio of cross-sections between measurements at 13 TeV and 8 TeV in different bins of p_T and y for prompt J/ψ mesons.	116
B.5	The fraction of J/ψ -from- b mesons (in %) in bins of the J/ψ transverse momentum and rapidity. The uncertainty is only statistical. The systematic uncertainty is negligible.	117

1 Introduction

Nowadays, our understanding of Nature at the fundamentally microscopic level is framed into a quantum-field theory, the Standard Model (SM) of particles and interactions. The recent discovery of the Higgs boson [11, 12], which was predicted almost 40 years ago, is perhaps its greatest triumph. The Standard Model describes, through just a few free parameters, the plethora of physics processes involving the electroweak and strong interactions measured so far with great precision. However, the SM cannot explain several observed phenomena, such as neutrino masses or dark matter [13] and it is therefore believed to be an effective theory, *i.e.* a theory that is valid only up to some energy scale after which new particles would contribute to the dynamics. This motivates the search for physics beyond the SM, which is the chief goal of today's particle physics.

Searches for physics beyond the SM can be broadly classified into two approaches. The *direct* approach implies observation of new particles in controlled high energy collisions. While this approach might offer convincing evidences of the new particles, it is naturally limited by the maximum energy available in the collisions. On the other hand, the *indirect* approach does not have such a limitation since it aims at probing the presence of virtual non-SM particles in low-energy processes. Indirect searches require very high precision in experimental measurements and theoretical predictions, but are potentially sensitive to new physics at much higher energy scales than directly attainable.

Among the variety of processes used to test the SM, a special place is taken by rare decays of B-mesons. Being suppressed in the SM at the leading order, such decays proceed through quantum loops, where heavy non-SM particles could be exchanged, showing observable signs of their existence. Chapter 4 describes the search for the rare $B_{(s)}^0 \rightarrow \pi^+ \pi^- \mu^+ \mu^-$ decays in the LHCb data set collected in 2011 and 2012. These suppressed decays were not observed yet, and offer promising possibilities to test various QCD approaches that model the decay dynamics, in addition to offering a powerful indirect probe for non-SM physics. Since these decays are very rare (with about one occurrence every billion of produced B-mesons), their searches required the development of sophisticated selection procedures based on multivariate algorithms, novel data-driven techniques to control backgrounds, and robust and redundant validation

Chapter 1. Introduction

studies. The results feature the first observation of the $B_s^0 \rightarrow \pi^+ \pi^- \mu^+ \mu^-$ decay and the first evidence of the $B^0 \rightarrow \pi^+ \pi^- \mu^+ \mu^-$ decay and have been published in *Physics Letters B* 743, 46 (2015).

While the SM can give very precise predictions for phenomena governed by electroweak interactions, it typically can't describe low-energy strong interactions with the same precision, due to the non-perturbative nature of quantum chromodynamics (QCD) in that regime. The strong interaction appears in all transitions of quarks, at least through virtual processes, and quite often calculations of QCD effects give the largest contribution to the final theoretical uncertainty. Thus, experimental constraints of the various QCD techniques are crucial for improving the general predictive power of the SM. Chapter 5 describes a measurement of the production cross-section of the J/ψ meson in data collected by LHCb in summer 2015, which provides unique tests of QCD predictions. Another important outcome of this analysis is the validation of the novel data processing paradigm adopted by LHCb for Run II [14, 5], implemented here for the first time. Along with the new data-taking conditions, the limited time scale was one of the main challenges of this analysis: its results were reported just after three weeks from the start of the data-taking, which is nearly a record time with the complex infrastructures associated with LHC experiments. The analysis has been published in *Journal of High Energy Physics* 10, 172 (2015).

At the end of this thesis, at Chapter 6, I also report performance studies of one of the LHCb detectors dedicated reconstruction of charged particles and a novel monitoring system which will be implemented in 2016.

2 Introduction to the Standard Model

The Standard Model (SM) is a gauge quantum field theory based on the symmetry group $SU(3) \times SU(2) \times U(1)$ which describes the interactions of three generations of four fermion fields (u, d, e, ν) and one complex scalar field. The $SU(3)$ group describes the strong interaction through a theory called Quantum Chromodynamics (QCD), the $SU(2) \times U(1)$ group describes the electromagnetic and weak interactions and is called Quantum Electrodynamics (QED). In each generation, chiral states of the fermions form five representations of the $SU(3) \times SU(2)$ symmetry group:

$$q_L(3,2) \equiv \begin{pmatrix} u_L \\ d_L \end{pmatrix}, l_L(1,2) \equiv \begin{pmatrix} e_L \\ \nu_L \end{pmatrix}, u_R(3,1), d_R(3,1), e_R(1,1), \quad (2.1)$$

where lower indexes defines the chirality (left or right), numbers in brackets are the representation of $SU(3)$ and $SU(2)$ groups and components of the $SU(2)$ doublets are shown explicitly. Fermions that constitute $SU(3)$ triplets are called quarks, the others are called leptons. The scalar field representation is

$$\phi(1,2) \quad (2.2)$$

and it has non-zero vacuum expectation value before spontaneous symmetry breaking occurs [15, 16, 17]. Thus, the lagrangian of the SM can be written as

$$\mathcal{L} = i\bar{\psi}_{ij}\gamma_\mu D_i^\mu \psi_{ij} + |D^\mu \phi|^2 - \frac{1}{4}F_{\mu\nu}^a F^{a\mu\nu} - m^2 \phi^\dagger \phi - \lambda(\phi^\dagger \phi)^2 - Y_{i,j}^l \bar{l}_i \phi e_j - Y_{i,j}^d \bar{q}_i \phi d_j - Y_{i,j}^u \bar{q}_i \phi u_j + h.c. \quad (2.3)$$

Here,

- $\bar{\psi}_{ij}\gamma_\mu D_i^\mu \psi_{ij}$ describes the kinetic energy and the interaction of the massless fermion

Chapter 2. Introduction to the Standard Model

fields ψ_{ij} ¹ with the gauge fields by means of the covariant derivative,

$$D^\mu = \partial^\mu + i g_s G_a^\mu L_a + i g W_b^\mu T_b + i g' B^\mu Y \quad (2.4)$$

where G_a , W_b and B are the strong, weak and hypercharge boson fields; L and T are the $SU(3)$ and $SU(2)$ generators; Y is the hypercharge of a fermion; and g , g_s and g' are the gauge couplings.

- $|D^\mu \phi|^2$ describes the interaction of the Higgs field with gauge bosons. This term creates masses of the bosons under the spontaneous symmetry breaking.
- $\frac{1}{4} F_{\mu\nu}^a F^{a\mu\nu}$ represents the kinetic energy and self-interaction of the gauge fields. Here, $F_{\mu\nu}$ stands for the strength tensor of the gauge fields defined as

$$F_{\mu\nu}^a = \delta_\mu A_\nu^a - \delta_\nu A_\mu^a + g_a f^{abc} A_\nu^b A_\mu^c, \quad [t^a, t^b] = i f^{abc} t^c \quad (2.5)$$

where A is one of the B , W and G gauge fields with the coupling constant g , the generator t^a and the structure constant f^{abc} , which vanishes for the $U(1)$ group since its generators commute.

- $m^2 \phi^\dagger \phi + \lambda (\phi^\dagger \phi)^2$ is the Higgs kinetic energy and self-interaction.
- $Y_{i,j}^l \bar{l}_i \phi e_j$, $Y_{i,j}^d \bar{q}_i \phi d_j$ and $Y_{i,j}^u \bar{q}_i \tilde{\phi} u_j$ (and their hermitian conjugate) are the Yukawa coupling terms between the Higgs field and the fermions, which give them masses through the spontaneous symmetry breaking.

With the spontaneous symmetry breaking, the Higgs field is translated by the real constant

$$\phi \rightarrow \phi' + \frac{1}{\sqrt{(2)}} \begin{pmatrix} 0 \\ v \end{pmatrix}, \quad v^2 = -\frac{m^2}{\lambda} \quad (2.6)$$

where the new field ϕ' has zero vacuum expectation value. This violates $SU(2)$ symmetry, but introduces W^\pm , Z^0 and A fields through mixing of the W_b and B fields,

$$W_\mu^\pm = \frac{W_{1\mu} \mp i W_{2\mu}}{\sqrt{2}}, \quad m_W = \frac{v g}{2} \quad (2.7)$$

$$Z_\mu = \cos \theta_W B_\mu - \sin \theta_W W_{3\mu}, \quad m_Z = \frac{v \sqrt{g^2 + g'^2}}{2} = \frac{m_W}{\cos \theta_W} \quad (2.8)$$

$$A_\mu = \cos \theta_W B_\mu + \sin \theta_W W_{3\mu}, \quad m_A = 0 \quad (2.9)$$

¹where i stands for the type of the fermion (u , d , e or ν) and j corresponds to one of the three generations.

The leptonic coupling constants $Y_{i,j}^l$ can be made diagonal and thus conserve individual lepton number while this is not the case for the quark terms. Rotations in the family (u, c, t) or (d, s, b) space can diagonalise Yukawa coupling matrix in only one of these terms, which is conventionally chosen to be $Y_{i,j}^u$ [18]. It is possible to make diagonal the second mass matrix as well by introducing an additional unitary matrix, called Cabibbo-Kobayashi-Maskawa (CKM) matrix, that generates mass eigenstates through the mixture of the flavour eigenstates,

$$\begin{pmatrix} d' \\ s' \\ b' \end{pmatrix} = \begin{pmatrix} V_{ud} & V_{us} & V_{ub} \\ V_{cd} & V_{cs} & V_{cb} \\ V_{td} & V_{ts} & V_{tb} \end{pmatrix} \times \begin{pmatrix} d \\ s \\ b \end{pmatrix} \equiv \hat{V}_{\text{CKM}} \times \begin{pmatrix} d \\ s \\ b \end{pmatrix} \quad (2.10)$$

Here (d', s', b') are the mass eigenstates, and (d, s, b) are the flavour eigenstates. The CKM matrix depends on four physical parameters, three mixing angles and one complex phase. The standard parametrisation of V_{CKM} can be written as follows:

$$V_{\text{CKM}} = \begin{pmatrix} c_{12}c_{13} & s_{12}c_{13} & s_{13}e^{-i\delta} \\ -s_{12}c_{23} - c_{12}s_{23}s_{13}e^{i\delta} & c_{12}c_{23} - s_{12}s_{23}s_{13}e^{i\delta} & s_{23}c_{13} \\ s_{12}s_{23} - c_{12}c_{23}s_{13}e^{i\delta} & -c_{12}s_{23} - s_{12}c_{23}s_{13}e^{i\delta} & c_{23}c_{13} \end{pmatrix} \quad (2.11)$$

where $c_{ij} \equiv \cos(\theta_{ij})$ and $s_{ij} \equiv \sin(\theta_{ij})$. Another parametrisation (Wolfenstein parametrisation) can be obtained with expansion of each element as a power series in the small parameter $\lambda = |V_{us}| = 0.22$ [19]. An approximation of Wolfenstein parametrisation with terms up to λ^3 is

$$V_{\text{CKM}} = \begin{pmatrix} 1 - \frac{1}{2}\lambda^2 & \lambda & A\lambda^3(\rho - i\eta) \\ -\lambda & 1 - \frac{1}{2}\lambda^2 & A\lambda^2 \\ A\lambda^3(1 - \rho - i\eta) & -A\lambda^2 & 1 \end{pmatrix} + \mathcal{O}(\lambda^4) \quad (2.12)$$

where the four mixing parameters are (λ, A, ρ, η) .

Tests of the SM description of the quark sector are usually obtained by testing the unitarity of V_{CKM} . Convenient intuitive concepts for such tests are the ‘‘unitarity triangles’’, which are generic relations like

$$\sum_{i=u, c, t} V_{ij}V_{ik}^* = 0 \quad (2.13)$$

where j, k are two different quark flavours. Since V_{ij} are complex numbers, these equations are interpreted as triangles in the complex $(\rho, i\eta)$ plane, the ‘‘unitarity triangles’’. While most of these triangles are degenerated, *i.e.* they have one side much smaller than others, the choice of $j = b, i = d$ makes all sides of the triangle to be of the same order of $\mathcal{O}(\lambda^3)$ in the Wolfenstein parametrisation, which allows to probe the triangle formed by this set of variables in many complementary measurements. Tests of unitarity are done by examining whether all the measurements can be described by a unique set of (λ, A, ρ, η) variables. Figure 2.1 shows the unitarity triangle with existing constraint from the different measurements overlaid. All

measurements are in a good agreement with the CKM picture of the weak interactions of quarks.

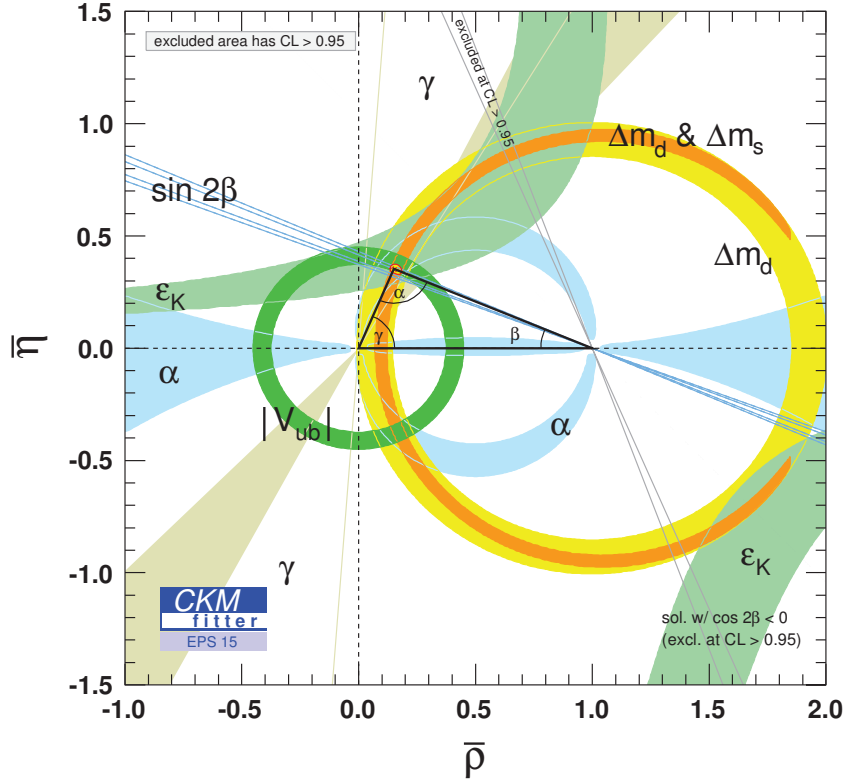


Figure 2.1 – Experimental constraints for the unitarity of the CKM matrix [1].

2.1 Flavor changing neutral currents

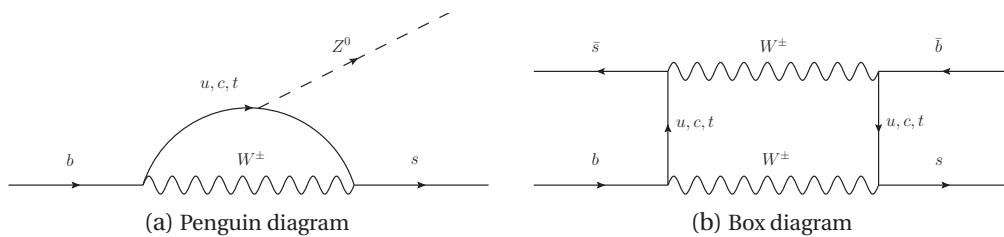


Figure 2.2 – Example of FCNC transitions of b quark through (a) penguin diagram with change of flavour $\Delta F = 1$ and (b) box diagram with $\Delta F = 2$.

Probing of the unitarity of V_{CKM} and searches for the non-SM physics are particularly informative when based on studies of processes governed by flavor-changing neutral currents of

quarks.

After the spontaneous symmetry breaking, the interactions term of the SM Lagrangian has the form

$$\mathcal{L}_{int} = \frac{g}{2\sqrt{2}}(J_\mu^+ W^{+\mu} + J_\mu^- W^{-\mu}) - eJ_\mu^{\text{em}} A^\mu + \frac{g}{2\sqrt{2}\cos\theta_W} J_\mu^0 Z^\mu \quad (2.14)$$

where e is the QED coupling constant, θ_W is the Weinberg angle, and the currents are defined as

$$J_\mu^+ = \sum_{l=e,\mu,\tau} \bar{\nu}_l \gamma_\mu (1 - \gamma_5) l + \sum_{i=1,2,3} \bar{u}_i \gamma^\mu (1 - \gamma_5) d_i', \quad (2.15)$$

$$J_\mu^{\text{em}} = \sum_f Q_f \bar{f} \gamma_\mu f, \quad (2.16)$$

$$J_\mu^0 = \sum_f \bar{f} \gamma_\mu (T_3^f - 2Q_f \sin^2 \theta_W - T_3^f \gamma_5) f, \quad (2.17)$$

with T_3^f denoting the third component of the weak isospin of the left-handed fermion. From here, the fermion flavor might be changed only through the charged current.

Being prohibited at the first order in perturbation theory (tree level), flavor changing neutral currents (FCNC) may proceed through higher order amplitudes (loop diagrams) as it is shown in Figure 2.2. At one loop level, two types of FCNC processes are possible, ‘‘penguin’’ and ‘‘box’’ diagrams. These diagrams can be interpreted as a set of effective vertices. For example, the decay amplitude for a $b \rightarrow s$ loop transition with a t quark in the loop may be expressed as [20]

$$\lambda(s, b, t) \times C \times F(m_t) \times O(b, s) \quad (2.18)$$

where $\lambda(s, b, t)$ contains information on the CKM matrix element (for example, $\lambda = V_{tb}^* V_{ts}$ for the penguin and leptonic box diagrams shown in Figure 2.2), C is a constant multiplier depending on couplings, $F(m_t)$ is a function of the mass of the internal quark in the loop and $O(b, s)$ is a local current operator (for example, $O(b, s) \equiv \bar{b} \gamma_\mu (1 - \gamma_5) s$ for the $b \rightarrow s$ transition with the emitted Z^0 boson). There are several basic functions $F(m_t)$ for different FCNC currents, and most of them grow with the mass of the internal particle [20]. This has two important consequences. First, loop diagrams with a top quark dominate the FCNC processes, and thus study of B and K meson FCNC decays give information on the V_{ti} CKM matrix elements (where $i = d, b, s$), which is hard to obtain directly. Second, this yields to increased sensitivity to massive non-SM particles which may mediate the quantum loop. This is why such processes play an important role in searches for physics beyond the SM.

While decays generated by FCNC provide a promising prospective for tests of the SM, their experimental study is complicated by their rareness. Due to unitarity of the CKM matrix, summation of loop amplitudes with various mediating quarks leads to their cancellation, which would be complete in case of equivalence of quark masses (this is so-called GIM mechanism [21]). In Chapter 4 we describe the typical experimental challenges of searches of rare decays and currently used ways to overcome them.

2.2 QCD effects

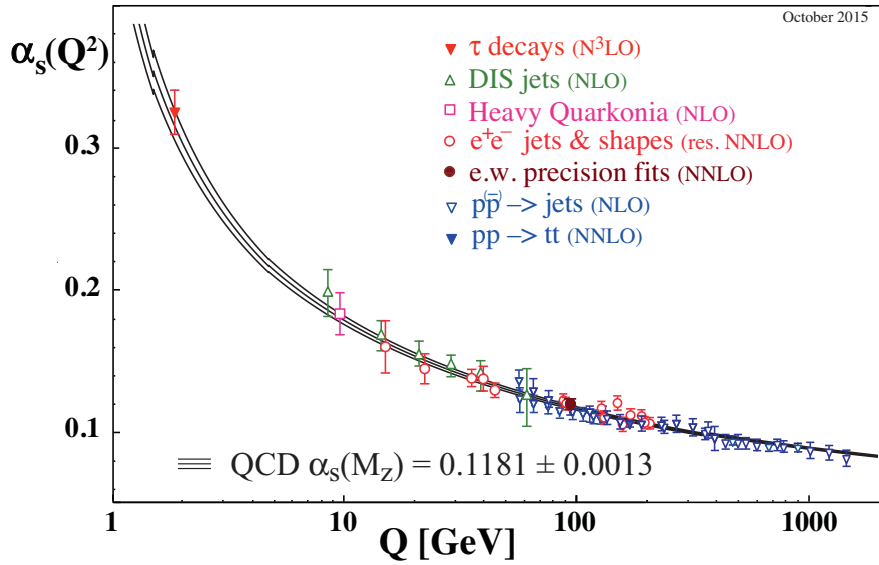


Figure 2.3 – Summary of measurements of α_s as a function of the energy scale Q [2].

In experiments we operate with hadrons, rather than with free quarks, which implies the need to account for the strong interaction that binds quarks to hadrons. An important feature of the QCD interaction is the asymptotic freedom of quarks, which is the logarithmic decrease of the coupling constant α_s with the energy (see Figure 2.3). High values of the strong coupling constant at low energies ($\alpha_s \sim \mathcal{O}(1)$) make perturbative calculations, which are successfully implemented at high energy, inapplicable for long-distance (low energy) strong interaction, which are those typically at play in the weak decays of hadrons.

The Effective Field Theory (EFT) approach provides a way to deal with both regimes of QCD by decoupling of the long distance (low energy) and the short distance (high-energy) effects in computations of the process amplitude. In the framework of EFT, the amplitude of a process $I \rightarrow F$ is written as

$$\mathcal{A}(I \rightarrow F) = \langle F | \mathcal{H}_{eff} | I \rangle = \lambda_{CKM} \sum_i C_i(\mu) \langle F | O_i(\mu) | I \rangle \quad (2.19)$$

where λ_{CKM} includes CKM elements, $C_i(\mu)$ are the Wilson coefficients describing short dis-

tance QCD effects, whereas the $\langle F|O_i(\mu)|I\rangle$ matrix element accounts that for long distance. The parameter μ is an energy scale that separates the two regimes of QCD. For hadronic matrix elements μ is taken close to the scale of the momentum transfer in a given process ($\mu \approx 1 - 5 \text{ GeV}$). Wilson coefficients are first calculated perturbatively for the energy scale of M_W and later evolved to lower values of μ with an evolution matrix $\vec{C}(\mu) = \hat{U}(\mu, M_W)\vec{C}(M_W)$ [20]. Identity of the energy scales of the Wilson coefficients and the hadronic matrix elements cancels dependence of the final amplitude on the parameter μ .

Since hadronic matrix elements accounts for phenomena within the few GeV energy range, their calculations require both perturbative and non-perturbative approaches. Theoretical calculations of the matrix elements have large uncertainties and are not always consistent, which indicate a need in deeper experimental studies of QCD sector of the SM. This work reports

1. The most sensitive search for non-SM physics in rare $B_{(s)}^0 \rightarrow \pi\pi\mu\mu$ decays, which could reveal indirect presence of non-SM particles if the observed result is inconsistent with the SM predictions, or provide refined experimental inputs for the phenomenological QCD models needed in predictions otherwise.
2. The first measurement of forward J/ψ production in pp collisions at 13 TeV, which allows crucial tests of QCD with unprecedented precision.

3 Overview of the LHCb detector

The LHCb detector is a single arm forward spectrometer dedicated to the physics of bottom and charm mesons operating at the LHC since 2010. The data-taking period from 2010 to 2012 is referred to in this text as Run I. During this period LHCb detector collected 1 fb^{-1} of data in pp collisions at $\sqrt{s} = 7 \text{ TeV}$ and 2 fb^{-1} at $\sqrt{s} = 8 \text{ TeV}$. At the end of 2012, LHC operations were paused until summer 2015 (Long Shutdown 1), when operations were resumed with pp collisions at the increased energy of 13 TeV (Run II).

A schematic overview of LHCb is presented in Figure 3.1. A detailed report of the LHCb performance is in Ref. [3]. Since the analyses reported here focus of the study of decays with charged hadrons and leptons in the final state, we focus on detector performances for

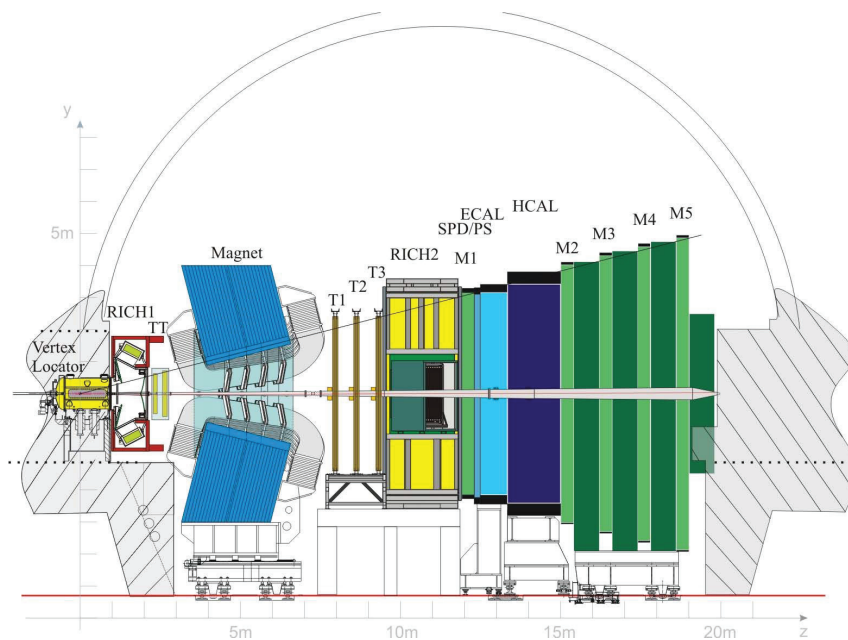


Figure 3.1 – Layout of the LHCb detector

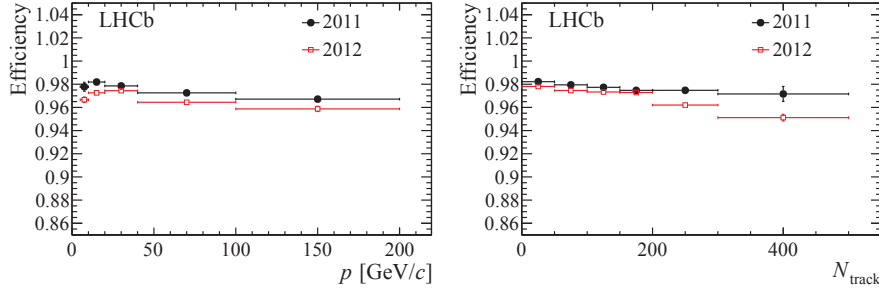


Figure 3.2 – Tracking efficiency as function of the momentum, p and the total number of tracks in the event, N_{track} [3]. The error bars indicate the statistical uncertainty

- Reconstruction of charged particles and accurate determination of their trajectories;
- Identification of muons;
- Identification of charged hadrons (π, K).

3.1 LHCb performance overview

The trajectories of charged particles traversing the tracking system are reconstructed from hits in the VERTeX LOcator (VELO), a silicon micro-strip detector surrounding the collision point; the Tracker Turicensis (TT), a silicon micro-strip detector placed upstream the magnet; and three tracking stations T1-T3 located downstream of the magnet. The tracking stations T1-T3 are composed of the straw tube Outer Tracker (OT) and the silicon micro-strip Inner Tracker (IT). The TT and IT together called the Silicon Tracker (ST).

The track finding efficiency is defined as the probability that the trajectory of a charged particle track that has passed through the full tracking system is reconstructed. It depends on the momentum of the track and the track multiplicity of the event, as shown in Figure 3.2. The average value in the LHCb detector acceptance is $\sim 96\%$. The track momentum resolution is a crucial measure of the performance of the tracking system, since it governs the mass resolution of combined particles. The dependence of the relative momentum resolution on the momentum is in Figure 3.3, which also shows the relative mass resolution for J/ψ , $\psi(2S)$, $\Upsilon(1S)$, $\Upsilon(2S)$, $\Upsilon(3S)$ mesons and the Z^0 boson reconstructed with two muon tracks. Another important characteristic of the tracking system is its ability to accurately measure the distance between the production and decay vertices of the B -hadron. This distance is used to reconstruct the particle’s decay time, which is used for background rejection as signal bottom and charged decays have typically higher decay rates than background from light quarks. A decay time resolution of ~ 50 fs is obtained in LHCb.

Two Ring-Imaging Cherenkov (RICH1 and RICH2) detectors located around the magnet provide identification for charged hadrons (π, p, K), and also contribute to the identification of charged leptons (e, μ). RICH1 and RICH2 detectors are filled with silica aerogel and C_4F_{10} gas

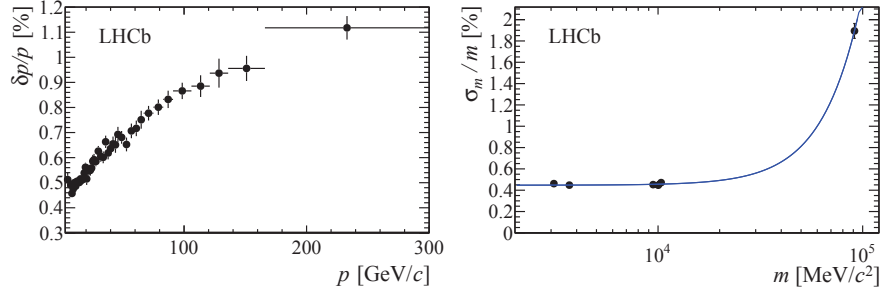


Figure 3.3 – Relative momentum resolution versus momentum for long tracks in data obtained using J/ψ decays (left) and mass resolution (σ_m) (right) as a function of the mass (m) of the dimuon resonance [3].

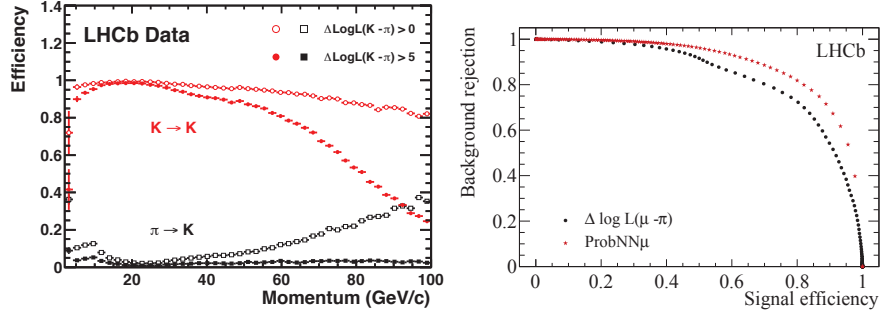


Figure 3.4 – Kaon identification efficiency and pion misidentification rate as a function of track momentum [4] (left) and background misidentification rates versus muon identification efficiency [3] (right).

radiator and with CF₄ gas radiator accordingly, which allows to cover wide range of momenta of particles, from a few GeV/c to more than 100 GeV/c. The performance of the RICH is characterized by the efficiency of the identification of particles of interest (for example, by pions) and by the misidentification rate of this selection. Figure 3.4 shows the kaon identification efficiency and $\pi \rightarrow K$ misidentification rate in bins of the track momentum for kaon identification optimized for the highest efficiency ($\Delta \log \mathcal{L}(K - \pi) > 0$) and the lowest misidentification rate ($\Delta \log \mathcal{L}(K - \pi) > 5$).

The muon identification system consists of five muon stations (M1-M5). A Gas Electron Multiplier (GEM) is utilized at M1, while Multi Wire Proportional Chambers (MWPC) are used for the rest of the muon stations. The background rejection efficiency versus the signal identification efficiency in separating pions from muons is shown in Figure 3.4.

The calorimeter system of the LHCb detector consists of a Scintillating Pad Detector (SPD), a Preshower (PS), an electromagnetic calorimeter (ECAL) and a hadronic calorimeter (HCAL). The calorimeter system reconstructs and identifies neutral particles (pions and photons), and is also used for the identification of electrons.

3.2 Data processing

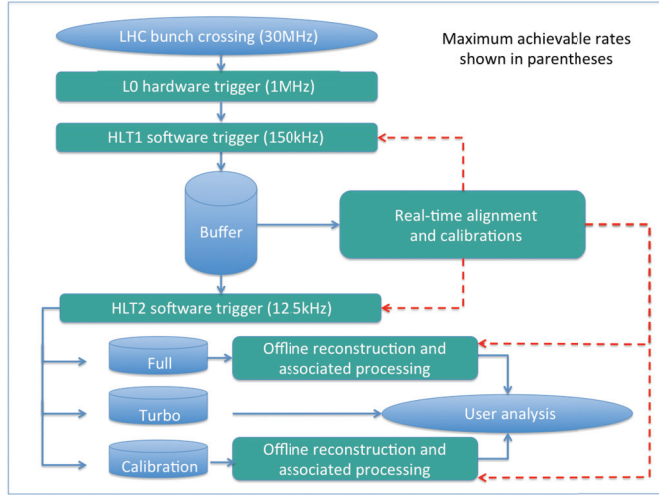


Figure 3.5 – Schematic diagram of the overall data processing in Run-II, where the blue solid line represents data flow, and the red dashed line the propagation of calibrations. [5]

In 2012, LHCb collected pp collisions data at a centre-of-mass energy of 8 TeV, with a nominal luminosity of $4 \times 10^{32} \text{ cm}^{-2}\text{s}^{-1}$. In these conditions, $\sim 3 \times 10^4$ pairs of b -hadrons and $\sim 6 \times 10^5$ pairs of c -hadrons were produced every second in $\sim 3 \times 10^7$ proton-proton collisions. The LHCb trigger system reduces this flow of data, providing preliminary selection of events that could potentially contain decays of interest, that can be accepted at a rate compatible with the maximum data-writing rate of 5 kHz (Run I) and 12.5 kHz (Run II).

The LHCb trigger system [22] is structured into three subsequent levels. The first level (L0) is a hardware trigger, which selects events containing high energy or high momentum particles based on information from the muon stations and the calorimeter system. It reduces the 30 MHz bunch crossing rate to an event rate of 1 MHz. The data is passed to the high level trigger (HLT) which is implemented using a large array of commercial processors, the “farm”. Two levels of the HLT (Hlt1 and Hlt2) perform further selection of events, and reconstruct all charged particles with transverse momentum higher than 200 MeV/ c . In 2012, 20% of the L0 output was sent to the trigger farm to be processed in absence of the data-taking (this technique is called “trigger deferral”). Events that pass the HLT2 selection undergo offline a so-called “stripping” procedure, which include offline reconstruction, creation of decay candidates, and cataloging according to predefined selection rules.

Increase of energy in proton-proton collisions from Run I to Run II cause an increase of the fraction of events with b and c hadrons. Together with increased luminosity, this led to an increase of the number of events of interest that should be stored, which offer challenge to the trigger system due to the limited capability of storage of the events (5 kHz in Run I and 12.5 kHz in RunII). LHCb collaboration is adopting a novel approach, “Turbostream”, to overcome this difficulty. It’s basic idea is to reconstruct decay candidates right on the trigger level and store

only these candidates, rather than full events [5]. This allow to reduce size required to store a single event from 70kB to 5kB and reduce processing time of a raw data by a factor of 10. Since decay candidates are reconstructed at the trigger level, good quality of such reconstruction could allow to save further offline reconstruction steps. To achieve the offline quality of decay reconstruction during the online sequence, the following requirements are required:

- **Availability of real-time calibration information for online sequence.** An important step of the event reconstruction is the reconstruction of the track trajectories from the hits in the detector. This procedure requires precise knowledge of the positions of the sensitive elements, which may slightly change during the data-taking. During Run I, alignment of the detector and PID calibration procedures were performed offline only several times a year, and thus it was possible to take into account actual calibration constants only during offline reconstruction. In Run II, alignment and PID calibration are performed on a small subset of data ($\sim 50 \times 10^3$ events) collected at the beginning of every fill¹ almost in real-time, and updated calibration constants are made available both for the trigger and offline reconstructions [23].
- **Increased time budget for a single event.** This is provided by an increased computational power of the HLT farm, and advanced usage of the deferral triggers. In Run II, all HLT farms operate in the deferral mode: when events pass the L0 trigger, they are stored at local disks of the HLT farm and can be processed any time, providing uniform load of the farm in time even in absence of data-taking.

The novel data processing model is schematically shown in Figure 3.5. Such substantial changes to the previous data processing model required meticulous validations studies which were performed during the analysis of the J/ψ production cross-section described in chapter 5, which used the Turbostream candidates for the first time in LHCb.

3.3 Simulations at LHCb

Monte-Carlo (MC) simulation plays important role in many studies performed at LHCb since it give access for estimation of many details in analysis (such as, for example, acceptance effects or interaction of particles with detector material) which are hard or impossible to compute analytically. Large number of simulated samples are produced at LHCb in a centralised manner [6]. Most of them simulate proton-proton collisions. In such events, the collision itself is modeled by PYTHIA [24] and EvtGen [25] is used to model the decay of particles. Propagation of the produced particles through the detector and its response is later simulated by the LHCb simulation based on Geant [26]. The rest of the process (response of the software trigger, event reconstruction and stripping) is identical to that for data. A schematic overview of MC production chain is shown in Figure 3.6.

¹“fill” is a period of time between injection of protons to LHC and a beam dump with typical duration of several hours

Chapter 3. Overview of the LHCb detector

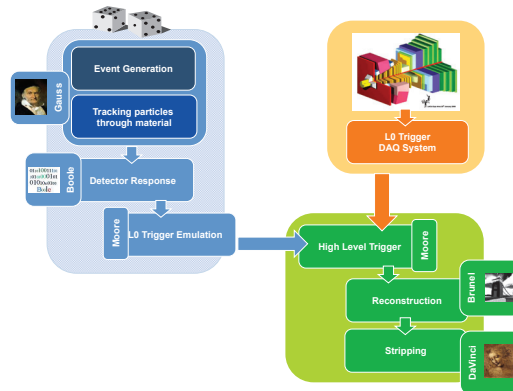


Figure 3.6 – Outline of the LHCb data processing. On the left in blue the processing of Monte Carlo samples, the Data Taking in orange on the right. The Reconstruction and Stripping for both the MC and the data collected by the DAQ of the experiment are in green. [6]

It is crucial to control possible data-simulation discrepancies. While the exact implementation of this validation depends on a specific analysis, its general idea is to compare observables between data and simulations and either correct simulation results or add this discrepancy to the systematic uncertainty. Thus, in the analyses described in Chapters 4 and 5, trigger and tracking efficiencies are validated with data-driven techniques (for analysis described in Chapter 4 description of tracking efficiency by simulations is validated in dedicated study [27]) and imperfect descriptions of distributions of some of the variables are studied from comparison of simulations with clean and high-statistics data samples and are accounted in systematic uncertainties of selection efficiencies.

4 Search for $B \rightarrow \pi\pi\mu\mu$ decays

4.1 Introduction

In this chapter we describe the search for the rare $B_{(s)}^0 \rightarrow \pi^+\pi^-\mu^+\mu^-$ decays with dipion mass range in $[0.5, 1.3] \text{ GeV}/c^2$ in data collected by the LHCb detector in 2011 and 2012. Such choice of the mass window is motivated by the fact that the major contribution within this mass window is given by $B_s^0 \rightarrow f_0(980)\mu^+\mu^-$ and $B^0 \rightarrow \rho(770)\mu^+\mu^-$ decays, the study of which is of particular interest.

4.1.1 Theoretical motivation

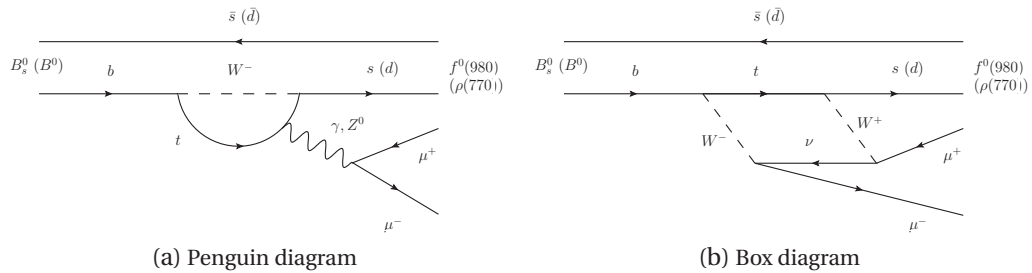


Figure 4.1 – Example of (a) penguin and (b) box Feynman diagrams for $B_{(s)}^0 \rightarrow \rho(770)(f_0(980))\mu^+\mu^-$ processes.

The $B_s^0 \rightarrow f_0(980)\mu^+\mu^-$ decay is dominated in the SM by the “penguin” and “box” $b \rightarrow s$ amplitudes (see Figure 4.1), which are sensitive to non-SM physics, similarly to the well-known $B^0 \rightarrow K^*(892)^0\mu^+\mu^-$ and $B_s^0 \rightarrow \phi\mu^+\mu^-$ decays [28, 29, 30]. At the same time, measurement of the branching fraction of this decay mode can provide a test of the several SM predictions, obtained with use of the different phenomenological models of low-energy QCD.

As discussed in Section 2.2, the amplitude of the $B_s^0 \rightarrow f_0(980)\bar{l}l$ transition in the frame of the

Chapter 4. Search for $B \rightarrow \pi\pi\mu\mu$ decays

effective field theory may be expressed as follows:

$$\mathcal{A}(B_s^0 \rightarrow f_0(980)\bar{l}l) = \frac{G_F}{2\sqrt{2}} \frac{\alpha_{em}}{\pi} V_{ts}^* V_{tb} \sum_i C_i(\mu) \langle f_0(980)\bar{l}l | O_i(\mu) | B_s^0 \rangle \quad (4.1)$$

While the complete list of the Wilson coefficients and the local operators $O_i(\mu)$ used in this summation can be found in Refs. [31, 32, 20], it is important to note that the matrix elements $\langle f_0(980)\bar{l}l | O_i(\mu) | B_s^0 \rangle$ may be split into an hadronic and a leptonic part,

$$\langle f_0(980)\bar{l}l | O(\mu) | B_s^0 \rangle = \langle \bar{l}l | (\bar{l}l)_j | 0 \rangle \langle f_0(980) | (\bar{s}b)^j | B_s^0 \rangle. \quad (4.2)$$

Several QCD approaches predict different dependence of the hadronic matrix element $\langle f_0(980) | (\bar{s}b)^j | B_s^0 \rangle$ (and thus the decay branching fraction) on the $f_0(980)$ decay constant, \bar{f} , which is defined as $\langle f_0(980) | \bar{s}s | 0 \rangle = M_{f_0} \bar{f}$. Perturbative QCD (pQCD [31]) and light-cone QCD sum rules (LCSR [33, 32]) predict that $\mathcal{B}(B_s^0 \rightarrow \pi^+\pi^-\mu^+\mu^-)$ depends on the $f_0(980)$ decay constant as \bar{f}^2 , while in the framework of the three-point QCD sum rules (tpQCDSR [34]) the dependence is $1/\bar{f}^2$. This results in significant differences between numerical predictions of $\mathcal{B}(B_s^0 \rightarrow \pi^+\pi^-\mu^+\mu^-)$ based on tpQCDSR or by pQCD or LCSR (see Table 4.1). A measurement of the branching fraction of $B_s^0 \rightarrow f_0(980)\mu^+\mu^-$ decay can favor or disfavor each of these approaches and, in general, offer an input for other phenomenological models. The branching fraction of the $B_s^0 \rightarrow f_0(980)\mu^+\mu^-$ decay is also calculated in some non-SM scenarios described in Refs. [35, 36], however these predictions can not be distinguished from SM predictions given the current size of SM uncertainties.

$\mathcal{B}(B_s^0 \rightarrow f_0(980)\mu^+\mu^-)$	Ref.
$(52.1^{+32.3}_{-20.6}) \times 10^{-8}$	[31]
$(9.5^{+3.1}_{-2.6}) \times 10^{-8}$	[33]
$(16.7 \pm 6.1) \times 10^{-8}$	[33]
$(0.81 - 2.02) \times 10^{-8}$	[34]
$(0.063 - 0.337) \times 10^{-8}$	[34]
$(8.8 \pm 1.97) \times 10^{-8}$	[35] (non-SM)

Table 4.1 – Predictions of the $B_s^0 \rightarrow f_0(980)\mu^+\mu^-$ decay in the SM and in extension of it.

The $B^0 \rightarrow \rho(770)\mu^+\mu^-$ decay proceeds through the ‘‘penguin’’ and ‘‘box’’ $b \rightarrow d$ amplitudes, which are suppressed with respect to the $b \rightarrow s$ amplitudes by the ratio $|V_{td}|/|V_{ts}| \sim 0.2$. This makes the $B^0 \rightarrow \rho(770)\mu^+\mu^-$ decays interesting for a complementary search of physics beyond the SM with respect to the $B_s^0 \rightarrow f_0(980)\mu^+\mu^-$ analysis. Theoretical predictions of the branching fraction of this decay are shown in Table 4.2.

$\mathcal{B}(B^0 \rightarrow \rho(770)\mu^+\mu^-)$	Ref.
$(5.0^{+2.1}_{-2.6}) \times 10^{-8}$	[37, 38]
$(8.6^{+3.4}_{-4.5}) \times 10^{-8}$	[37, 39]
$\sim 10 \times 10^{-8}$	[40] (non-SM)
6×10^{-8}	[41] (non-SM)
$(2.8 - 8.4) \times 10^{-8}$	[42] (non-SM)

 Table 4.2 – Predictions of the $B^0 \rightarrow \rho(770)\mu^+\mu^-$ decay in the SM and in extensions of it.

4.1.2 Choice of the dipion mass range

The $B_s^0 \rightarrow f_0(980)\mu^+\mu^-$ decay manifests itself as a peak in the $\pi^+\pi^-\mu^+\mu^-$ mass spectrum centred at the B_s^0 mass, and with the $\pi^+\pi^-$ invariant mass corresponding to the mass of the $f_0(980)$ resonance. The latter has a width that ranges from 40 to 100 MeV [43]. Therefore, the $f_0(980)$ state significantly overlaps within the $\pi^+\pi^-$ mass spectrum with the $\rho(770)$ resonance, which has a large width close to 150 MeV [43]. The choice of the [0.5, 1.3] GeV/ c^2 window for the dipion invariant mass allows to study both $B_s^0 \rightarrow f_0(980)\mu^+\mu^-$ and $B^0 \rightarrow \rho(770)\mu^+\mu^-$ decay modes simultaneously.

4.1.3 The main observables

The chief goal of this study is to search for $B_s^0 \rightarrow f_0(980)\mu^+\mu^-$ and $B^0 \rightarrow \rho(770)\mu^+\mu^-$ decays and measure their branching fractions (or to set their upper limits). In order to cancel numerous systematics (such as luminosity uncertainty, uncertainty in production of b quark, *etc.*), we estimate the branching fractions normalised to the branching fraction of the $B^0 \rightarrow J/\psi K^*(892)^0$ decay, where $J/\psi \rightarrow \mu^+\mu^-$ and $K^*(892)^0 \rightarrow K^+\pi^-$:

$$\mathcal{R}_s \equiv \frac{\mathcal{B}(B_s^0 \rightarrow \pi^+\pi^-\mu^+\mu^-)}{\mathcal{B}(B^0 \rightarrow J/\psi K^*(892)^0)} = \frac{f_d}{f_s} \frac{N(B_s^0 \rightarrow \pi^+\pi^-\mu^+\mu^-)}{N(B^0 \rightarrow J/\psi K^*(892)^0)} \varepsilon_{\text{rel}}^s, \quad (4.3)$$

$$\mathcal{R}_d \equiv \frac{\mathcal{B}(B^0 \rightarrow \pi^+\pi^-\mu^+\mu^-)}{\mathcal{B}(B^0 \rightarrow J/\psi K^*(892)^0)} = \frac{N(B^0 \rightarrow \pi^+\pi^-\mu^+\mu^-)}{N(B^0 \rightarrow J/\psi K^*(892)^0)} \varepsilon_{\text{rel}}^d, \quad (4.4)$$

where

- $N(X)$ is the number of the observed decays;
- $\varepsilon_{\text{rel}}^s = \varepsilon(B^0 \rightarrow J/\psi K^*(892)^0) / \varepsilon(B_s^0 \rightarrow \pi^+\pi^-\mu^+\mu^-)$ is the selection efficiency of the $B^0 \rightarrow J/\psi K^*(892)^0$ decay relative to that of the $B_s^0 \rightarrow \pi^+\pi^-\mu^+\mu^-$ decay;
- $\varepsilon_{\text{rel}}^d = \varepsilon(B^0 \rightarrow J/\psi K^*(892)^0) / \varepsilon(B^0 \rightarrow \pi^+\pi^-\mu^+\mu^-)$ is the selection efficiency of the $B^0 \rightarrow J/\psi K^*(892)^0$ decay relative to that of the $B^0 \rightarrow \pi^+\pi^-\mu^+\mu^-$ decay;
- f_d/f_s is the ratio of the fragmentation probabilities of the b -quark to the B^0 and B_s^0

Chapter 4. Search for $B \rightarrow \pi\pi\mu\mu$ decays

mesons. The value of f_d/f_s is measured by LHCb collaboration with use of already-measured branching fractions of some of B and D decays [51].

A choice of normalisation channel is dictated by it's high statistics, similarities in kinematics with the signal channel and by the fact that it's branching ratio and composition of $K\pi$ spectrum is well-studied at LHCb.

The data and the simulation samples, along with the selection and its optimisation towards the observation of the $B_{(s)}^0 \rightarrow \pi^+\pi^-\mu^+\mu^-$ decays, are presented in Section 4.2. The relative efficiencies are determined using both simulated samples and control samples of data, as described in Section 4.2.7. The number of events entering equations 4.3 and 4.4 are determined in Section 4.4 from the fit of the $J/\psi\pi^+K$ mass spectrum and simultaneous fit of the $\pi^+\pi^-\mu^+\mu^-$ and $J/\psi\pi^+\pi^-$ mass spectra. Finally, we present the results of the analysis and draw the conclusions in Section 4.7.

4.2 Data samples and selection

Decay mode	Generated events
$B^0 \rightarrow \rho(770)\mu^+\mu^-$	2M(2011) + 0.5M(2012)
$B_s^0 \rightarrow f_0(980)\mu^+\mu^-$	0.5M(2011) + 0.5M(2012)
$B_s^0 \rightarrow f_0(980)\mu^+\mu^-$ (phase space)	0.5M(2011) + 0.5M(2012)
$B_s^0 \rightarrow J/\psi f_0(980)$	2M(2011) + 1.5M(2012)
$B^0 \rightarrow J/\psi\rho(770)$	0.1M(2011) + 0.5M(2012)
$B^0 \rightarrow J/\psi K^*(892)^0$	10M(2011) + 1M(2012)
$B_s^0 \rightarrow \phi\mu^+\mu^-$	0.5M(2011)
$B^+ \rightarrow J/\psi K^+$	12M(2011) + 5M(2012)
$B_s \rightarrow J/\psi\eta'$	0.7M(2011) + 1M(2012)
$B_c^+ \rightarrow J/\psi\pi^+\pi^-\pi^+$	2M(2011) + 4M(2012)

Table 4.3 – Simulation samples used in the analysis

This analysis uses proton-proton collisions data collected by the LHCb detector during Run I. The integrated luminosity of the data set is 3fb^{-1} , where 1fb^{-1} is collected at center-of-mass energy of 7 TeV, and 2fb^{-1} are collected at 8 TeV. This analysis also uses simulations for studies of the selection efficiency, development of the fit model and validation studies. The list of simulated samples used in this analysis is presented in Table 4.3. Simulation reproduces both the 2011 and 2012 running conditions.

4.2.1 Preselection

The trigger selection of this analysis enrich output dataset with events containing signal candidates by exploiting it's peculiarities:

Hardware trigger On a hardware level, LHCb trigger system selects events with either one or two muons with high transverse momenta, which exploits high mass of the B -meson. Nearly 5% of events are also selected due to high- p_T hadron.

Software trigger 1 The first level of the software trigger selects events with two muons with invariant mass is within kinematically -allowed $([0.2, 5] \text{ GeV}/c^2)$ region for studied decays, or with presence of high- p_T or high-energy tracks.

Software trigger 2 The second level of the software trigger selects events which satisfy to at least one of the following criteria: the two muons originating from a point detached from the primary vertices; one muon has high p_T ; several tracks form a vertex, which is detached from the primary vertex.

Detailed information on the requirements used in the selection is in Refs. [44, 45, 46].

After the trigger selection, the events are processed with the `B2XMUMU` line of the Stripping `v20r0p3` (`v20r1p3`) for the 2012 (2011) data-taking conditions [47]. This line creates B -meson candidates from the two pairs (two hadrons and two muons) of tracks originating from the same displaced vertex. The reconstructed candidate is required to have a well-reconstructed secondary vertex separated from the associated primary vertex.

4.2.2 Sample composition

Using cuts on the invariant masses and the particle identification information (the latter is described in more detail in Section 4.2.5), we classify the selected decay candidates into the following categories:

“Normalisation” Candidates in the “normalisation” sample are required to have one of the hadrons to be kaon, and another to be pion and the invariant $\mu^+\mu^-$ mass should be within the J/ψ window $M_{\mu^+\mu^-} \in [2.796, 3.216] \text{ GeV}/c^2$. This sample is used to reconstruct the $B^0 \rightarrow J/\psi K^*(892)^0$ candidates, which are used for the normalisation of the branching ratios.

“Signal” or “non-resonant” The “signal” (also referred as “non-resonant”) sample is used for selection of the signal $B_s^0 \rightarrow \pi^+\pi^-\mu^+\mu^-$ and $B^0 \rightarrow \pi^+\pi^-\mu^+\mu^-$ decays. Candidates from this sample are required to have both hadrons to be pions and invariant dimuon mass to be inconsistent with the J/ψ and $\psi(2S)$ resonances: $M_{\mu^+\mu^-} \in [0.212, 1.01] \cup [1.030, 2.796] \cup [3.216, 3.436] \cup [3.806, 5.05] \text{ GeV}/c^2$. The $[1.01, 1.03] \text{ GeV}/c^2$ dimuon region is excluded in order to avoid the possible contamination from the $B_{(s)}^0 \rightarrow D_{(s)}^- (\rightarrow \phi\pi)\pi^+$ decays with $\phi \rightarrow \mu\mu$.

“Resonant” The decay candidates in the “resonant” sample are required to have both hadrons to be pions and the dimuon invariant mass is required to be within the J/ψ mass window. This sample includes candidates from $B_s^0 \rightarrow J/\psi \pi^+\pi^-$ and $B^0 \rightarrow J/\psi \pi^+\pi^-$ decays and

is used as a proxy for the non-resonant sample: to check the description of the fit components at higher statistic; to determine some of the shape parameters; and to optimise the suppression of π - K misidentification.

The type of the track (pion or kaon) is defined here through the particle identification (PID) variable, difference of logarithm of a likelihood between pion and kaon hypothesis for a given track, $DLL(\pi - K)$. For each track, these hypotheses are obtained through combination of likelihoods from RICH, Velo, muon chambers and calorimeters [4]. After the preselection, kaon tracks are selected with $DLL(\pi - K) < 5$ and pion tracks with $DLL(\pi - K) > -5$. In order to include both $\rho(770)$ and $f_0(980)$ resonances in the $\pi^+\pi^-$ invariant mass spectrum, the requirement $M_{\pi^+\pi^-} \in [0.5, 1.3] \text{ GeV}/c^2$ is applied for both signal and resonant samples. The normalisation sample is required to have invariant mass of the two hadrons within the $K^*(892)^0$ mass window, $M_{K\pi} \in [0.826, 0.966] \text{ GeV}/c^2$.

4.2.3 Selection strategy

Distributions of the four-particle invariant mass $M_{\pi^+\pi^-\mu^+\mu^-}$ after the stripping selection for the resonant and the signal samples are shown in Figure 4.2. For the signal sample this distribution approximates a decline using exponential which indicates that a core fraction of this sample is made of “combinatorial” candidates composed of random tracks. These events are suppressed by means of the multivariate classifier discussed in Section 4.2.4. A significant peak around $5.1 \text{ GeV}/c^2$ in the distribution of the invariant mass of the resonant candidates and a bump in that of signal candidates corresponds to the $B^0 \rightarrow K^*(892)^0(\rightarrow K\pi)\mu\mu$ events with the kaon misidentified as a pion. This and other “misidentification” backgrounds are suppressed as it is described in Section 4.2.5. Background originating from wrongly reconstructed decays are discussed in Section 4.2.6.

4.2.4 Multivariate selection

A boosted decision tree (BDT) algorithm is used to suppress the combinatorial background. The algorithm is taken from the TMVA package of ROOT [48, 49]. Simulated $B_s^0 \rightarrow \pi^+\pi^-\mu^+\mu^-$ decays are used as a signal sample for training of the BDT. Candidates from the high-mass sideband of the signal data sample ($M_{\pi^+\pi^-\mu^+\mu^-} \in [5.5, 5.8] \text{ GeV}/c^2$) are used as a background sample since no candidates from B decays are expected in this region and thus it is populated mainly by pure combinatorial candidates. The training is performed separately for the 2011 and 2012 running conditions. Both the signal and the background samples are split into two equal-size subsets for training and testing the multivariate classifier. For each running condition, two classifier are trained so that the training sample of one classifier is the test sample for the other one and vice-versa. Input variables for the classifiers listed in Table 4.4 exploit peculiarities of the signal decays and their topology:

- Since B is long-lived particle, secondary vertex of signal candidate should be displaced

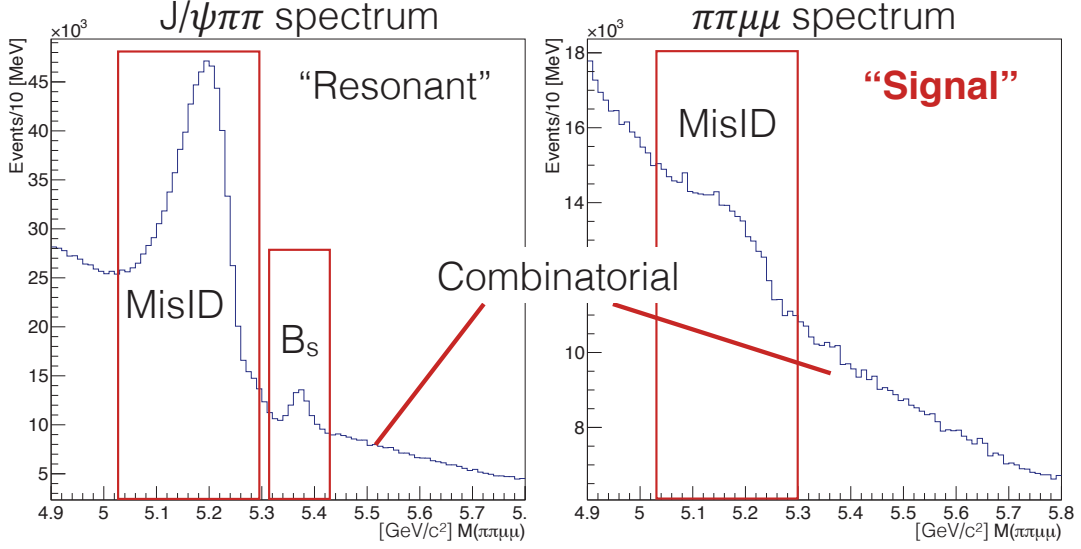


Figure 4.2 – Mass distributions of the resonant (left) and the signal (right) samples after the stripping selection.

from the vertex and tracks of the candidate should have big “Impact Parameter χ^2 ” (variation of the vertex χ^2 on association of the track to the vertex);

- Since B is a heavy meson, the decay products are expected to have high p_T . Since two pions originates from the resonance, their summed p_T is also expected to be high;
- Four tracks should come from the same point, which means that signal candidates should have well-reconstructed secondary vertex;
- Secondary vertex should be displaced from the associated primary vertex in direction of momentum, which means small “direction angle” (angle between reconstructed momenta and displacement of vertexes) for signal candidates.

The separation of signal and background categories obtained with the BDT for the 2011 and 2012 running conditions is shown in Figure 4.3. Matching of test and training distributions of the BDT response supports evidence for absence of over-training. To test the robustness of the BDT against data/simulations mismodelings, we compare distributions of input BDT variables for simulated $B^0 \rightarrow J/\psi K^* (892)^0$ sample with that for $B^0 \rightarrow J/\psi K^* (892)^0$ signal sPlotted from the normalisation channel. The observed discrepancies in transverse momentum of the B

Variables	BDT rank
$\min\{\text{IP}_{\chi^2}(\pi^+), \text{IP}_{\chi^2}(\pi^-)\}$	0.1651
B vertex χ^2	0.1524
B direction angle	0.1194
$\min\{\text{IP}_{\chi^2}(\mu^+), \text{IP}_{\chi^2}(\mu^-)\}$	0.1111
$p_T(B)$	0.09
$p_T(\pi^+) + p_T(\pi^-)$	0.06
$ p_T(\mu^+) - p_T(\mu^-) $	0.0435
$c\tau(B)$	0.0408
$ \text{IP}_{\chi^2}(\pi^+) - \text{IP}_{\chi^2}(\pi^-) $	0.04
$c\tau(B)\chi^2$	0.04
$\min\{p_T(\mu^+), p_T(\mu^-)\}$	0.0345
B min. IP χ^2	0.0312
$ \text{IP}_{\chi^2}(\mu^+) - \text{IP}_{\chi^2}(\mu^-) $	0.0293
$ p_T(\pi^+) - p_T(\pi^-) $	0.0248
$\min\{p_T(\pi^+), p_T(\pi^-)\}$	0.0197

Table 4.4 – Variables used as inputs in the BDT classification.

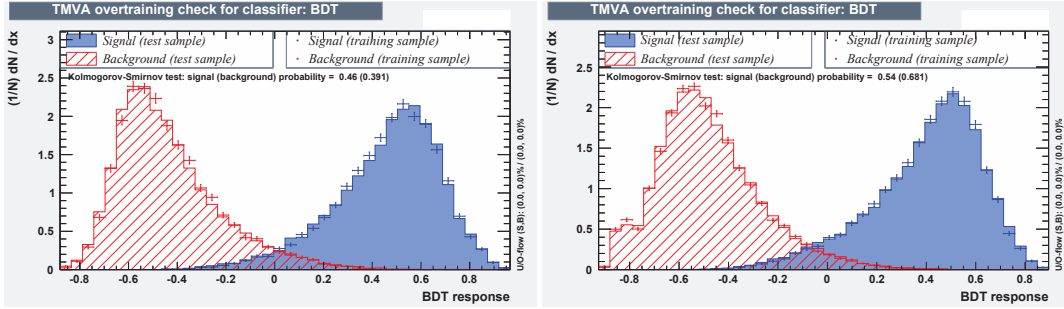


Figure 4.3 – Comparison of the BDT output for test and training distributions for 2011 (left) and 2012 (right) data sets.

meson and χ^2 of the secondary vertex were taken into account by reweighting the MC samples. A two-dimensional reweighting is performed in $(p_T(B), \chi_{BV}^2)$ bins with weights defined as

$$w_i = \frac{N_i^{Norm}}{N_i^{MC}} \times \frac{N_{tot}^{Norm}}{N_{tot}^{MC}} \quad (4.5)$$

where $N_i^{Norm(MC)}$ is the number of decay candidates in bin i in compared normalisation (simulation) sample and $N_{tot}^{Norm(MC)}$ is the total number of decay candidates in compared samples. While these distributions for reweighted samples show good agreement (see Figure 4.6), we also compare distributions of BDT responses obtained for these two samples to ensure that all correlations are also well-reproduced (see Figure 4.7). Small discrepancies of these two distributions resulting in small differences of selection efficiencies are taken as systematic

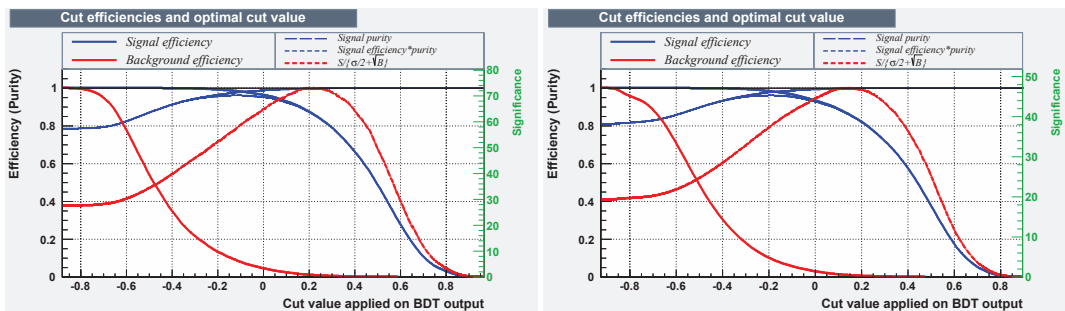


Figure 4.4 – Optimisation of the BDT cut-point for 2011 (left) and 2012 (right) data sets. The figure of merit $\epsilon/(\alpha/2 + \sqrt{B})$ is shown with the dashed red line.

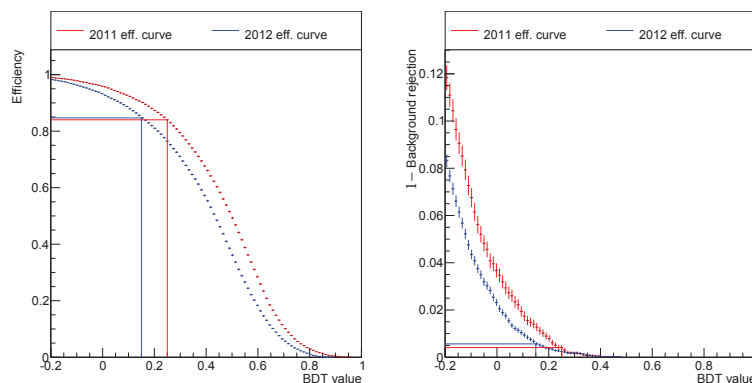


Figure 4.5 – Left: signal efficiencies for the 2011 and 2012 BDTs selection. Right: background efficiencies for the 2011 and 2012 BDTs.

uncertainties, as described below.

The cut value on the BDT output is chosen to maximize the figure of merit $\epsilon/(\alpha/2 + \sqrt{B})$ where ϵ is the signal selection efficiency, B is the number of remained background candidates and α is the expected significance of the signal in standard deviations [50] ($\alpha = 3$ for 2011 and $\alpha = 5$ for 2012). Such figure of merit is optimal in searches for rare signals since it does not push the optimal cut point towards very low backgrounds (unlike S/\sqrt{B}) and does not require apriori knowledge of the branching ratio of the signal (unlike $S/\sqrt{S+B}$). The optimal BDT cut values are selected to be 0.25 for the 2011 and 0.15 for the 2012 running conditions respectively (see Figure 4.4). Selection efficiencies for the signal and the background categories for the 2011 running conditions are found to be close to that for the 2012, as shown in Figure 4.5.

4.2.5 Misidentified decays

Decay candidates that have the same final state of the signal as a result of a misidentification of one or more charged particles are referred to as “misidentified backgrounds”. Such backgrounds are suppressed with requirements on the quality of the particle identification and

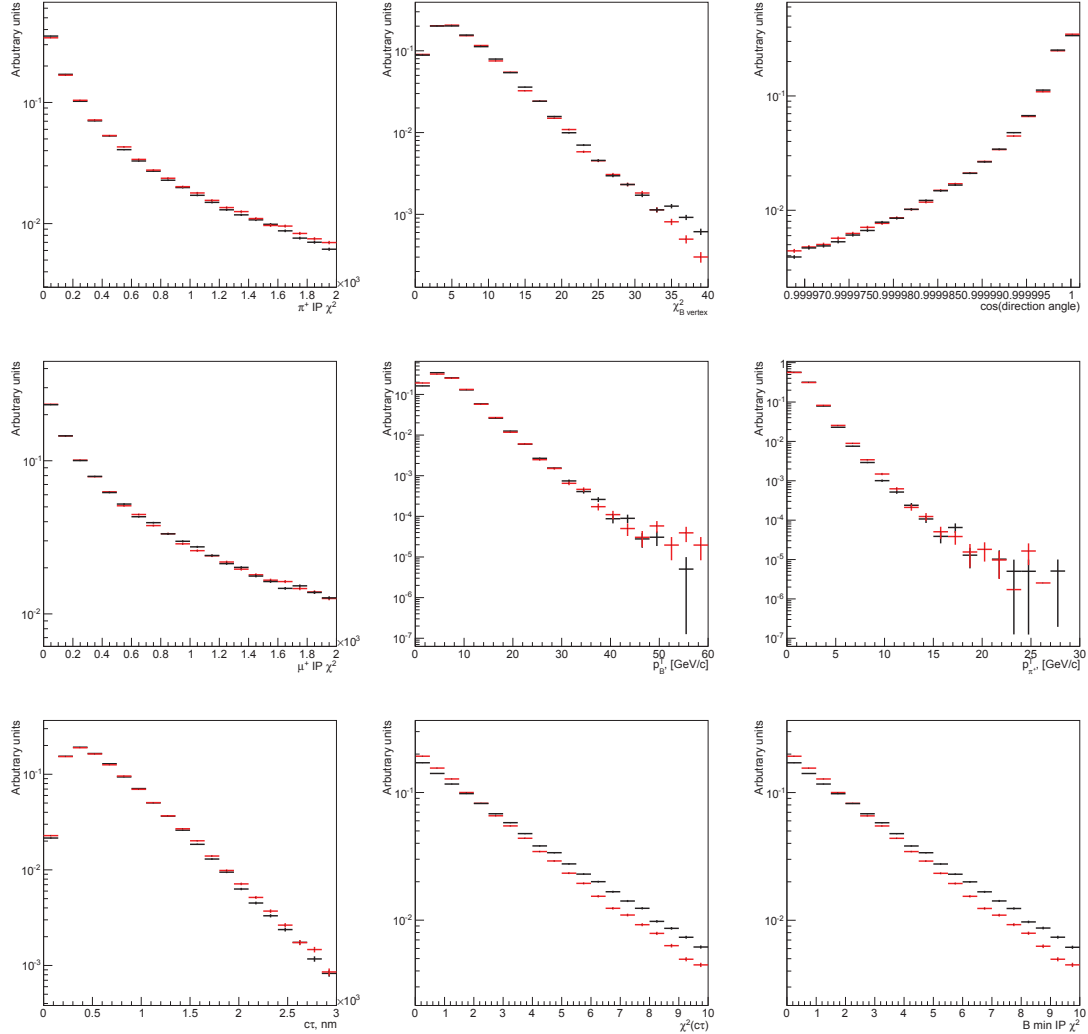


Figure 4.6 – Comparison of BDT input variables distributions for data (black) and simulations (red) samples

with vetoes on the $\pi^+ \pi^- \mu^+ \mu^-$, $\pi^+ \pi^-$ and $\mu^+ \mu^-$ invariant masses.

The main source of the misidentified backgrounds are the $B^0 \rightarrow K^*(892)^0 \mu^+ \mu^-$ and $B^0 \rightarrow J/\psi K^*(892)^0$ decays with the kaon misidentified as a pion. This background is suppressed with a cut on the $DLL(\pi - K)$ variable defined in Section 4.2.2. To optimise PID selection separately from BDT selection (and to factorise PID and BDT selection efficiencies as it will be done in Section 4.2.7), we assume neglect correlation between BDT and PID selections, which is justified by a small ($\sim 5\%$) correlation values between these variables obtained on signal (MC) and background (data sidebands) samples. Scatter plot of BDT and PID variables for signal and background samples are presented in Figure 4.8.

The requirement on the PID variable is optimised on the resonant sample under the assump-

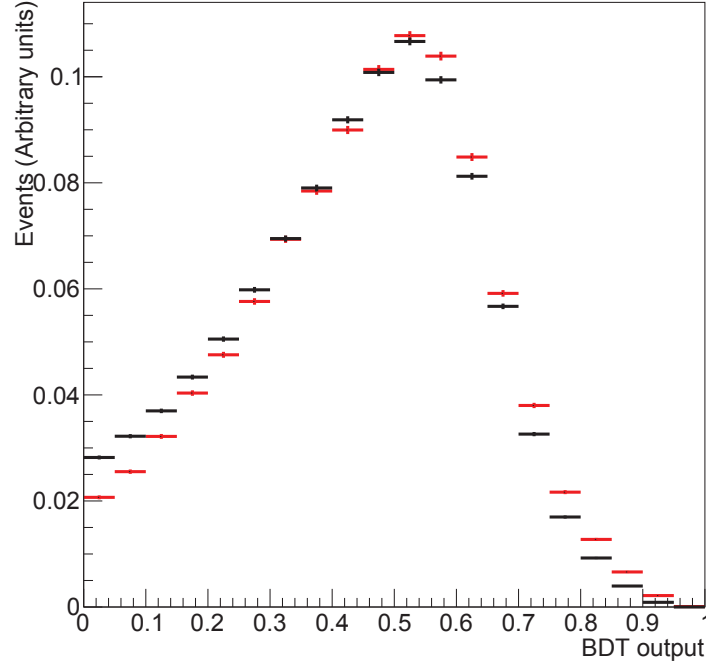


Figure 4.7 – Comparison of BDT output distributions for data (black) and simulations (red) samples

Variable	Requirement
$DLL(\pi - K)$	> 1
$DLL(\pi - \mu)$	> -1
$DLL(\pi - p)$	> 0
$\text{ProbNN}(\mu)$	> 0.25
$M_{\pi\pi}$	$\in [0.5, 1.3] \text{ GeV}/c^2$
$M_{\mu\mu}^{\text{signal}}$	$\in [0.212, 1.010] \cup [1.030, 2.796] \cup [3.216, 3.436] \cup [3.806, 5.05] \text{ GeV}/c^2$
$M_{\mu\mu}^{\text{resonant}}$	$\in [2.796, 3.216] \text{ GeV}/c^2$
$M_{\pi^+\pi^-\mu^+\mu^-}$	$\in [5.19, 6.99] \text{ GeV}/c^2$
$M_{\mu\mu}^{\pi \leftrightarrow \mu}$	$\notin [3.036, 3.156] \cup [3.625, 3.745] \text{ GeV}/c^2$

Table 4.5 – Additional selection requirements applied.

tion of equal S/B ratios in the signal and resonant samples. This assumption is justified by the fact that resonant and signal channels differ only in intermediate $\mu\mu$ state, and structure of dimuon mass spectrum is expected to be similar for signal and background decays due to similar diagrams governing them. The figure of merit for PID optimisation is chosen to be $S/\sqrt{S+B}$, where S and B are defined as the $B^0 \rightarrow J/\psi \pi^+ \pi^-$ and $B^0 \rightarrow J/\psi K^* (892)^0$ yields, respectively, obtained from the fit of the resonant sample with the following fit model: double

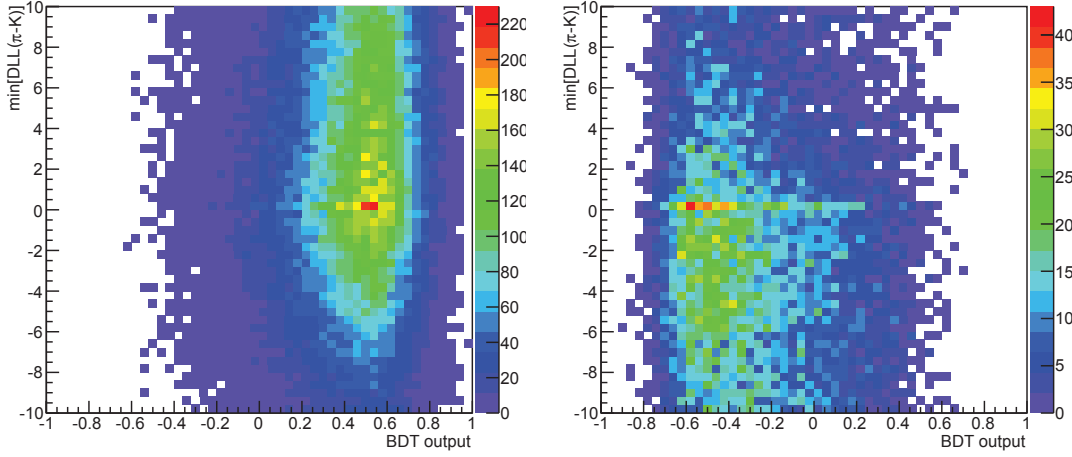


Figure 4.8 – BDT output variable versus the PID criteria for the signal (left) and background (right) samples. Distribution of candidates on these plots evidence negligibly small correlation between the two variables for examined samples.

Crystal Ball functions with the same mean and opposite side tails to describe contributions from the $B_s^0 \rightarrow J/\psi \pi^+ \pi^-$ and $B^0 \rightarrow J/\psi \pi^+ \pi^-$ decays, exponential function to describe the combinatorial background and empirical shape describing the contribution from the misidentified $B^0 \rightarrow J/\psi K^* (892)^0$ candidates. The procedure of obtaining this shape is described in Section 4.3

The optimal value for particle identification cut is found to be $DLL(\pi - K) > 1$ for both the 2011 and 2012 running conditions. After the full selection, the mean value and the uncertainty of yields of the misidentified $B^0 \rightarrow K^* (892)^0 \mu^+ \mu^-$ decays are estimated from the data with the procedure described in Section 4.3. This procedure is used in the fit of the signal sample described in Section 4.4 to define the contribution from the $B^0 \rightarrow K^* (892)^0 \mu^+ \mu^-$ decays.

Other requirements on the PID variables in Table 4.5 are set by choosing a threshold that preserves a 95% efficiency on signal, estimated with the $B_s^0 \rightarrow f_0(980) \mu^+ \mu^-$ simulation. Those requirements allow to suppress contamination from the decays with misidentified particles, such as muon-pion and proton-pion misidentifications. Background candidates from proton-pion misidentification typically originate from Λ decays and are suppressed by the $DLL(\pi - p) > 0$ requirement. The muon-pion misidentification in the resonant sample may results in extra candidates in the signal sample, which are kinematically indistinguishable from the properly reconstructed decays due to the proximity of muon and pion masses. To avoid it, we have vetoed the candidates with the dimuon mass in $[3036, 3156] \cup [3625, 3745]$ MeV/c^2 , under the reassignment of the muon mass to the pion candidates (and vice-versa), considering any combination of opposite-charged particles. Backgrounds can also originate from double misidentification between pions and muons. We expect a negligible contribution from $B_{(s)}^0 \rightarrow D_{(s)}^- (\rightarrow 3\pi) \pi^+$ decays, where the two pions are misidentified as two muons, whose

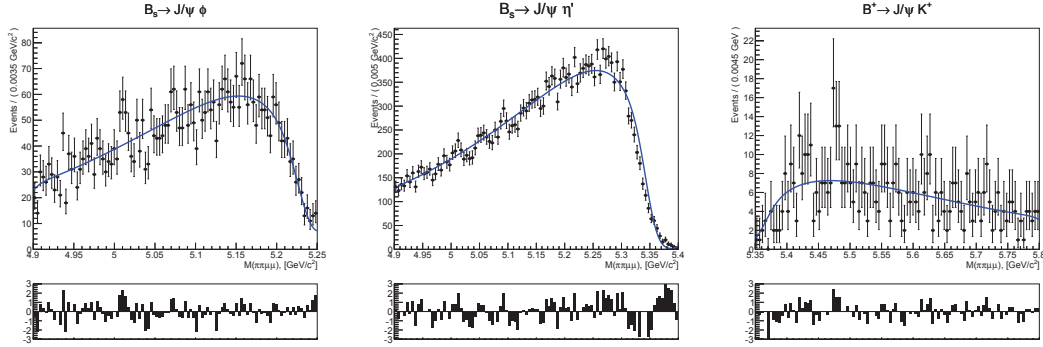


Figure 4.9 – Distributions of MC data for partially- and over-reconstructed decays with fit projections overlaid. The left plot shows $B_s^0 \rightarrow J/\psi\phi$, the middle plot $B_s^0 \rightarrow J/\psi\eta'$, and the right plot the $B^+ \rightarrow J/\psi K^+$ decays. The distributions are fitted with Argus functions convolved with a Gaussian with width fixed to the value found for the signal decays ($\approx 20 \text{ MeV}/c^2$).

selection efficiency is $\mathcal{O}(10^{-5})$ smaller than the signal efficiency due to the low μ - π misidentification rate and the fact that the tracks from $D_{(s)}^-$ decays are displaced from the B vertex, given the $D_{(s)}^-$ lifetime.

4.2.6 Wrongly reconstructed decays

We also consider peaking backgrounds due to decays that are not properly reconstructed, either because a track of the decay is not associated to the candidate (“partially reconstructed”), or because a random track is wrongly associated to the decay vertex during the reconstruction of the B candidate (“over reconstructed”).

In the first category, we have the two leading contributions in the resonant sample: the $B_s^0 \rightarrow J/\psi\phi(\rightarrow \pi^+\pi^-\pi^0)$ decays with a missing π^0 ; and the $B_s^0 \rightarrow J/\psi\eta'(\rightarrow X(\rightarrow \pi^+\pi^-)\gamma)$ decays with a missing γ . The invariant mass distributions of these partially reconstructed decays are shown in Figure 4.9. Analogous decays of the B^0 either do not enter the $J/\psi\pi^+\pi^-$ mass window (when missing a pion, for instance in $B^0 \rightarrow J/\psi\omega(\rightarrow \pi^+\pi^-\pi^0)$) or are suppressed and negligible. Over-reconstructed events originate from the $B^+ \rightarrow J/\psi K^+$ decays with an additional combinatorial pion and the kaon misidentified as a pion and from the $B^+ \rightarrow J/\psi\pi^+$ decays, with an additional combinatorial pion. We estimate a ratio R between yields of these background decays and the yield of $B^0 \rightarrow K^*(892)^0\mu^+\mu^-$ background (with dimuon pair within J/ψ mass window for the resonant channel and out of it for the signal) by calculating the relative branching ratios (from PDG [43]), taking into account the factor f_s/f_d for B_s^0 decays [51], and by determining the relative selection efficiencies with simulations. Table 4.6 reports the values of R for the different background decays, and the corresponding estimated yields, once the $B^0 \rightarrow J/\psi K^*(892)^0$ yield has been determined as described in Section 4.3.

In the signal sample we consider the following decays with non-resonant muon pairs: $B_s^0 \rightarrow \phi(\rightarrow \pi^+\pi^-\pi^0)\mu^+\mu^-$, $B_s^0 \rightarrow \eta'(\rightarrow X(\rightarrow \pi^+\pi^-)\gamma)\mu^+\mu^-$, $B^+ \rightarrow \pi^+\mu^+\mu^-$ and $B^+ \rightarrow K^+\mu^+\mu^-$. We es-

estimate the ratio R for their yields in data relative to the yield of misidentified $B^0 \rightarrow K^*(892)^0\mu^+\mu^-$ decays, by using the known branching ratios [43], the f_s/f_d factor for the B_s^0 decays [51] and the relative efficiency computed from simulations. Since no measurement of the branching fraction of $B_s^0 \rightarrow \eta'(\rightarrow X(\rightarrow \pi^+\pi^-)\gamma)\mu^+\mu^-$ is available for the estimation of this background, we assume that the leading amplitudes governing $B_s^0 \rightarrow \eta'\mu^+\mu^-$ and $B_s^0 \rightarrow J/\psi\eta'$ are respectively, the same of $B_s^0 \rightarrow \phi\mu^+\mu^-$ and $B_s^0 \rightarrow J/\psi\phi$, and calculate the expected $B_s^0 \rightarrow \eta'\mu^+\mu^-$ yield considering

$$\frac{\mathcal{B}(B_s^0 \rightarrow \phi\mu^+\mu^-)}{\mathcal{B}(B_s^0 \rightarrow J/\psi\phi)} \approx \frac{\mathcal{B}(B_s^0 \rightarrow \eta'\mu^+\mu^-)}{\mathcal{B}(B_s^0 \rightarrow J/\psi\eta')}. \quad (4.6)$$

The yields of the partially reconstructed decays are found to be much smaller than the yield of the misidentified $B^0 \rightarrow K^*(892)^0\mu^+\mu^-$ decays (see Table 4.6).

Decay mode	2011 sample		2012 sample	
	R	Yield	R	Yield
$B_s \rightarrow J/\psi\eta'$	0.271 ± 0.057	208 ± 44	0.218 ± 0.046	408 ± 86
$B_s^0 \rightarrow J/\psi\phi$	0.0455 ± 0.0073	35.0 ± 5.6	0.0427 ± 0.0068	80 ± 13
$B^+ \rightarrow J/\psi K^+$	0.0841 ± 0.0025	64.7 ± 1.9	0.0844 ± 0.0025	158.3 ± 4.7
$B_s \rightarrow \eta'\mu^+\mu^-$	0.308 ± 0.065	2.06 ± 0.48	0.327 ± 0.069	5.0 ± 1.2
$B_s^0 \rightarrow \phi\mu^+\mu^-$	0.0517 ± 0.0083	0.346 ± 0.065	0.0467 ± 0.0075	0.72 ± 0.14
$B^+ \rightarrow K^+\mu^+\mu^-$	0.0960 ± 0.0029	0.640 ± 0.067	0.1148 ± 0.0034	1.76 ± 0.18

Table 4.6 – Yields of partially- and over-reconstructed decays.

Semileptonic decays $B^0 \rightarrow D^-(\rightarrow \rho^0\mu^-X)\mu^+X$ are found to have a negligible tail within the considered region of the $\pi\pi\mu\mu$ invariant mass.

4.2.7 Selection efficiencies

We determine the the selection efficiencies $\varepsilon(B_s^0 \rightarrow \pi^+\pi^-\mu^+\mu^-)$, $\varepsilon(B^0 \rightarrow \pi^+\pi^-\mu^+\mu^-)$, and $\varepsilon(B^0 \rightarrow J/\psi K^*(892)^0)$, to determine the relative efficiencies entering equations 4.3 and 4.4. The selection efficiency for a given decay can be factorised as follows:

$$\mathcal{E} = \varepsilon_{\text{acc}} \times \varepsilon_{\text{trig}} \times \varepsilon_{\text{pres}} \times \varepsilon_{\text{BDT}} \times \varepsilon_{\text{PID}}, \quad (4.7)$$

where ε_{acc} is the geometrical efficiency, defined by the detector acceptance; $\varepsilon_{\text{trig}}$ is the trigger efficiency; $\varepsilon_{\text{pres}}$ is the efficiency of the preselection (including stripping); ε_{BDT} is the efficiency of the BDT selection; ε_{PID} is the efficiency of the PID selection.

All of them, but ϵ_{PID} , are determined from simulations as

$$\epsilon_y = \frac{N(\text{selected})}{N(\text{input})}, \quad (4.8)$$

being $N(\text{selected})$ the number of events that pass the selection y , and $N(\text{input})$ the number before the considered selection. The efficiency of the PID selection is calculated by using the PIDCalib package¹ [52], except for the efficiency of the requirement on $\text{ProbNN}(\mu)$, which is estimated with simulation. Efficiency of a certain PID requirement on a certain particle is found as an average efficiency among all tracks of this type in a simulated sample:

$$\epsilon = \frac{\sum_{i=1}^N \epsilon_i(p_i, \eta_i, nTracks_i)}{N} \quad (4.9)$$

Here, the summation is performed over all decay candidates and $\epsilon_i(p_i, \eta_i, nTracks_i)$ is the efficiency of a PID requirement for i -th decay candidate, estimated from the data in bins of $(p_i, \eta_i, nTracks_i)$ of a track.

The estimated efficiencies with their uncertainties are reported in Table 4.7, where the uncertainty is defined by the size of the sample used in the estimation. Table 4.8 details the efficiencies entering the third column of Table 4.7 ($\epsilon_{\text{trig}} \epsilon_{\text{pres}} \epsilon_{\text{BDT}}$), in order to compare each contribution for the signal and the normalisation decay modes; as expected, the efficiencies are very similar between the $B_{(s)}^0 \rightarrow \pi^+ \pi^- \mu^+ \mu^-$ and $B^0 \rightarrow J/\psi K^* (892)^0$ decays, a part from the selection efficiency of the $\mu^+ \mu^-$ mass regions; also, the BDT efficiency shows some differences, since the BDT was optimised for observation of the $B_s^0 \rightarrow \pi^+ \pi^- \mu^+ \mu^-$ decays; the muon PID efficiencies differ due to the different region of q^2 associated with resonant and non-resonant samples.

Sample	$\epsilon_{\text{acc}}(\%)$	$\epsilon_{\text{trig}} \epsilon_{\text{pres}} \epsilon_{\text{BDT}}(\%)$	$\epsilon_{\text{PID}}(\%)$	Total (%)
2011				
$B_s^0 \rightarrow \pi^+ \pi^- \mu^+ \mu^-$	14.26 ± 0.076	5.026 ± 0.033	50.345 ± 0.092	0.3608 ± 0.0031
$B^0 \rightarrow \pi^+ \pi^- \mu^+ \mu^-$	14.49 ± 0.049	4.211 ± 0.015	48.755 ± 0.05	0.2975 ± 0.0015
$B^0 \rightarrow J/\psi K^* (892)^0$	14.87 ± 0.039	7.4619 ± 0.0089	8.407 ± 0.043	0.0933 ± 0.0005
2012				
$B_s^0 \rightarrow \pi^+ \pi^- \mu^+ \mu^-$	15.48 ± 0.076	5.174 ± 0.032	46.062 ± 0.096	0.3689 ± 0.0030
$B^0 \rightarrow \pi^+ \pi^- \mu^+ \mu^-$	15.64 ± 0.049	4.103 ± 0.029	42.813 ± 0.11	0.2748 ± 0.0022
$B^0 \rightarrow J/\psi K^* (892)^0$	16.05 ± 0.039	6.688 ± 0.027	9.075 ± 0.056	0.0974 ± 0.0008

Table 4.7 – Efficiencies of the signal and normalisation decays. The column ϵ_{PID} does not include the efficiency of the $\text{ProbNN}(\mu)$ requirement, which is included in ϵ_{pres} (see Table 4.8).

The following uncertainties are considered:

¹A standard LHCb package based on tabulated PID efficiencies extracted from control samples of data.

Statistical uncertainty of the simulation samples. In case of efficiencies estimated with the PIDCalib, we consider the errors due to the limited size of our simulation samples used to reweight the calibrations samples, and the size of the calibration samples of the PIDCalib package.

Model dependence of efficiencies. This uncertainty is caused by the limited knowledge of the decay models for the Monte-Carlo (MC) simulation of the $B_{(s)}^0 \rightarrow \pi^+\pi^-\mu^+\mu^-$ samples; the main contribution comes from the unknown angular distributions of the products of the $B_{(s)}^0 \rightarrow \pi^+\pi^-\mu^+\mu^-$ decay, which may lead to the different detection efficiencies. In order to estimate contributions from this source, we consider two alternative models, one for the $B_{(s)}^0 \rightarrow \pi^+\pi^-\mu^+\mu^-$ generated with the angular distributions predicted in Refs. [53, 54], and one generated with the phase-space model. As uncertainty we take the relative difference of the efficiency calculated for the two models, which yields 5.4%.

Discrepancies between the simulation and data in the trigger description. Such uncertainties are caused by the limited capability of the simulation to describe the trigger selection efficiencies. The relative uncertainties on the efficiencies of $B_{(s)}^0 \rightarrow \pi^+\pi^-\mu^+\mu^-$ and $B^0 \rightarrow J/\psi K^*(892)^0$ decays are assumed to be the same. Using the $B^0 \rightarrow J/\psi K^*(892)^0$ data sample and the TISTOS method [55], we find that the trigger efficiencies in simulation studies differs from the efficiencies in data by 0.5% in 2011 and 2.1% in 2012. We assign these differences as systematic uncertainties to both signal and normalisation efficiencies, and consider them as uncorrelated.

Discrepancies between the simulation and data for BDT and ProbNN(μ) variables These uncertainties are related to the inaccurate simulation of some relevant distributions, like the B transverse momentum or the ProbNN(μ) variable, that can result in a wrong estimation of the efficiencies of the BDT selection and of the ProbNN(μ) requirement. For the BDT selection, we use the $B^0 \rightarrow J/\psi K^*(892)^0$ data sample to estimate the selection efficiency in data, and we compare it with the value obtained in the simulation. We take the differences of the two estimations as the systematic uncertainty, and we assume that the relative uncertainties on the efficiencies of $B_{(s)}^0 \rightarrow \pi^+\pi^-\mu^+\mu^-$ and $B^0 \rightarrow J/\psi K^*(892)^0$ decays are the same. We assign these systematic uncertainties to both signal and normalisation efficiencies, consider them as uncorrelated, as a cancellation of the errors in the efficiency ratio is not necessarily realized. The relative systematic uncertainties are 3.7% in 2011, and 2.1% in 2012. For the ProbNN(μ) requirement, we have compared the efficiency estimated in MC with the one obtained from the PIDCalib package for $B^0 \rightarrow J/\psi K^*(892)^0$ decays, and we take the difference as systematic uncertainty. The relative errors in this case are 0.1% for both 2011 and 2012.

B lifetime Since the B -lifetime enters the BDT inputs, the relative efficiency for the B_s^0 selection has an additional relative uncertainty of 1.6% caused by the uncertainty of the B_s^0 lifetime estimate for the $B_s^0 \rightarrow \pi^+\pi^-\mu^+\mu^-$ decays [56], and the B^0 lifetime estimate for the $B^0 \rightarrow J/\psi K^*(892)^0$ decays. To estimate this uncertainty, we compare the nominal selection efficiency with the one obtained from the reweighted simulation samples,

4.3. Study of misidentified backgrounds

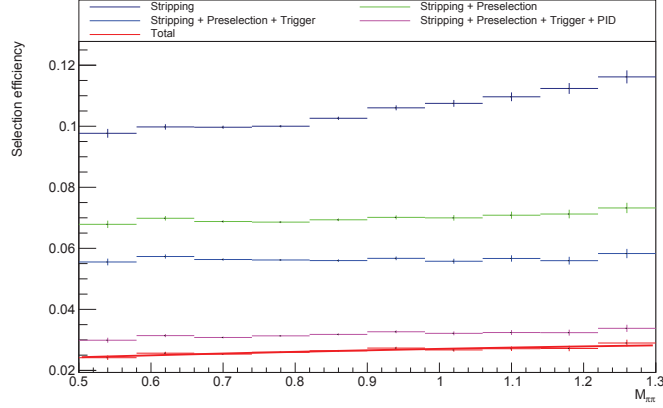


Figure 4.10 – Dependence of the selection efficiency (for different steps of the selection) as a function of the $\pi^+\pi^-$ mass for MC data. Here, with “preselection” we consider the $\mu^+\mu^-$ mass requirements, while the BDT is applied in the last step (Total).

where the reweighting procedure simulates generation of the decay candidates with another lifetime. In order to estimate the possible variation of the B_s^0 lifetime, we varied with $\pm 1\sigma$ (from the world average values in HFAG [57]) both Γ_L and Γ_H values used for the lifetime used in simulation, which is $\Gamma_s = 0.5(\Gamma_H + \Gamma_L)$. Uncertainty for the B^0 lifetime is taken into account in the same way.

We also check the efficiency as a function of the $\pi^+\pi^-$ invariant mass, as reported in Figure 4.10; this is important to quote the visible branching fraction of $B_{(s)}^0 \rightarrow \pi^+\pi^-\mu^+\mu^-$ in the $[0.5, 1.3] \text{ GeV}/c^2$ $\pi^+\pi^-$ mass window. The total selection induces an efficiency that has a quadratic dependence along the $\pi^+\pi^-$ mass spectrum with variation of the order of 2%; we fit that dependence to extract a correction function that is used to reweight, event-by-event, the data sample, in order to yield a uniform efficiency distribution in the $\pi^+\pi^-$ spectrum.

4.3 Study of misidentified backgrounds

Misidentified background from the $B^0 \rightarrow K^*(892)^0\mu^+\mu^-$ decay significantly affects the measurement of branching fraction of the $B^0 \rightarrow \pi^+\pi^-\mu^+\mu^-$ decay. Since the background candidates from this source are very close kinematically to the signal candidates, the only way to suppress them is to impose requirements on the quality of particle identification, PID. Unfortunately, PID variables are known to be poorly described within the LHCb simulation, so one needs to find a data-based method to suppress and control these backgrounds. Such method is described here. Its underlying idea is to use a properly reconstructed sample of $B^0 \rightarrow K^*(892)^0\mu^+\mu^-$ decays to emulate the misidentification and use this well-controlled sample for optimisation of the PID selection and modeling of the background contribution to the

Sample	Stripping	2011			2012			$M_{\mu\mu}$	$\mu - \pi$ veto	ϕ veto	Binning scheme	$K\pi$ window	BDT	PID(μ)
		L0	HLT1	HLT2	L0	HLT1	HLT2							
$B_s^0 \rightarrow \pi^+ \pi^- \mu^+ \mu^-$	0.11585 ± 0.00052	0.8764 ± 0.0054	0.9547 ± 0.0062	0.9523 ± 0.0063	0.7115 ± 0.0052	0.9929 ± 0.0079	0.9961 ± 0.0079	0.9552 ± 0.0077	–	0.8444 ± 0.0072	0.9595 ± 0.0086			
$B^0 \rightarrow \pi^+ \pi^- \mu^+ \mu^-$	0.10283 ± 0.00024	0.8979 ± 0.0029	0.9607 ± 0.0033	0.9604 ± 0.0033	0.6684 ± 0.0026	0.9839 ± 0.0043	0.9879 ± 0.0043	0.9565 ± 0.0042	–	0.8043 ± 0.0037	0.9692 ± 0.0048			
$B^0 \rightarrow J/\psi K^* (892)^0$	0.22593 ± 0.00017	0.90723 ± 0.00087	0.96485 ± 0.00096	0.96535 ± 0.00098	0.95051 ± 0.00098	–	–	–	0.5147 ± 0.0065	0.8198 ± 0.0013	0.9746 ± 0.0016			
$B_s^0 \rightarrow \pi^+ \pi^- \mu^+ \mu^-$	0.11706 ± 0.00050	0.8473 ± 0.0051	0.9622 ± 0.0061	0.9706 ± 0.0062	0.7117 ± 0.0050	0.9911 ± 0.0076	0.9958 ± 0.0077	0.9656 ± 0.0075	–	0.8598 ± 0.0070	0.9578 ± 0.0082			
$B^0 \rightarrow \pi^+ \pi^- \mu^+ \mu^-$	0.09935 ± 0.00047	0.8761 ± 0.0057	0.9659 ± 0.0066	0.9748 ± 0.0067	0.6693 ± 0.0052	0.9932 ± 0.0085	0.9876 ± 0.0085	0.9553 ± 0.0083	–	0.8231 ± 0.0076	0.9603 ± 0.0094			
$B^0 \rightarrow J/\psi K^* (892)^0$	0.21035 ± 0.0005	0.8723 ± 0.0028	0.9701 ± 0.0032	0.9767 ± 0.0033	0.9453 ± 0.0032	–	–	–	0.5158 ± 0.0022	0.8189 ± 0.0042	0.9635 ± 0.0052			

Table 4.8 – Detailed efficiency table for $\mathcal{E}_{\text{trig}} \mathcal{E}_{\text{pres}} \mathcal{E}_{\text{BDT}}$ (see Table 4.7); with “Binning scheme” we consider the effect of removing the events that are out of the kinematical range that can be used in the PIDCalib package.

final fit.

4.3.1 Selection of a clean $B^0 \rightarrow J/\psi K^* (892)^0$ sample

In order to emulate the $K - \pi$ misidentification rate in data associated with a given PID requirement on the $DLL(\pi - K)$ variable, a clean sample of properly-reconstructed $B^0 \rightarrow J/\psi K^* (892)^0$ candidates is needed. For this, candidates from the normalisation sample are selected through the same stripping line and selection requirements as the resonant sample (including BDT requirements). In addition, a $DLL(\pi - K) < -5$ requirement is applied for the kaon track, which strongly suppresses misidentification of this particle with a $\sim 9\%$ penalty in signal efficiency. Pion tracks are required to meet the requirement $DLL(\pi - K) > X$, where X is the tested threshold. An identical procedure is used for $B^0 \rightarrow K^* (892)^0 \mu^+ \mu^-$ decays contributing to the non-resonant sample.

4.3.2 sWeights for further background suppression

The $K\pi\mu\mu$ invariant mass distribution of the selected candidates is fitted as shown in Figure 4.11(left) with model consisting of

- Two double Crystal Ball functions to describe the $B^0 \rightarrow J/\psi K^* (892)^0$ and $B_s^0 \rightarrow J/\psi K^* (892)^0$ peaks;
- An exponential function to describe the combinatorial background;
- A mirrored Argus function to describe the small contamination from $B^+ \rightarrow J/\psi K^+$ decays with a combinatorial pion. This function is convolved with a Gaussian function with the same width of the principal Crystal Ball of the signal;
- An Argus function to describe partially reconstructed candidates. This function is convolved with a Gaussian function with the same width of the signal Crystal Ball.

From this fit we obtain sWeights [58] to unfold the $B^0 \rightarrow J/\psi K^* (892)^0$ component. A similar procedure is applied for $B^0 \rightarrow K^* (892)^0 \mu^+ \mu^-$ decays. Due to the smaller sample size, it is possible to simplify the fit, considering only the main components, which are the $B^0 \rightarrow K^* (892)^0 \mu^+ \mu^-$ signal and the combinatorial background. The resulting fit to the data is presented in Figure 4.12(left).

4.3.3 Emulation of misidentification

With a signal-only, sWeighted $B^0 \rightarrow J/\psi K^* (892)^0$ sample, we can emulate the misidentification. This includes assignation of a pion mass to the kaon tracks; reweighing of each

candidate with $\epsilon[\text{DLL}(\pi\text{-K})>X]/\epsilon[\text{DLL}(\pi\text{-K})<-5]$ to account for the selection PID efficiency for the misidentified candidates; and the application of the cut to the invariant dipion mass: $M_{\pi\pi} \in [0.5, 1.3] \text{ GeV}/c^2$. Both PID selection efficiencies are calculated as functions of $(p, \eta, nTracks)$ with means of PIDCalib package [52] and thus depend on the kinematics properties of the track and the track multiplicity of the event. The misidentification emulation procedure is the same for the $B^0 \rightarrow K^*(892)^0\mu^+\mu^-$ decays contributing to the non-resonant sample.

4.3.4 Extraction of the background shape

The misidentified $B^0 \rightarrow K^*(892)^0\mu^+\mu^-$ mass distribution is described by a Crystal Ball function as shown in Figure 4.12(center), while the $B^0 \rightarrow J/\psi K^*(892)^0$ mass distribution is described with a sum two Gaussian functions, each with free mean and width as shown in Figure 4.11(center). Red lines in Figure 4.11(center) represent two Gaussians, the final shape is shown in blue. Parameters of the background shapes (except for the location in mass of the PDF) are fixed from the fit of the emulated $\pi\pi\mu\mu$ mass distribution to the values reported in Tables 4.9 and 4.10. Since the fit range of the resonance and signal samples starts from $5.19 \text{ GeV}/c^2$, the yield of the misidentified background contribution to the $\pi\pi\mu\mu$ mass fit depends on the shape of the distribution.

The dependence of the yield from the mass transitions of the PDF is defined as follows:

$$Y_{\text{misid}}(\hat{M}) = \int_{5.19 + M_{\text{misid}} - \hat{M}_{\text{misid}}}^{+\text{inf}} \text{PDF}(m) dm, \quad (4.10)$$

where $Y_{\text{misid}}(\hat{M})$ is the yield and M_{misid} is a parameters defining the position of the PDF defined during the emulation of the misidentification. Right plots of Figures 4.12 and 4.11 illustrate the dependence of the background yield from the position of the background PDF in fit to the $\pi\pi\mu\mu(J/\psi)$ invariant mass (“PDF” curve). The “Data” curve on these plots is obtained in the same way with the data distribution used instead of the PDF and serves demonstrational purposes. PDF curve is parametrised with the quadratic function

$$Y_{\text{misid}}(\hat{M}) = a + b\hat{M} + c\hat{M}^2, \quad (4.11)$$

where $Y_{\text{misid}}(\hat{M})$ is the yield of the misidentified background in the $\pi\pi\mu\mu$ mass fit, \hat{M} is the position² of the peak of the distribution, and a , b , and c are numerical parameters. The parameters a , b and c are determined from the fit of the PDF curve and the resulting parametrisation is shown in the right plots in Figures 4.12 and 4.11 as “Fit” curve.

The estimated yields of the $B^0 \rightarrow K^*(892)^0\mu^+\mu^-$ and $B^0 \rightarrow J/\psi K^*(892)^0$ contributions are Gaussian constrained in the fit of the $\pi\pi\mu\mu$ invariant mass distribution of the signal and

²which is the mean of the first Gaussian in case of $B^0 \rightarrow J/\psi K^*(892)^0$ or the mean of the Crystal Ball in the case of $B^0 \rightarrow K^*(892)^0\mu^+\mu^-$

resonance channels, by means of

$$\exp \left[-\frac{(N_{\text{misid}} - N_{\text{est}}(M_{\text{misid}}))^2}{2\sigma_{N_{\text{est}}}^2} \right], \quad (4.12)$$

where N_{misid} are the yields of the misidentified background, floating in the fit; $N_{\text{est}}(M_{\text{misid}})$ are the yields estimated through the equation. 4.11, and $\sigma_{N_{\text{est}}}$ are their associated errors, discussed below.

Parameter	2011 sample	2012 sample
Mean 1st gauss, [GeV/c ²]	5.229 ± 0.033	5.2352 ± 0.0042
Width 1st gauss, [GeV/c ²]	0.0217 ± 0.0060	0.0165 ± 0.0048
fraction 1st gauss	0.56 ± 0.48	0.25 ± 0.13
Mean 2nd gauss, [GeV/c ²]	5.198 ± 0.027	5.21 ± 0.0039
Width 2nd gauss, [GeV/c ²]	0.0333 ± 0.0057	0.0327 ± 0.0014

Table 4.9 – Parameters of the mis-identified $B^0 \rightarrow J/\psi K^*(892)^0$ PDF.

Parameter	2011 sample	2012 sample
Mean CB, [GeV/c ²]	5.2345 ± 0.0055	5.224 ± 0.012
Width CB, [GeV/c ²]	0.0226 ± 0.005	0.0271 ± 0.0079
tail parameter n	115 ± 11	115 ± 33
tail parameter α	0.84 ± 0.38	0.63 ± 0.57

Table 4.10 – Parameters of the mis-identified $B^0 \rightarrow K^*(892)^0 \mu^+ \mu^-$ PDF.

4.3.5 Uncertainty of the method

For a given value of M_{misid} (called \hat{M}_{misid} in the following) the uncertainties on the yield estimation of $B^0 \rightarrow K^*(892)^0 \mu^+ \mu^-$ and $B^0 \rightarrow J/\psi K^*(892)^0$ decays are computed as follows. Consider the estimation of the $B^0 \rightarrow J/\psi K^*(892)^0$ yield. The number of events resulting from procedure described above is given by the sum over all events in the selected sample of the product of the sWeights and the relative PID efficiencies, $\varepsilon^{\text{PID}} = \varepsilon[\text{DLL}(\pi - K) > 1] / \varepsilon[\text{DLL}(\pi - K) < -5]$. The PIDCalib package provides an estimation of the PID efficiencies in bins of the particles momentum and pseudorapidity, and the number of tracks in the event, from tables of efficiencies calculated on large samples of calibration channels. The package provides also uncertainties on the estimated efficiencies, which are dominated by the size of the calibration samples. We write the estimated number of events as follows:

$$N_{\text{misid}}(\hat{M}_{\text{misid}}) = \sum_{\text{bin}} \varepsilon_{\text{bin}}^{\text{PID}} N_{\text{bin}}, \quad (4.13)$$

Chapter 4. Search for $B \rightarrow \pi\pi\mu\mu$ decays

where N_{bin} is the number of events in a given bin, $N_{\text{bin}} = \sum_i \text{sWeight}_i$. The uncertainty on $N_{\text{misid}}(\hat{M}_{\text{misid}})$ is then defined as

$$\sigma_N = \sqrt{\sum_{\text{bin}} \left[(\varepsilon_{\text{bin}}^{\text{PID}} \delta N_{\text{bin}})^2 + (\delta \varepsilon_{\text{bin}}^{\text{PID}} N_{\text{bin}})^2 \right]}, \quad (4.14)$$

where δN_{bin} is the uncertainty on N_{bin} , given by the error on the yield estimated from the fit to extract the sWeights of the events entering the bin; $\delta \varepsilon_{\text{bin}}^{\text{PID}}$ is the uncertainty on the relative efficiency of the bin, computed by propagating the error on the efficiency provided by the PIDCalib package. The relative errors on $N_{\text{misid}}(\hat{M}_{\text{misid}})$ for the $B^0 \rightarrow J/\psi K^*(892)^0$ background are estimated to be 1.8% in 2011 data and 1% in 2012 data.

For $B^0 \rightarrow K^*(892)^0 \mu^+ \mu^-$ decays, to reduce the effect of statistical fluctuations on the error estimation, we assume that $B^0 \rightarrow K^*(892)^0 \mu^+ \mu^-$ and $B^0 \rightarrow J/\psi K^*(892)^0$ are distributed in the same way in the 3-dimensional bins of the PID efficiency, and consider a scale factor $m = N(B^0 \rightarrow K^*(892)^0 \mu^+ \mu^-) / N(B^0 \rightarrow J/\psi K^*(892)^0)$; with this approximation we calculate the error of the $B^0 \rightarrow K^*(892)^0 \mu^+ \mu^-$ yield as

$$\sigma_N = \sqrt{\sum_{\text{bin}} \left[(\varepsilon_{\text{bin}}^{\text{PID}} \delta N_{\text{bin}} \sqrt{m})^2 + (\delta \varepsilon_{\text{bin}}^{\text{PID}} N_{\text{bin}} m)^2 \right]}. \quad (4.15)$$

The relative errors on $N_{\text{misid}}(\hat{M}_{\text{misid}})$ for the $B^0 \rightarrow K^*(892)^0 \mu^+ \mu^-$ background are estimated to be 15% for 2011 and 10% for 2012.

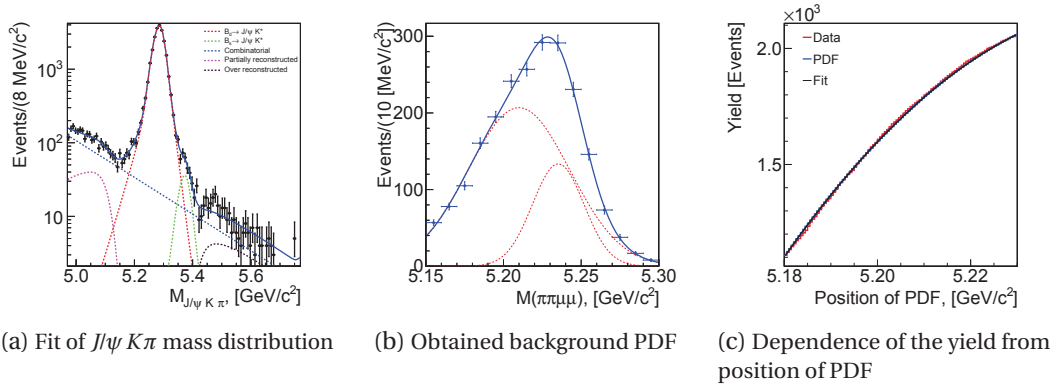


Figure 4.11 – Mass distributions of $B^0 \rightarrow J/\psi K^*(892)^0$ with fit projections overlaid (left), background PDF obtained with misidentification emulation (center) and position dependence of the yield of corresponding background to the fit of the resonance sample. All plots are obtained with for the 2012 data set.

4.4 Fits to the data

Yields of decays in the normalisation, resonant and signal samples used in equations 4.3 and 4.4 of Section 4.1 are determined from an unbinned maximum likelihood fit to the $J/\psi K^*(892)^0$

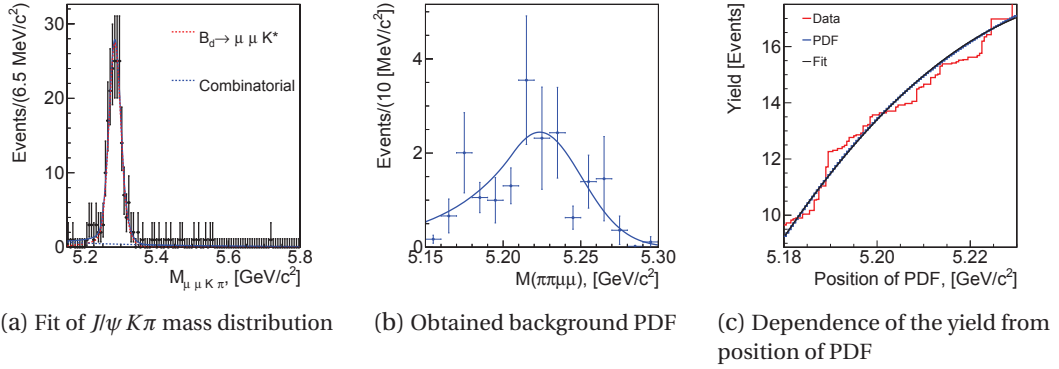


Figure 4.12 – Mass distributions of $B^0 \rightarrow K^*(892)^0 \mu^+ \mu^-$ with fit projections overlaid (left), background PDF obtained with misidentification emulation (center) and position dependence of the yield of corresponding background to the fit of the resonance sample. All plots are obtained for the 2012 data set.

mass distribution (normalisation), and from an unbinned maximum likelihood simultaneous fit of the $\pi^+ \pi^- \mu^+ \mu^-$ (signal) and the $J/\psi \pi^+ \pi^-$ (resonant) mass distributions. All fits are done using the RooFit package [59]. The data sample is split according to the data-taking year.

4.4.1 Fit to the normalisation channel

The normalisation sample, which contains $B^0 \rightarrow J/\psi K^*(892)^0$ decay candidates, is selected by the same requirements employed for the $\pi^+ \pi^- \mu^+ \mu^-$ data selection (including the BDT), but requiring $\text{DLL}(\pi - K) < -5$ instead of $\text{DLL}(\pi - K) > 1$. The invariant mass of the $K\pi$ pair is required to be within the narrow [826, 966] MeV window around the $K^*(892)^0$ mass; we use the same mass window as in Ref. [60] in order to subtract from our result the $B^0 \rightarrow J/\psi K\pi$ S-wave contribution measured in that analysis.

We fit the $J/\psi K\pi^3$ mass spectrum from 4.97 to 5.77 GeV/c^2 by means of the following model. We use a sum of two Crystal Ball functions for the $B^0 \rightarrow J/\psi K^*(892)^0$ and $B_s^0 \rightarrow J/\psi K^*(892)^0$ signals; all parameters (except the Crystal Ball tails, which are fixed to the values obtained during the fit of the simulations) are floating in the fit and common between the B^0 and B_s^0 signal, with the B_s^0 peak shifted by the fixed mass difference of B_s^0 and B^0 mesons. An exponential function is used to describe the combinatorial background. A small contamination of over reconstructed $B^+ \rightarrow J/\psi K^+$ decays is present in the right side-band, and modeled with a mirrored Argus function [61] with starting point fixed to the sum of the π^+ and B^+ masses. Partially reconstructed decays in the left side-band are described with another Argus function. Both over and partially reconstructed shapes are convolved with a Gaussian function with the same width of the principal Crystal Ball of the signal.

³The invariant mass of the dimuon pair of the decay candidates in this sample is within the [2.796, 3.216] GeV/c^2 mass window, but is not constrained to the J/ψ mass.

Chapter 4. Search for $B \rightarrow \pi\pi\mu\mu$ decays

The 2011 and 2012 samples are fitted independently. We report the fit results in Table 4.11, and in Figure 4.13 we show fit projections. The $B^0 \rightarrow J/\psi K^* (892)^0$ signal comprises about 10500 and 25100 events respectively in the 2011 and 2012 data sets. We correct these numbers to subtracted the $B^0 \rightarrow J/\psi K\pi$ S -wave contribution, $(6.4 \pm 1.0)\%$ from Ref. [60], and obtain

$$N_{2011}(B^0 \rightarrow J/\psi K^* (892)^0) = 9821 \pm 110 (\text{stat}) \pm 134 (\text{syst}) \pm 97 (S\text{-wave}), \quad (4.16)$$

$$N_{2012}(B^0 \rightarrow J/\psi K^* (892)^0) = 23521 \pm 175 (\text{stat}) \pm 172 (\text{syst}) \pm 243 (S\text{-wave}). \quad (4.17)$$

Systematic uncertainties considered are due to the variations of the shape parameters fixed in the fit to the values found in the simulation. We generate a set of values by sampling the parameters within a multidimensional Gaussian function defined by the covariance matrix of the fits to simulation; we fix the obtained parameters and perform the fit to the data; we repeat 1000 times the sampling and the fit, and we plot the distribution of the difference between the fitted yields and their values from the default fit. We consider as a systematic uncertainty the r.m.s. spread of this distribution.

Parameter	2011 sample	2012 sample
Yield of $B^0 \rightarrow J/\psi K^* (892)^0$	10493 ± 110	25129 ± 176
Width of first CB, [GeV/ c^2]	0.01896 ± 0.00018	
Ratio of CB widths	0.741 ± 0.044	
Ratio of CB	0.741 ± 0.015	
Part.reco'd Argus shape c	-19 ± 11	
Part.reco'd Argus starting point, [GeV/ c^2]	5.1235 ± 0.0063	
B^0 mass, [GeV/ c^2]	5.28521 ± 0.00022	
Combinatorial slope, [c^2 /GeV]	-5.49 ± 0.75	-5.77 ± 0.47
Yield of partially reconstructed	349 ± 79	911 ± 142
Combinatorial yield	938 ± 119	2712 ± 227
Yield of $B_s^0 \rightarrow J/\psi K^* (892)^0$	100 ± 18	219 ± 31
Yield of $B^+ \rightarrow J/\psi K^+$	48 ± 26	131 ± 44

Table 4.11 – Results of the fit to the $B^0 \rightarrow J/\psi K^* (892)^0$ data.

4.4.2 Likelihood of the $\pi\pi\mu\mu$ and $J/\psi\pi\pi$ sample

By using the equations 4.3 and 4.4, we write the numbers of events of $B_s^0 \rightarrow \pi^+\pi^-\mu^+\mu^-$ and $B^0 \rightarrow \pi^+\pi^-\mu^+\mu^-$ decays in the 2011 and 2012 data sets as follows:

$$N(B_s^0 \rightarrow \pi^+\pi^-\mu^+\mu^-)_{\text{year}} = \frac{f_s}{f_d} \frac{N_{\text{year}}(B^0 \rightarrow J/\psi K^* (892)^0)}{\epsilon_{\text{rel,year}}^s} \mathcal{R}_s, \quad (4.18)$$

$$N(B^0 \rightarrow \pi^+\pi^-\mu^+\mu^-)_{\text{year}} = \frac{N_{\text{year}}(B^0 \rightarrow J/\psi K^* (892)^0)}{\epsilon_{\text{rel,year}}^d} \mathcal{R}_d, \quad (4.19)$$

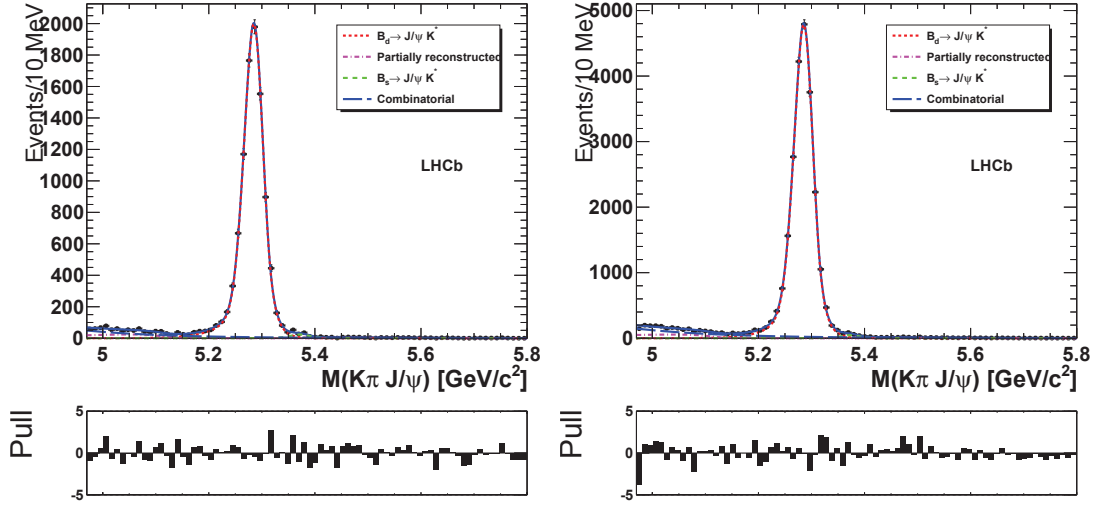


Figure 4.13 – Mass distribution of $B^0 \rightarrow J/\psi K^*(892)^0$ candidates with fit projections overlaid. Left and right plots are respectively the 2011 and 2012 data sets.

where the numbers of $B^0 \rightarrow J/\psi K^*(892)^0$ events are measured in the previous section; the efficiencies are evaluated in Section 4.2.7; the factor f_s/f_d is taken as an external input [51]; and

$$\mathcal{R}_s = \frac{\mathcal{B}(B_s^0 \rightarrow \pi^+ \pi^- \mu^+ \mu^-)}{\mathcal{B}(B^0 \rightarrow J/\psi K^*(892)^0)}, \quad (4.20)$$

$$\mathcal{R}_d = \frac{\mathcal{B}(B^0 \rightarrow \pi^+ \pi^- \mu^+ \mu^-)}{\mathcal{B}(B^0 \rightarrow J/\psi K^*(892)^0)}, \quad (4.21)$$

are the quantities that we want to measure. By using this parametrisation we can simultaneously fit the 2011 and 2012 data sample, using directly \mathcal{R}_s and \mathcal{R}_d as floating parameters. Since the correction for $\frac{f_s}{f_d}$ is independent from the year, and can be applied after to the fit results, we prefer (to reduce a number of constants in the code) to fit with the parameters

$$\mathcal{R}'_s = \frac{f_s}{f_d} \frac{\mathcal{B}(B_s^0 \rightarrow \pi^+ \pi^- \mu^+ \mu^-)}{\mathcal{B}(B^0 \rightarrow J/\psi K^*(892)^0)} (1 - f_{Sw}) \equiv \frac{f_s}{f_d} \mathcal{R}_s (1 - f_{Sw}), \quad (4.22)$$

$$\mathcal{R}'_d = \frac{\mathcal{B}(B^0 \rightarrow \pi^+ \pi^- \mu^+ \mu^-)}{\mathcal{B}(B^0 \rightarrow J/\psi K^*(892)^0)} (1 - f_{Sw}) \equiv \mathcal{R}_d (1 - f_{Sw}), \quad (4.23)$$

where the S -wave fraction, f_{Sw} , has not been subtracted in equation 4.18. To avoid biases toward larger values in case of zero (or small) signal yields, we allow \mathcal{R}'_s and \mathcal{R}'_d to take also negative values (corresponding to negative yields).

The joint likelihood of the $\pi^+ \pi^- \mu^+ \mu^-$ and $J/\psi \pi^+ \pi^-$ mass distributions, and of the 2011 and 2012 samples, is written as follows:

$$\mathcal{L}(m_1, m_2 | \xi) = \mathcal{L}_{2011}^{\mu^+ \mu^-}(m_1 | \xi_1) \mathcal{L}_{2011}^{J/\psi}(m_2 | \xi_2) \mathcal{L}_{2012}^{\mu^+ \mu^-}(m_1 | \xi'_1) \mathcal{L}_{2012}^{J/\psi}(m_2 | \xi'_2) \quad (4.24)$$

Chapter 4. Search for $B \rightarrow \pi\pi\mu\mu$ decays

where we call m_1 and m_2 the $\pi^+\pi^-\mu^+\mu^-$ and $J/\psi\pi^+\pi^-$ mass respectively, and ξ is a short-hand notation to represent the vector of the fitting parameters. The likelihood of each subsample is the product over the number of events (in the subsamples) of the probability density functions (PDF) describing each signal and background contributions of the mass spectrum:

$$\mathcal{L}_{\text{year}}^{(k)} = \prod \left[N_s^{(k)} \text{pdf}_s^{(k)} + N_d^{(k)} \text{pdf}_d^{(k)} + N_{\text{mis}}^{(k)} \text{pdf}_{\text{mis}}^{(k)} + N_{\text{comb}}^{(k)} \text{pdf}_{\text{comb}}^{(k)} + \sum_j N_{\text{part}}^{(j,k)} \text{pdf}_{\text{part}}^{(j,k)} \right] \quad (4.25)$$

where $N_i^{(k)}$ is the number of events of the contribution i described by the $\text{pdf}_i^{(k)}$ ($k = \mu^+\mu^-, J/\psi$); $i = s$, for the $B_s^0 \rightarrow \pi^+\pi^-\mu^+\mu^-$ ($B_s^0 \rightarrow J/\psi\pi^+\pi^-$) decays; $i = d$, for the $B^0 \rightarrow \pi^+\pi^-\mu^+\mu^-$ ($B^0 \rightarrow J/\psi\pi^+\pi^-$) decays; $i = \text{mis}$, for the misreconstructed $B^0 \rightarrow K^*(892)^0\mu^+\mu^-$ ($B^0 \rightarrow J/\psi K^*(892)^0$) background; $i = \text{comb}$, for the combinatorial background; $i = \text{part}$, for the different partially reconstructed decays. The 2011 and 2012 data are described by the same PDF, but some parameter may differ, as the efficiencies and yields fractions. In the following, we describe in detail all contributions.

Shapes of the $B_{(s)}^0 \rightarrow \pi^+\pi^-\mu^+\mu^-$ and $B_{(s)}^0 \rightarrow J/\psi\pi^+\pi^-$ mass distribution are obtained by fitting the simulation samples of these decays with a sum of two Crystal Ball functions, separately for the 2011 and 2012 simulations. In the fit to the data, all parameters are fixed to those values except for the mean of the B^0 signal peaks, and the width of the principal Crystal Ball of the signals, which is shared between B^0 and B_s^0 , with a scale factor, fixed from simulations, to account for the different width observed in simulations; the mean of the B_s^0 peaks is bound to the B^0 mean, by fixing the difference between the B_s^0 and B^0 mass from the PDG values. The two free parameters are in common between the resonant and the non-resonant sample. The widths of the B_s^0 and B^0 signals peak in the non-resonant sample are multiplied by average scale factors, derived from the ratio of the signal widths in the simulations of the non-resonant and resonant decay modes, to account for a dependence of the widths due to the different q^2 of the muons.

The combinatorial background is modeled with an exponential function, going from 5.19 to 6.99 GeV/ c^2 . The yields and slopes of the exponents are floating in the fit and different for each year and for the resonant and the non-resonant sample. To properly describe the data of the resonant sample around 6 GeV/ c^2 , we take into account a contribution from $B_c^+ \rightarrow J/\psi\pi^+\pi^-\pi^+$ decays, where one pion is not associated to the candidate in the reconstruction. The mass distribution is derived from the simulation and it is described by a sum of a Crystal Ball function and a Gaussian, with parameters fixed in the fit to the data.

Background decays from the π - K misidentification are $B^0 \rightarrow K^*(892)^0\mu^+\mu^-$ decays in the non-resonant sample; $B^0 \rightarrow J/\psi K^*(892)^0$ and $B_s^0 \rightarrow J/\psi K^*(892)^0$ decays in the resonant sample. Shapes and yields of the $B^0 \rightarrow (J/\psi \rightarrow)\mu\mu K^*(892)^0$ decays are extracted from the data with the procedure described in Section 4.3. The shape of the $B_s^0 \rightarrow J/\psi K^*(892)^0$ mass distribution is taken from the $B^0 \rightarrow J/\psi K^*(892)^0$ shape, shifted by the difference between the B_s^0 and B^0 mass. The yield of the $B_s^0 \rightarrow J/\psi K^*(892)^0$ decays is estimated by rescaling the $B^0 \rightarrow J/\psi K^*(892)^0$ yield with f_s/f_d [51], the relative branching fractions of the two decay modes (from PDG) and

considering the relative selection efficiencies (obtained from simulations); it corresponds to $(0.8 \pm 0.2)\%$ of the $B^0 \rightarrow J/\psi K^{*0}$ yield.

Other minor background decays considered in the resonant sample are partially and over-reconstructed decays described in Section 4.2.6, $B_s^0 \rightarrow J/\psi \phi (\rightarrow \pi^+ \pi^- \pi^0)$, $B_s^0 \rightarrow J/\psi \eta' (\rightarrow X (\rightarrow \pi^+ \pi^-) \gamma)$, and $B^+ \rightarrow J/\psi K^+$. Their mass distributions are modeled with Argus functions extracted from the fit to the simulation samples as shown in Figure 4.9), convolved with a Gaussian resolution function with the width taken from the width of the $B_s^0 \rightarrow J/\psi \pi^+ \pi^-$ signal ($18 \text{ MeV}/c^2$). Shape parameters are then fixed in the fit, as well as the yields, to the values reported in Table 4.12. In the signal sample we consider contributions from the decays $B_s^0 \rightarrow \phi (\rightarrow \pi^+ \pi^- \pi^0) \mu^+ \mu^-$, $B_s^0 \rightarrow \eta' (\rightarrow \pi^+ \pi^- \gamma) \mu^+ \mu^-$, and $B^+ \rightarrow K^+ \mu^+ \mu^-$. Their shapes are taken from simulations, as done for the corresponding background decays of the resonant samples (fixing the parameters in the fit to data), and the yields are fixed to the values estimated in Table 4.6.

decay	Argus end-point, [GeV/ c^2]	2nd Argus parameter
$B_s^0 \rightarrow J/\psi \phi (\rightarrow \pi^+ \pi^- \pi^0)$	5.24	-17.46 ± 0.75
$B_s^0 \rightarrow J/\psi \eta' (\rightarrow X (\rightarrow \pi^+ \pi^-) \gamma)$	5.37	-17.52 ± 0.12
$B^+ \rightarrow J/\psi K^+$	5.36	-10.3 ± 1.6
$B_s^0 \rightarrow \phi (\rightarrow \pi^+ \pi^- \pi^0) \mu^+ \mu^-$	5.24	-17.46 ± 0.75
$B_s^0 \rightarrow \eta' (\rightarrow X (\rightarrow \pi^+ \pi^-) \gamma) \mu^+ \mu^-$	5.37	-17.52 ± 0.12

Table 4.12 – Parameters of the partially and over- reconstructed decays PDE

4.4.3 Fit results

In Table 4.13 we report the results of the fit to the data. The fit projections on the mass distribution of each subsample are shown in Figure 4.14. In Figure 4.15 the 2011 and 2012 data sets are combined and zoomed in the region $[5.19, 5.99] \text{ GeV}/c^2$. Generally, the fit describes well the data distributions. In the resonant sample, two peaks corresponding to about 8890 $B_s^0 \rightarrow J/\psi \pi^+ \pi^-$ decays and 6400 $B^0 \rightarrow J/\psi \pi^+ \pi^-$ decays are present; in the non-resonant sample, we find 55 ± 10 (stat) ± 5 (syst) $B_s^0 \rightarrow \pi^+ \pi^- \mu^+ \mu^-$ decays and 40 ± 10 (stat) ± 3 (syst) $B^0 \rightarrow \pi^+ \pi^- \mu^+ \mu^-$ decays. The systematic uncertainty of these numbers is described in Section 4.4.4.

In Figure 4.16 we report the $\pi^+ \pi^-$ spectrum for the non-resonant and resonant sample, where the background is subtracted by using the sWeights [58] calculated with the fit to the $\pi^+ \pi^- \mu^+ \mu^-$ and $J/\psi \pi^+ \pi^-$ mass distributions; the $f_0(980)$ and $\rho(770)^0$ peaks are clearly visible. In case of the $B^0 \rightarrow J/\psi \pi^+ \pi^-$ decays, for $m_{\pi^+ \pi^-} > 1 \text{ GeV}/c^2$ the data show an excess corresponding to the resonance $f_2(1270)$, while around $500 \text{ MeV}/c^2$, the $f_0(500)$ should contribute [62]. The $\pi^+ \pi^-$ mass spectrum shape for the $B_s^0 \rightarrow J/\psi \pi^+ \pi^-$ component presents the clear $f_0(980)$ peak and the contribution from the higher mass resonances, like $f_0(1370)$ and $f_2(1270)$ [63].

Chapter 4. Search for $B \rightarrow \pi\pi\mu\mu$ decays

Parameter	2011 sample	2012 sample
\mathcal{R}_d'	$(0.387 \pm 0.093) \times 10^{-3}$	
\mathcal{R}_s'	$(0.404 \pm 0.071) \times 10^{-3}$	
$N(B_s^0 \rightarrow J/\psi \pi^+ \pi^-)$	2675 ± 59	6218 ± 92
$N(B^0 \rightarrow J/\psi \pi^+ \pi^-)$	1980 ± 67	4425 ± 100
$M(B^0)$ [GeV/ c^2]	5.28459 ± 0.00039	5.28438 ± 0.00027
M_{misid} [GeV/ c^2]	5.2036 ± 0.0027	5.2141 ± 0.0018
Signal width [MeV/ c^2]	17.96 ± 0.35	19.86 ± 0.35
N_{comb} resonant	796 ± 70	1895 ± 104
Slope comb. resonant, [c^2 /GeV]	-4.31 ± 0.37	-3.83 ± 0.19
N_{comb} non-resonant	56.2 ± 9.2	172 ± 16
Slope comb. non-resonant, [c^2 /GeV]	-1.22 ± 0.36	-1.44 ± 0.21
$N(B_c^+ \rightarrow J/\psi \pi^+ \pi^- \pi^+)$	167 ± 25	361 ± 39
$N(B^0 \rightarrow J/\psi K^*(892)^0)$	762 ± 20	1858 ± 34
$N(B^0 \rightarrow K^*(892)^0 \mu^+ \mu^-)$	7.1 ± 1.0	15.8 ± 1.5

Table 4.13 – Results of the fit to the data.

Assuming Wilks' theorem [64], we calculate the statistical significance, s_{stat} , of the $B_s^0 \rightarrow \pi^+ \pi^- \mu^+ \mu^-$ and $B^0 \rightarrow \pi^+ \pi^- \mu^+ \mu^-$ signals, measured in units of normal standard deviation, σ ,

$$s_{\text{stat}} = \sqrt{\min[-2 \log \mathcal{L}] - \min[-2 \log \mathcal{L}_0]}, \quad (4.26)$$

where $-\min[-2 \log \mathcal{L}]$ is the doubled value of the log likelihood of the fit at its maximum, and \mathcal{L}_0 corresponds to the likelihood where the signal of which we want to estimate the significance is set to zero (background-only hypothesis). The values of $\min[-2 \log \mathcal{L}]$ and $\min[-2 \log \mathcal{L}_0]$ are reported in Table 4.14. We obtain

$$s_{\text{stat}}(B_s^0 \rightarrow \pi^+ \pi^- \mu^+ \mu^-) = 7.5\sigma, \quad (4.27)$$

$$s_{\text{stat}}(B^0 \rightarrow \pi^+ \pi^- \mu^+ \mu^-) = 4.9\sigma. \quad (4.28)$$

From these numbers we expect an observation of both decays. However, to assign the global significance of the two peaks, we need to include the systematic uncertainties related to the fit, as discussed in Section 4.4.4.

$\min[-2 \log \mathcal{L}]$	$\min[-2 \log \mathcal{L}_0]$ no B_s^0 signal	$\min[-2 \log \mathcal{L}_0]$ no B^0 signal
-371790	-371733	-371766

Table 4.14 – Values of $\min[-2 \log \mathcal{L}]$ and $\min[-2 \log \mathcal{L}_0]$.

In Figure 4.17 we report the profile-likelihood, $-\Delta \log \mathcal{L}$, as a function of \mathcal{R}_s and \mathcal{R}_d , where, for each point probed, all other parameters are floating during the maximisation of the likelihood. The profile have asymmetric and tilted parabolic shapes, as can be expected in case of small

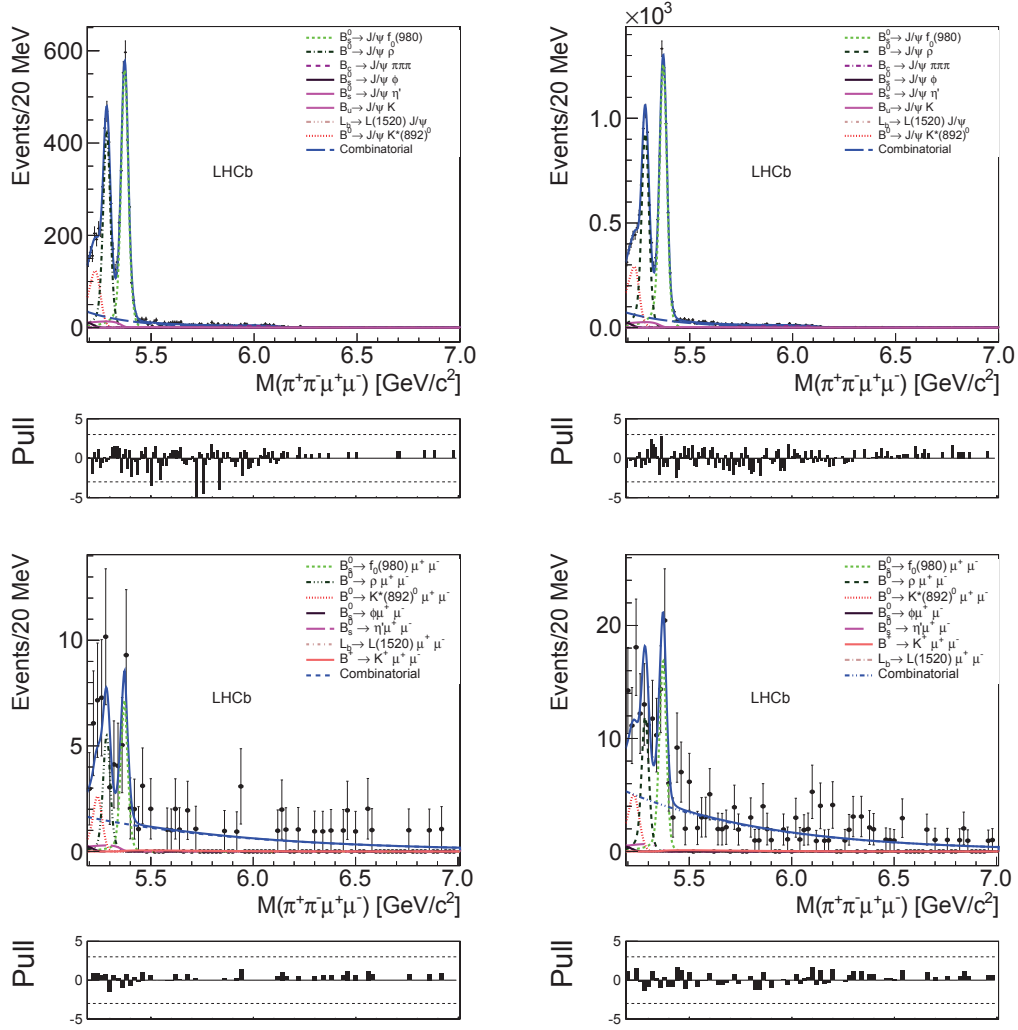


Figure 4.14 – Mass distributions of the $J/\psi\pi^+\pi^-$ and $\pi^+\pi^-\mu^+\mu^-$ sample with fit projections overlaid. Left and right columns are respectively the 2011 and 2012 data sets.

signals. Indeed, the errors on \mathcal{R}_s' and \mathcal{R}_d' are not asymmetric, as reported in Table 4.15, where we compare errors as evaluated by the MIGRAD and the MINOS algorithms of MINUIT [65], *i.e.* assuming a symmetric or an asymmetric likelihood around the minimum, respectively. Since the asymmetry is small compared to the value of the errors, we retain the uncertainties as computed by MIGRAD. The significance of the results can be seen also in Figure 4.17 from the intercept of the profile with the axis $\mathcal{R}^i = 0$, which is $\Delta\log\mathcal{L} \approx 28$ and $\Delta\log\mathcal{L} \approx 12$ for $B_s^0 \rightarrow \pi^+\pi^-\mu^+\mu^-$ and $B^0 \rightarrow \pi^+\pi^-\mu^+\mu^-$ decays, respectively; both values are sufficiently larger for the observation of the two signals.⁴ We also report the 2-dimensional profile-likelihood in the $[\mathcal{R}_s, \mathcal{R}_d]$ space in Figure 4.18, drawing contours levels of $-\Delta\log\mathcal{L}$ corresponding to regions of 68.2%, 95.5%, 99.7% C.L. ($n = 1, \dots, 5\sigma$ region for a 2-dimensional χ^2); we can also note that there is no significant correlation between the two signals.

⁴The $-\Delta\log\mathcal{L}$ corresponding to 5σ is 12.5.

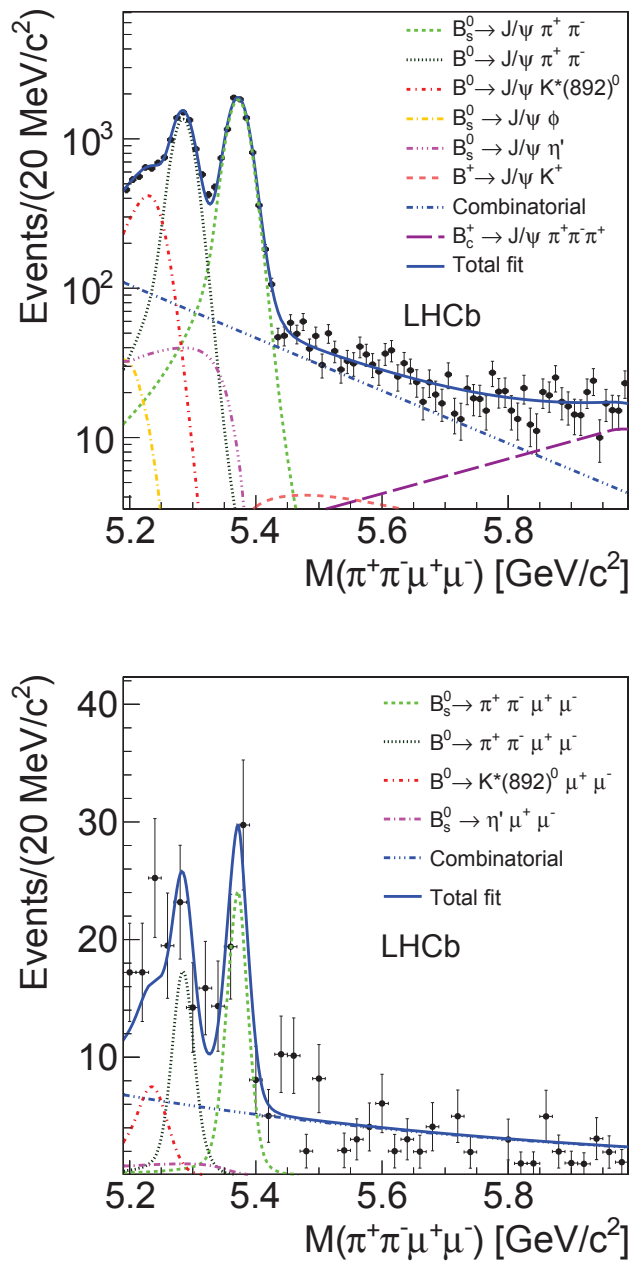


Figure 4.15 – Mass distributions of the $J/\psi \pi^+ \pi^-$ (top) and $\pi^+ \pi^- \mu^+ \mu^-$ (bottom) sample with fit projections overlaid, combining 2011 and 2012 data sets, zoomed in the region [5.19, 5.99] GeV/c².

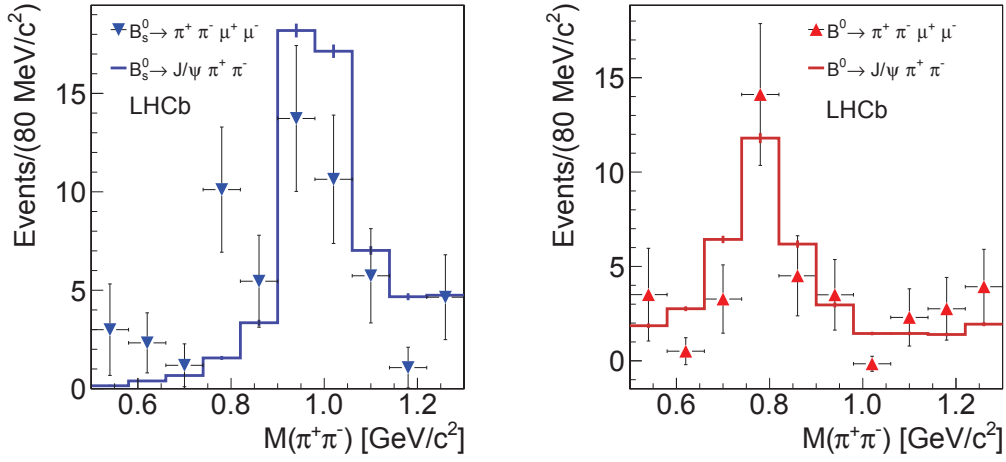


Figure 4.16 – Dipion mass distributions of the $J/\psi\pi^+\pi^-$ and $\pi^+\pi^-\mu^+\mu^-$ samples. Left and right plots are respectively resonant and non-resonant data sets.

Parameter	MIGRAD error ($\times 10^{-3}$)	MINOS error ($\times 10^{-3}$)
\mathcal{R}_s'	± 0.071	$[-0.069, +0.073]$
\mathcal{R}_d'	± 0.093	$[-0.090, +0.097]$

Table 4.15 – Comparison of MIGRAD and MINOS errors for \mathcal{R}_s' and \mathcal{R}_d' .

4.4.4 Systematic uncertainties

Several systematic uncertainties on \mathcal{R}_s and \mathcal{R}_d are considered. All of them are summarised in Table 4.16, and a description of each contribution is provided in the following. The final systematic uncertainty is the sum in quadrature of all contributions in Table 4.16. The dominant contributions is given by the uncertainty on f_s/f_d in case of \mathcal{R}_s ; the other biggest uncertainty, which is the dominant one for \mathcal{R}_d , is given by the systematic errors of the signal efficiencies and on the yields of the normalisation decays. The overall systematic uncertainties are limited, and total 43% (26%) of the statistical errors for \mathcal{R}_s (\mathcal{R}_d). Here the list of the considered systematic sources:

Shapes of the $B^0 \rightarrow K^*(892)^0\mu^+\mu^-$ background: we consider the uncertainty given by the shape parameters fixed in the fit to describe these contributions.⁵ The systematic uncertainties are estimated by the following procedure: we generate a set of values by sampling the parameters within a multidimensional Gaussian function defined by the

⁵The yields are Gaussian constrained in the fit, according to equation 4.12, therefore the associated systematic are already comprised in the statistical uncertainties of \mathcal{R}_s and \mathcal{R}_d .

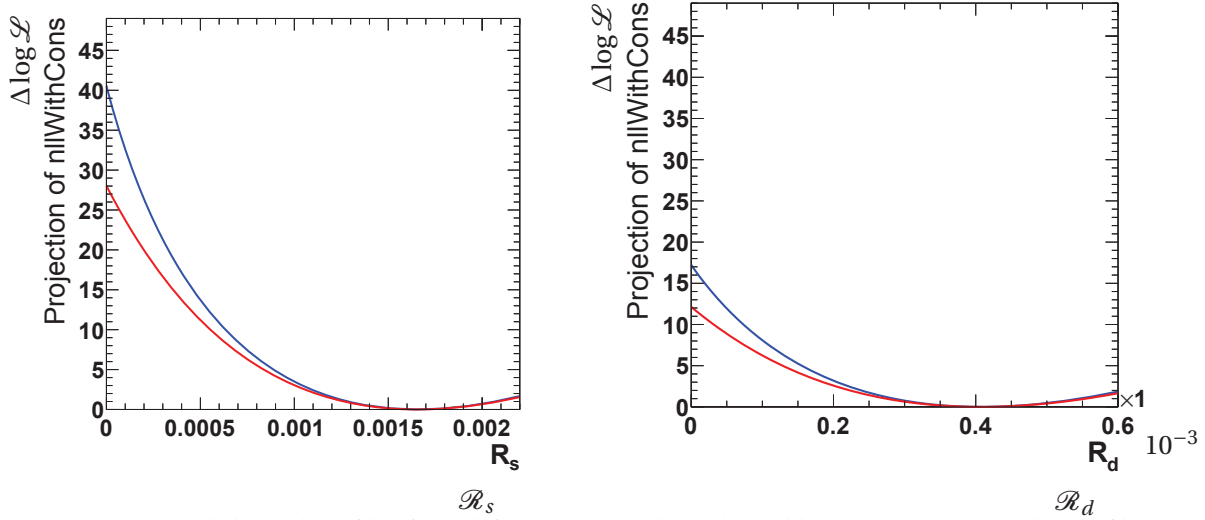


Figure 4.17 – Likelihood profile of \mathcal{R}_s (left) and \mathcal{R}_d (right). The red line corresponds to the profile-likelihood, where, for each point probed in \mathcal{R}_i , all other parameters are floating; the blue line corresponds to the likelihood scan along to \mathcal{R}_i , where all the others parameters are fixed to their values at the minimum of the likelihood.

covariance matrix of the fits to the emulated $\pi\pi\mu\mu$ mass distribution; we fix the such parameters and perform the fit to the data; we repeat 1000 times the sampling and the fit, and we plot the distribution of the difference between the fitted \mathcal{R}_s (\mathcal{R}_d) and its value from the default fit. We consider as a systematic uncertainty the r.m.s. spread of this distribution.

Partially- and over-reconstructed background: we consider the uncertainty related to the yields of these backgrounds that are fixed in the fit, and the uncertainty given by the shape parameters fixed in the fit to described these contributions. For both cases, we apply the procedure adopted for the systematic related to the $B^0 \rightarrow J/\psi K^* (892)^0$ background.

Signal shapes: we estimate the effect of having fixed the parameters of the signal PDFs in the fit to the data, by applying the same procedure described for the $B^0 \rightarrow J/\psi K^* (892)^0$ shape parameters above, and by considering the covariance matrices from the fits of the simulated samples.

Signal efficiencies: we estimate the effect of having fixed the values of the signal efficiencies in the fit. We generate a set of values by simultaneously sampling the efficiencies within Gaussian functions with widths as large as the sum in quadrature of their statistical and systematic errors (see Section 4.2.7). We fix the efficiency and we perform the fit to the data; we repeat 1000 time the sampling and the fit, and we plot the distribution of the difference between the fitted \mathcal{R}_s (\mathcal{R}_d) and its value from the default fit. We consider as a systematic uncertainty the RMS of this distribution. In this case, the largest contribution comes from the systematic uncertainties due to the limited information of the decay

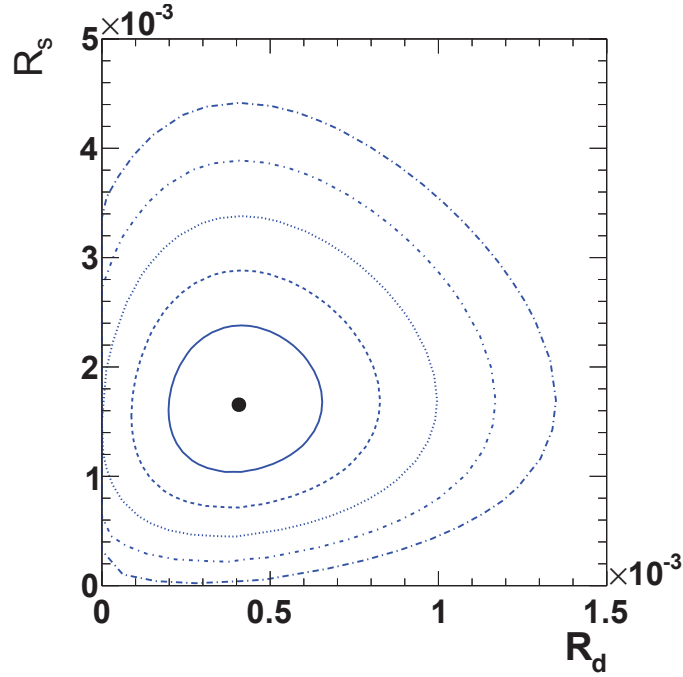


Figure 4.18 – Likelihood profile in the $[\mathcal{R}_s, \mathcal{R}_d]$ plane, showed as contours levels corresponding to regions of 68.2%, 95.5%, 99.7% C.L. ($n = 1, \dots, 5\sigma$ region for a 2-dimensional χ^2).

models for the MC generation of the $B_{(s)}^0 \rightarrow \pi^+ \pi^- \mu^+ \mu^-$ samples (“Model dependence of efficiencies” in Section 4.2.7).

Number of $B^0 \rightarrow J/\psi K^*(892)^0$ events: we generate a set of values by simultaneously sampling the number of $B^0 \rightarrow J/\psi K^*(892)^0$ events entering in the equation 4.18 with gaussian function with widths fixed from errors on the yields from the $B^0 \rightarrow J/\psi K^*(892)^0$ fit in Section 4.4.1 (we consider here the sum in quadrature of the statistical and systematic error). We fix such yields and we perform the fit to the data; we repeat 1000 time the sampling and the fit, and study the distribution of the difference between the fitted \mathcal{R}_s (\mathcal{R}_d) and its value from the default fit. We consider as a systematic uncertainty the RMS of this distribution.

Combinatorial background: A systematic uncertainty is assigned on the estimation of the combinatorial background with the following method; pseudo-experiments are generated in an extended mass range from $4.97 \text{ GeV}/c^2$, where an additional peaking component is also added to simulate the partially reconstructed B^0 decays, and the pseudo-data are fitted in the nominal range from $5.19 \text{ GeV}/c^2$. The shifts between the average fitted values and the input values of \mathcal{R}_s and \mathcal{R}_d are taken as the systematic uncertainties.

S-wave in $B^0 \rightarrow J/\psi K^*(892)^0$ yields: we evaluate the error due to the uncertainty of the S-wave subtraction to $B^0 \rightarrow J/\psi K^*(892)^0$ yields with standard error propagation on \mathcal{R}_s and \mathcal{R}_d .

Value of f_s/f_d : we evaluate the error due to the uncertainty of f_s/f_d to \mathcal{R}_s with the standard error propagation.

Source	$\sigma(\mathcal{R}_s) [10^{-3}]$	$\sigma(\mathcal{R}_d) [10^{-3}]$
Shape of misidentified decays	0.003	0.004
Partially reconstructed decays	0.003	0.004
Combinatorial background	0.029	0.014
Signal shapes	0.020	0.014
Efficiencies	0.061	0.013
Normalisation decay yields	0.055	0.014
f_s/f_d	0.093	–
Quadratic sum	0.130	0.028

Table 4.16 – Summary of systematic uncertainties on \mathcal{R}_s and \mathcal{R}_d .

4.5 Fit model validation

In order to prove stability of the fit results and validate the fit model, the fit was performed under three alternative configurations:

Extended low mass limit We repeat the fit extending the low mass region down to 4.7 GeV. In this fit, an additional component is added in the PDF to describe the background from B^0 decays with a missing pion in the reconstruction. This partially reconstructed background is modeled with an Argus function with end-point fixed to the difference of the B^0 and pion mass, and convolved with a Gaussian function representing the mass resolution.

Fixed combinatorial contribution We change the default fit by fixing the exponential function and the yields of the combinatorial background, from a previous fit to events in the right side-band region [5.8, 7.0] GeV, both in the case of the default fit range and in the case of the fit extended in the low mass region.

Linear combinatorial contribution We try a different parametrisation of the combinatorial background, by replacing the exponential function with a linear function.

The results of those tests are reported in the Table 4.17 and fit projections shown in Figure 4.19; no significant changes in the results of \mathcal{R}_s and \mathcal{R}_d are observed.

We also consider the fit of the 2011 and 2012 data separately; we report the results in Table 4.18. All the measured parameters are in agreement across sub-samples.

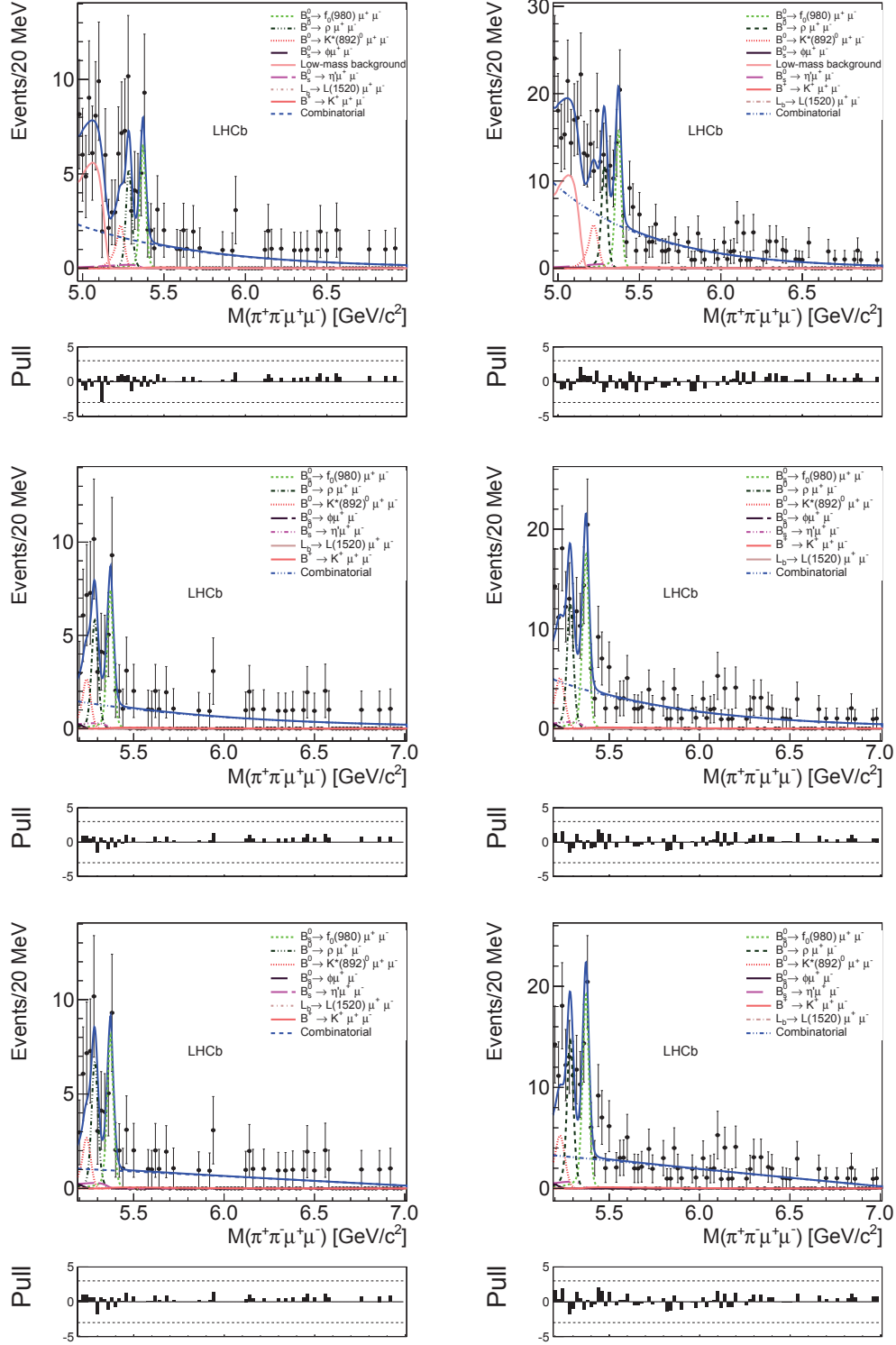


Figure 4.19 – Mass distributions of the $J/\psi\pi^+\pi^-$ and $\pi^+\pi^-\mu^+\mu^-$ sample with fit projections overlaid, for: top row, extending the low mass region; middle row: fixing the exponential function from a fit the side band data; bottom, using a linear function for the combinatorial background. Left and right columns are respectively the 2011 and 2012 data sets.

Chapter 4. Search for $B \rightarrow \pi\pi\mu\mu$ decays

	Default fit	Extended fit range	Fixing combinatorial	Linear combinatorial
$\mathcal{R}_s (\times 10^{-3})$	1.67 ± 0.29	1.59 ± 0.29	1.72 ± 0.28	1.87 ± 0.29
$\mathcal{R}_d (\times 10^{-3})$	0.413 ± 0.1	0.42 ± 0.1	0.436 ± 0.094	0.502 ± 0.098

Table 4.17 – Values of \mathcal{R}_s and \mathcal{R}_d from the fit to data in different configurations to check the stability of the results.

	2011	2012
\mathcal{R}_d'	0.52 ± 0.17	0.31 ± 0.11
W.A.	0.374 ± 0.093	
default	0.387 ± 0.093	
\mathcal{R}_s'	0.42 ± 0.13	0.395 ± 0.085
W.A.	0.407 ± 0.074	
default	0.404 ± 0.071	

Table 4.18 – Values of \mathcal{R}_s' and \mathcal{R}_d' from the fit to 2011 and 2012 data separately. The measured values are in agreement in the two sub-samples. The row "W.A." reports the weighted mean of the 2011 and 2012 results; the row "default" reports the result of the simultaneous fit to the two sub-samples. All numbers are in units of 10^{-3} .

4.6 Pseudo-experiment studies

We generate a large set of pseudo-experiments with same sample size of the data, from the PDF used to fit the data; we fit each pseudo-experiment in the same way we do for real data. We then look at the distributions of the fitted parameters, of their fitted errors, and of the pull defined as

$$p = \frac{\xi_{\text{fit}} - \xi_{\text{gen}}}{\sigma_\xi}, \quad (4.29)$$

where ξ_{fit} and σ_ξ are the fitted value in the pseudo-experiment of the parameter ξ and its error, respectively; ξ_{gen} is the value of the parameter in the generation of the pseudo-experiments.

We generate 5000 pseudo-experiments with parameters' values similar to the ones found in the fit to data. In Table 4.19 we report the results of this study; in Figure C.1 we report the distributions of the fitted errors on \mathcal{R}_i and of the pull. The errors on \mathcal{R}_i from the fit to data ($\sigma(\mathcal{R}_s) = 0.0020$ and $\sigma(\mathcal{R}_d) = 0.0067$) are in agreement with the average fitted error in the pseudo-experiments.

The study shows unbiased estimates of the parameters (within $\leq 9\%$ of the statistical errors for \mathcal{R}_s , and $\leq 3\%$ of the statistical errors for \mathcal{R}_d), and normal distributions for the pulls. For each pseudo-experiment, we calculate the significances of the signals by using equation 4.26 and we plot their distributions (see Appendix C); according to these pseudo-experiments, we should expect a significance of 7.5σ and 5.4σ for the $B_s^0 \rightarrow \pi^+\pi^-\mu^+\mu^-$ and $B^0 \rightarrow \pi^+\pi^-\mu^+\mu^-$

signals, respectively. The significance found in data for $B^0 \rightarrow \pi^+ \pi^- \mu^+ \mu^-$ signals is smaller, but still in the core of the expected distribution.

Parameter	Gen. value	Mean fit value	Mean fit error	Pull mean	Pull RMS	s_{stat}
\mathcal{R}_s	1.132	1.126	0.196	-0.076 ± 0.012	0.98	7.5
\mathcal{R}_d	0.292	0.294	0.065	-0.019 ± 0.012	0.98	5.4
\mathcal{R}_s	0.0	-0.009	0.099	-0.227 ± 0.014	1.14	0.7
\mathcal{R}_d	0.292	0.284	0.064	-0.173 ± 0.012	1.00	5.3
\mathcal{R}_s	1.132	1.118	0.195	-0.118 ± 0.012	0.97	7.5
\mathcal{R}_d	0.0	-0.011	0.041	-0.377 ± 0.014	1.15	0.8

Table 4.19 – Results of the pseudo-experiments. The second column report the values used in the generation of the pseudo-experiments for \mathcal{R}_s and \mathcal{R}_d ; all other parameters are generated with values close to the ones found in the fit to data, see the table. 4.13.

We generate a set of 17 000 pseudo-experiments where the $B_s^0 \rightarrow \pi^+ \pi^- \mu^+ \mu^-$ signal is set to zero, while the $B^0 \rightarrow \pi^+ \pi^- \mu^+ \mu^-$ yield is fixed to the value obtained from the fit to data. The estimated \mathcal{R}_s is biased ($\approx 23\%$ of the statistical errors), probably due to the asymmetry of the fitted uncertainties visible in the likelihood profile, which become more evident in the limit of zero signal events. Also in this case we plot the distributions of significances: in case of no signal, the expected $B_s^0 \rightarrow \pi^+ \pi^- \mu^+ \mu^-$ significance is around 0.7σ , while the expected significance of the nonzero $B^0 \rightarrow \pi^+ \pi^- \mu^+ \mu^-$ signal is around 5.3σ . We repeat the same test with a set of 17 000 pseudo-experiments, where the $B^0 \rightarrow \pi^+ \pi^- \mu^+ \mu^-$ signal is set to zero, while the $B_s^0 \rightarrow \pi^+ \pi^- \mu^+ \mu^-$ yield takes the value as found in data; again, the fit presents a small bias in the estimate of \mathcal{R}_d . Results of these tests are summarised in Table 4.19 and corresponding distributions are presented in Appendix C.

4.7 Results

The first observation of the decay $B_s^0 \rightarrow \pi^+ \pi^- \mu^+ \mu^-$ and the first evidence of B^0 decay to the same final state are obtained in a data set corresponding to an integrated luminosity of 3.0 fb^{-1} collected by the LHCb detector in pp collisions at center-of-mass energies of 7 and 8 TeV. The analysis is restricted to candidates with muon pairs that do not originate from ϕ , J/ψ , and $\psi(2S)$ resonances, while the pion pairs are required to have invariant mass in the range $0.5\text{--}1.3 \text{ GeV}/c^2$. About 55 $B_s^0 \rightarrow \pi^+ \pi^- \mu^+ \mu^-$ decays and 40 $B^0 \rightarrow \pi^+ \pi^- \mu^+ \mu^-$ decays are observed with significances of 7.2σ and 4.8σ , respectively. Their branching fractions relative to the branching fraction of the $B^0 \rightarrow J/\psi (\rightarrow \mu^+ \mu^-) K^* (892)^0 (\rightarrow K^+ \pi^-)$ decay are measured to be

$$\frac{\mathcal{B}(B_s^0 \rightarrow \pi^+ \pi^- \mu^+ \mu^-)}{\mathcal{B}(B^0 \rightarrow J/\psi (\rightarrow \mu^+ \mu^-) K^* (892)^0 (\rightarrow K^+ \pi^-))} = (1.67 \pm 0.29 \text{ (stat)} \pm 0.13 \text{ (syst)}) \times 10^{-3},$$

$$\frac{\mathcal{B}(B^0 \rightarrow \pi^+ \pi^- \mu^+ \mu^-)}{\mathcal{B}(B^0 \rightarrow J/\psi (\rightarrow \mu^+ \mu^-) K^* (892)^0 (\rightarrow K^+ \pi^-))} = (0.41 \pm 0.10 \text{ (stat)} \pm 0.03 \text{ (syst)}) \times 10^{-3}.$$

Chapter 4. Search for $B \rightarrow \pi\pi\mu\mu$ decays

From these ratios, the following branching fractions are obtained:

$$\mathcal{B}(B_s^0 \rightarrow \pi^+ \pi^- \mu^+ \mu^-) = (8.6 \pm 1.5 \text{ (stat)} \pm 0.7 \text{ (syst)} \pm 0.7 \text{ (norm)}) \times 10^{-8} \text{ and}$$

$$\mathcal{B}(B^0 \rightarrow \pi^+ \pi^- \mu^+ \mu^-) = (2.11 \pm 0.51 \text{ (stat)} \pm 0.15 \text{ (syst)} \pm 0.16 \text{ (norm)}) \times 10^{-8},$$

where the third uncertainties are due to the uncertainties on the branching fraction of the normalisation decay. We use $\mathcal{B}(B^0 \rightarrow J/\psi K^*(892)^0) = (1.30 \pm 0.10) \times 10^{-3}$, which is the weighted average of measurements where the $K^+ \pi^-$ S-wave contribution is subtracted [66, 67, 68], $\mathcal{B}(J/\psi \rightarrow \mu^+ \mu^-)$ from Ref. [69], and $\mathcal{B}(K^*(892)^0 \rightarrow K^+ \pi^-) = 2/3$.

Assuming that the decays $f_0(980) \rightarrow \pi^+ \pi^-$ and $\rho(770) \rightarrow \pi^+ \pi^-$ are the dominant transitions in the $B_s^0 \rightarrow \pi^+ \pi^- \mu^+ \mu^-$ and $B^0 \rightarrow \pi^+ \pi^- \mu^+ \mu^-$ decays, respectively, and neglecting other contributions, the $B_{(s)}^0 \rightarrow \pi^+ \pi^- \mu^+ \mu^-$ branching fractions are corrected to account for the selection efficiencies of the $f_0(980)$ and $\rho(770)$ resonances in the $\pi^+ \pi^-$ mass range considered. The following values are obtained: $\mathcal{B}(B_s^0 \rightarrow f_0(980)(\rightarrow \pi^+ \pi^-) \mu^+ \mu^-) = (8.9 \pm 1.8) \times 10^{-8}$ and $\mathcal{B}(B^0 \rightarrow \rho(770) \mu^+ \mu^-) = (2.24 \pm 0.60) \times 10^{-8}$, where all uncertainties are summed in quadrature. These values favor SM expectations of Refs. [33, 37, 38] and disfavor the $\mathcal{B}(B_s^0 \rightarrow f_0(980) \mu^+ \mu^-)$ SM expectation of Ref. [34], as shown in Figure 4.20.

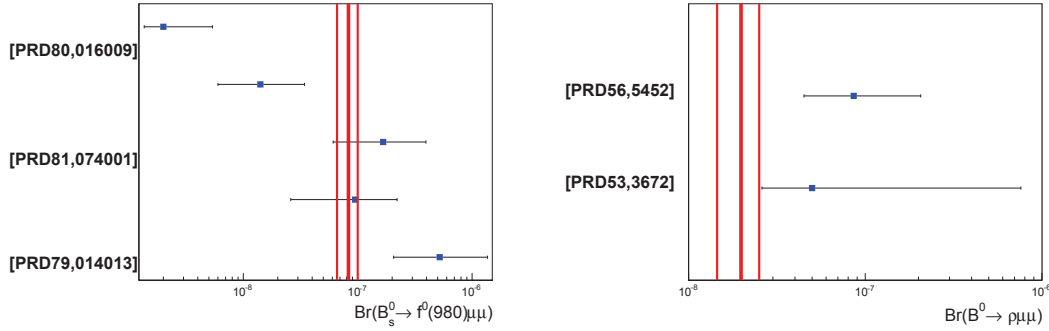


Figure 4.20 – Comparison of SM theoretical expectations obtained with various phenomenological techniques (points with errors) with our measurement (red line).

5 Measurement of the J/ψ production cross-section

5.1 Introduction

This chapter describes the study of the production mechanism of the J/ψ meson, the lightest charmonium state, in pp collisions at $\sqrt{s} = 13$ TeV recorded by the LHCb detector in summer 2015.

In section 2.2 we briefly discuss the perturbative and non-perturbative regimes of QCD. Experimental studies of the production cross-section of heavy quarkonia (flavourless particles consisting of the quark-antiquark pair) provide the opportunity to test QCD predictions for both regimes simultaneously. Since the very first theoretical attempts to describe the production of the heavy quarkonium, the calculation of the production cross-section includes both non-perturbative terms, which depend on the intrinsic QCD scale, and perturbative terms, which depend on external scales, such as the momentum p_T of the quarkonium [70].

The color-singlet model (CSM) [71, 72, 73, 74, 75, 76, 77] is one of such attempts. In this model, the quarkonium production is described in two steps. At the first step, a pair of the heavy on-shell quarks ($Q\bar{Q}$) is produced. The energy scale of this process depends on the mass of the charmonium and the transverse momentum as $M^2 + p_T^2$ [78], which allows perturbative calculation. The second step is the hadronisation of this pair into the specific charmonium state. The CSM description considers only bound states of heavy quarks, assuming that the quarks are at rest in the meson frame. The second assumption of the CSM is that the $Q\bar{Q}$ pair has the same color and spin number as the final meson, *i.e.* the pair is produced in a color-singlet state.

The predictions of the CSM are in a good agreement with data at low energy. However, extrapolations to the higher energies are complicated. Corrections to the CSM at the next-to-leading order (NLO) and next-to-next-to-leading order (NNLO) in α_s appeared to be very large, which questions the assumption of the convergence of the α_s expansion. Moreover, the CSM is theoretically inconsistent for the calculations of the production and decay of quarkonium states with non-zero orbital angular momentum since it leads to uncanceled infrared di-

vergences [79].

Non-relativistic QCD (NRQCD) approach [80, 81, 82] allows to overcome the limitation of the CSM. In NRQCD, the production cross-section of a quarkonium H in hard collisions of the partons is written as:

$$\sigma(H) = \sum_n \sigma_n(\Lambda) \langle \mathcal{O}_n^H(\Lambda) \rangle \quad (5.1)$$

where the summation is performed over the states of the $Q\bar{Q}$ pair; Λ is the ultraviolet cutoff of the effective theory; $\sigma_n(\Lambda)$ are expansions in powers of heavy-quark velocity [80] of the cross sections to produce a $Q\bar{Q}$ pair in the color, spin, and orbital-angular momentum state n ; and $\langle \mathcal{O}_n^H(\Lambda) \rangle$ is the long-distance matrix element (LDME) representing the probability of the $Q\bar{Q}$ pair in the specific quantum state to hadronise into the charmonium meson. One may obtain CSM from NRQCD by counting only color-singlet contributions of leading order of velocity for each quarkonium state. The main advantage of NRQCD, is the universality of the LDMEs. Thus, the NRQCD predictions given in this analysis are based on the matrix elements measured at Tevatron [83].

The charmonium state J/ψ can be produced directly in hard collisions of partons or through feed-down of excited quarkonium states or it could be decay product of the b -hadron. The former are referred to as “prompt J/ψ ”; the latter as “ J/ψ -from- b ”. The production cross-section of the J/ψ -from- b and its dependence on p_T of the J/ψ meson are described with the Fixed Order plus Next-to-Leading Logarithms (FONLL) calculations [8].

Both NRQCD and FONLL predictions suffer from similar systematic uncertainties, such as the value of the quark mass, factorisation scale dependence and the choice of the parton distribution function (p.d.f.). Moreover, NRQCD calculations have additional source of systematical uncertainty from LDMEs. Being combined, these uncertainties are rather large (see Figure 5.1, left), however they significantly cancel in predictions of ratio of production cross-sections at different energies (see Figure 5.1, right), which provide rich opportunities for experimental tests of QCD predictions with an unprecedented precision.

The J/ψ differential production cross-section has been measured by LHCb at the center-of-mass energies of 2.76 TeV [84, 85], 7 TeV [86, 87, 88, 89, 90], and 8 TeV [91]. Predictions of the production cross-section of the J/ψ -from- b and its dependence on the p_T made with the FONLL are in agreement with measurements [92]. The measurements for the production cross-section of the prompt J/ψ and its dependence on the p_T are well described by the NRQCD calculations for both LHC [93, 94, 95] and Tevatron [96, 97] experiments. However, the NRQCD factorisation approach predicts large transverse polarisation of J/ψ at high p_T [98, 99, 100, 101], which is not supported by experimental results [102, 103, 104, 105, 106, 107, 108].

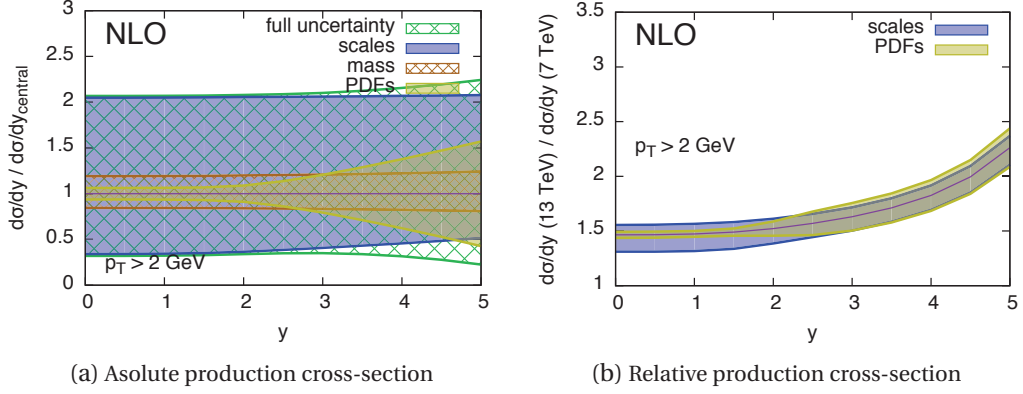


Figure 5.1 – FONLL predictions of the charm quark rapidity distribution at $\sqrt{s} = 13\text{TeV}$ normalised to the central theoretical prediction (a), and ratio of the charm quark rapidity distribution in pp collisions at $\sqrt{s} = 13\text{TeV}$ and $\sqrt{s} = 7\text{TeV}$ at LHC (b) [7] .

5.2 Cross-section determination

The main quantity measured in this analysis is the double differential production cross-section of the prompt J/ψ and the J/ψ -from- b determined for kinematic region of $2.0 < y < 4.5$ and $0\text{GeV}/c < p_T < 14\text{GeV}/c$. The cross-section is defined as

$$\frac{d^2\sigma^i}{dydp_T} = \frac{N(J/\psi \rightarrow \mu^+\mu^-)^i}{\mathcal{L} \times \varepsilon_{\text{tot}}^i \times \mathcal{B}(J/\psi \rightarrow \mu^+\mu^-) \times \Delta y \times \Delta p_T} \quad (5.2)$$

where i stands for the (p_T, y) bin number and

- $N(J/\psi \rightarrow \mu^+\mu^-)$ is either the number of prompt J/ψ or J/ψ -from- b signals reconstructed through the dimuon decay channel; it is obtained by the fit described in Section 5.2.1;
- \mathcal{L} is the integrated luminosity equal to $3.05 \pm 0.12\text{pb}^{-1}$;
- ε_{tot} is the total efficiency, described in detail in Section 5.2.2;
- $\mathcal{B}(J/\psi \rightarrow \mu^+\mu^-) = (5.961 \pm 0.033)\%$ is the branching fraction of the decay $J/\psi \rightarrow \mu^+\mu^-$, obtained from the Ref. [69];
- $\Delta p_T = 1\text{GeV}/c$ is the bin width of the J/ψ transverse momentum;
- $\Delta y = 0.5$ is the bin width of the J/ψ rapidity.

The cross-section is also integrated over one and both of p_T and y variables to compare with theoretical predictions and previous measurements. To provide precise tests of the QCD predictions, ratio ($R_{13/8}$) of the production cross-sections obtained at the energies of the proton-proton collisions of 13 TeV and 8 TeV is also determined for every kinematic bin.

5.2.1 Selection of the J/ψ candidates

Decay candidates used in this analysis are selected with the trigger system and passed through the set of the offline selection criteria. Hardware selection is performed by the `L0Muon` line, which selects events with at least one muon with high transverse momentum $p_T > 900 \text{ MeV}/c$. The first level of the software trigger uses `Hlt1DiMuonHighMass` line to select events with a pair of well-reconstructed muons which form heavy particle. The full list of selection criteria for the Hlt1 selection is shown in Table 5.1. Decay candidates are formed from the two opposite sign muons and undergo the further selection at the second level of the software trigger according to the `Hlt2DiMuonJPsiPVRfitTurbo` line. The selection requirements for this line can be found in Table 5.2.

Variable	Value
Track χ^2/ndf	< 3
Track p	$> 3000 \text{ MeV}/c$
Track p_T	$> 500 \text{ MeV}/c$
Vertex DOCA	< 0.2
Vertex χ^2	< 25
Muon Identification	<code>isMuon</code>
$M(\mu^+\mu^-)$	$> 2700 \text{ MeV}/c^2$

Table 5.1 – `Hlt1DiMuonHighMass` selection criteria

Variable	Value
Track χ^2/ndf	< 4
Muon Identification	<code>isMuon</code>
Vertex χ^2/ndf	< 25
Mass cut	$ m - M(J/\psi) < 150 \text{ MeV}$

Table 5.2 – `Hlt2DiMuonJPsiTurbo` selection criteria

Events containing the decay candidates selected with the `Hlt2DiMuonJPsiPVRfitTurbo` line pass additional offline selection, which consist from the several requirements:

- Event should have at least one reconstructed primary vertex (PV) within the luminous region. If event has several PVs, J/ψ candidate is associated to the PV with the smallest impact parameter χ^2 , *i.e.* to the primary vertex, which χ^2 increases least after the association of the tracks of the candidate to it.
- To suppress clone candidate, tracks of the candidate should satisfy requirements for Kullback-Leibler (KL) distance [109, 110, 111] and have low track fit χ^2/ndf .
- Tracks of the candidate should be identified as muons.

- Secondary (*i.e.* formed by the two candidate tracks) vertex should be fitted with low χ^2 and be close to the primary vertex.

Distance between the two vertices is defined through the pseudo-proper time, t_z :

$$t_z = \frac{(z_{J/\psi} - z_{PV}) \times M_{J/\psi}}{p_z}, \quad (5.3)$$

Where $z_{J/\psi}$ is the z -coordinate of the vertex of the J/ψ candidate, z_{PV} is that of the primary vertex, p_z is the z component of the measured momentum of the J/ψ candidate, $M_{J/\psi}$ is the known J/ψ mass. This variable was chosen as the best approximation of the lifetime, which is impossible to reconstruct in absence of full decay candidate. Projection of the pseudo proper time on axis z rather than on any other direction (for example, on direction of the J/ψ momentum) is just a result of convenience within LHCb collaboration. The full list of offline selection criteria is presented in Table 5.3

Variable	Value
Number of PV	> 0
Track χ^2 /ndf	< 3
Muon Identification	isMuon, $DLL_{\mu\pi} > 0$.
Muon p_T	> 700 MeV/c
Muon p	$3 < p < 500$ GeV/c
Track ghost probability P(ghost)	< 0.3
Vertex fit probability P(χ^2 /ndf)	> 0.5%
Mass cut	$ m(\mu^+ \mu^-) - M(J/\psi) < 150$ MeV/c ²
Pseudo proper time	$ t_z < 10$ ps
Uncertainty of t_z	< 0.3 ps
KL	> 5000
luminous region	$ z_{PV} < 227$ mm, $ y_{PV} < 1$ mm

Table 5.3 – Offline selection criteria

5.2.2 Efficiency determination

The total selection efficiency is factorised as

$$\epsilon_{\text{tot}} = \epsilon_{\text{acc}} \times \epsilon_{\text{Reco\&Sel}} \times \epsilon_{\text{MuonID}} \times \epsilon_{\text{Trigger}} \quad (5.4)$$

and calculated for each kinematic bin. Here:

- ϵ_{acc} is the geometrical acceptance efficiency. This is the probability that both muons of the J/ψ candidate are within the LHCb acceptance region, which is the polar angle

Chapter 5. Measurement of the J/ψ production cross-section

[10, 400] mrad defined with respect to the direction of LHCb z -axis, before entering the magnet.

- $\epsilon_{\text{Reco\&Sel}}$ is the efficiency of the reconstruction and selection. This is the probability of the J/ψ candidate (with both muons within the LHCb acceptance) to be reconstructed and pass through the offline selection criteria. This also includes the efficiency of the track reconstruction, which is found from the simulation and corrected by a data-driven technique. Efficiency of the reconstruction and selection is calculated separately for the prompt J/ψ and for the J/ψ -from- b .
- ϵ_{MuonID} is the efficiency of the identification criteria of the muons. This efficiency is calculated separately from $\epsilon_{\text{Reco\&Sel}}$ because simulations fail to properly describe the particle identification performances. Muon identification efficiency is estimated from simulations and corrected with the data-driven technique.
- $\epsilon_{\text{Trigger}}$ is the trigger efficiency. This term describes the probability of the event (with fully reconstructed and selected J/ψ candidate) to pass through the trigger selection.

The correction factor of the muon identification efficiency is obtained from the comparison of the efficiency obtained from the simulation with that obtained from a data-driven technique, the tag-and-probe method. In this method, a J/ψ candidate is reconstructed with only one track identified as a muon (“tag”), and the muon identification efficiency is taken to be equal to the probability of the second muon to pass through the identification requirements. This measurement is performed in bins of p_μ and η_μ ; the resulting tag-and-probe efficiency is defined as

$$\epsilon_{\text{tag-and-probe}} = \frac{\sum \epsilon_{\mu^+}(p_{\mu^+}, \eta_{\mu^+}) \epsilon_{\mu^-}(p_{\mu^-}, \eta_{\mu^-})}{N_{\text{tot}}}, \quad (5.5)$$

where the sum runs over all J/ψ candidates of the simulation sample, $\epsilon_\mu(p_\mu, \eta_\mu)$ is the muon identification efficiency of a single muon, and N_{tot} is the total number of simulated J/ψ candidates. The ratio between the tag-and-probe efficiency and the one from simulations is 1.050 ± 0.017 , which is used as the correction factor to the total efficiency for every (p_T, y) bin.

The correction of the tracking efficiency is obtained similarly to that of the muon identification efficiency. Here, the tag track is a fully reconstructed and tightly selected long muon track, and the probe track is reconstructed using only the Muon stations and the TT [27]. The tag-and-probe tracking efficiency is defined as the fraction of the J/ψ candidates where the probe track can be matched to the fully reconstructed long track. A correction factor, equal to the ratio of the tag-and-probe tracking efficiencies for a single track in data and simulations, is calculated for each (p_T, y) bin of the J/ψ meson and it ranges from 0.94 to 1.04 depending on the bin.

The online reconstruction procedure does not allow to separate $\epsilon_{\text{Reco\&Sel}}$ and $\epsilon_{\text{Trigger}}$, so ef-

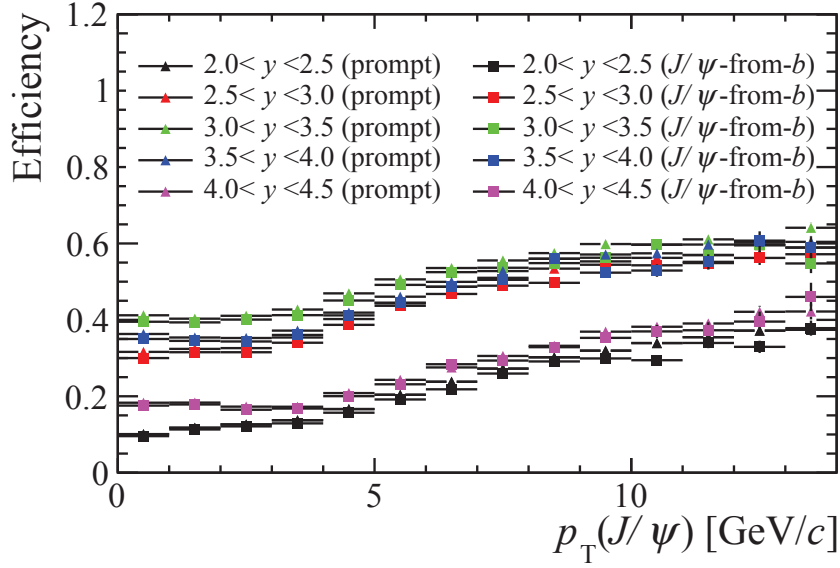


Figure 5.2 – Total efficiency ϵ_{tot} calculated using simulated events as a function of p_T in bins of y . The numbers of acceptance efficiency, muon ID efficiency and trigger efficiency for prompt J/ψ and J/ψ -from- b are taken to be the same.

Efficiency studies are performed using the simulated sample with the offline reconstruction. As discussed in Section 5.2.4, online and offline reconstructions can be considered as equal up to a $\sim 0.1\%$ difference, which can be neglected compared to other sources of uncertainty. The total efficiency for the prompt J/ψ and the J/ψ -from- b for each (p_T, y) bin is presented in Figure 5.2.

5.2.3 Fit model

The number of the prompt J/ψ and the J/ψ -from- b candidates is estimated from a simultaneous maximum likelihood fit of the unbinned distributions of the mass and t_z . The mass fit is used to separate inclusive J/ψ candidates from combinatorial background and t_z fit allows to estimate contributions from peaking backgrounds, prompt J/ψ and the J/ψ -from- b separately.

In the mass fit the J/ψ peak is described by a double Crystal Ball function [112] with a common mean value (μ) and different widths (σ_1 and σ_2). The mean value and the width of the first Crystal Ball are free parameters of the fit, the second width is parametrised as a function from the first width from simulation, and the rest of parameters are fixed from the simulation. The background distribution is described by exponential function.

The t_z distribution of prompt J/ψ mesons is described by a delta function, $\delta(t_z)$, that of J/ψ -from- b is described by an exponential function for $t_z > 0$ with free slope parameter. Both

of them are convolved with the detector resolution function f_{res} defined as:

$$f_{\text{res}}(t_z; \mu, S_1, S_2, \beta) = \frac{\beta}{\sqrt{2\pi}S_1\sigma} e^{-\frac{(t_z-\mu)^2}{2S_1^2\sigma^2}} + \frac{1-\beta}{\sqrt{2\pi}S_2\sigma} e^{-\frac{(t_z-\mu)^2}{2S_2^2\sigma^2}} \quad (5.6)$$

where σ is an error of the measured t_z value; $S_{1,2}$ are the scale parameters accounting imperfect estimation of the σ ; parameter μ defines the bias of the t_z distribution; and β is a fraction of the first Gaussian. Background contributions considered in t_z fit model are so-called ‘‘Wrong PV’’ candidates and combinatorial candidates.

Wrong PV candidates are J/ψ candidates which are associated with a wrong PV. The main source of these candidates are events with multiple primary vertices where the correct primary vertex of the candidate is not reconstructed. The shape of the t_z distribution of such candidates is obtained by the ‘‘Next Event’’ method, where the position of the associated primary vertex of the candidate is taken from the next event. Another possible source of candidates with a wrong PV are events with multiple PV, where a wrong PV happens to be close to the correct one. This component, however, is neglected during the fit since simulation studies shows that the fraction of such candidates is negligibly small.

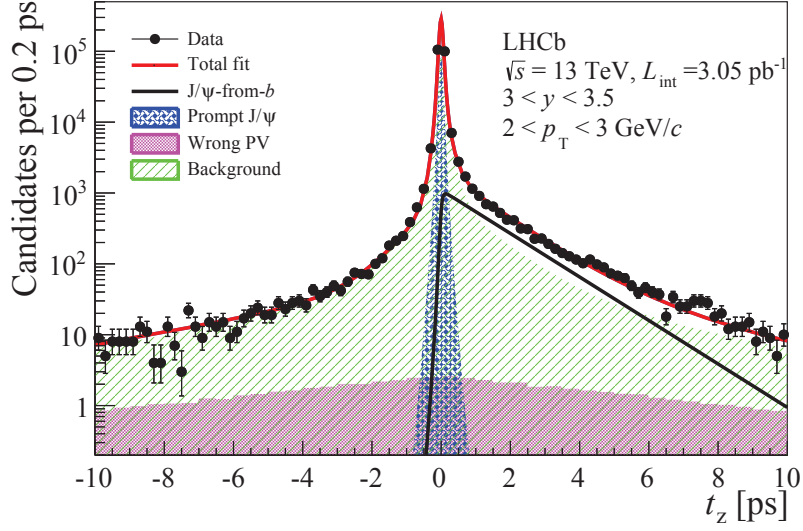
The t_z fit model of combinatorial candidates is studied from the fit of sidebands events ($60 < |M_{\mu\mu} - M_{J/\psi}| < 150 \text{ MeV}/c^2$). It is modeled with empirical function composed of a delta functions and five exponentials. This function is convolved with the background resolution function, which consists of two Gaussian functions with higher widths than the one of the signal resolution.

The fit is performed in each kinematic bin. An example of the fit is presented in Figure 5.3.

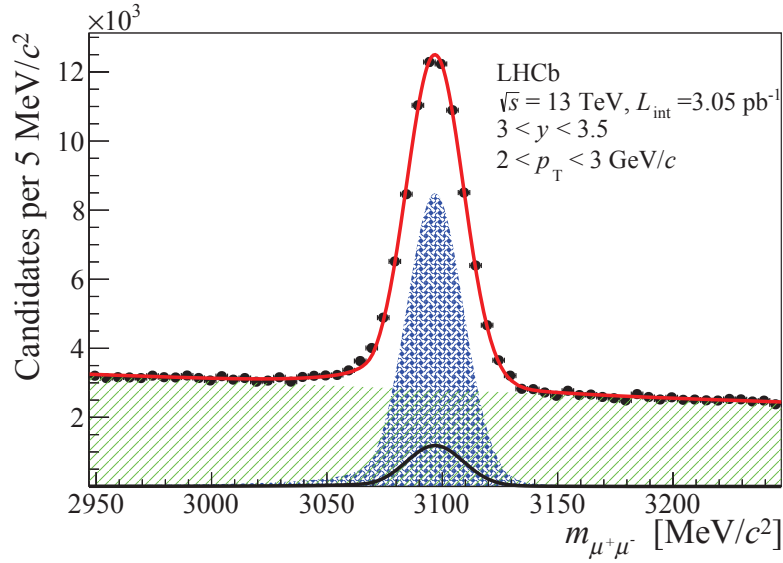
5.2.4 Validation of the novel data processing model

Measurement of the J/ψ production cross-section in early Run II data pioneers in usage of the Turbo stream technique for selection of the decay candidates. Thus, it is essential to show that this novel procedure is well understood and give performance identical to the standard (offline) reconstruction and selection sequence. The comparison of the two reconstruction sequences is performed event by event with means of the TupleToolTwoParticleMatching algorithm developed for this purpose as a part of the `Phys/DecayTreeTuple` package. For each event this algorithm looks for the offline and online candidates and match them basing of the information from the hits in the detector. The maximal fraction of the common hits is used as a quantitative measure of similarity of the candidates. After matching, the tool stores information on both original and matched candidates to the tuple, allowing to compare fraction of common hits or any other observable.

The comparison of the offline and online reconstruction sequences is performed with a simulated sample of 959006 $J/\psi \rightarrow \mu^+\mu^-$ events. These events have passed through the online



(a) Fit of the pseudo-proper time



(b) Mass fit

Figure 5.3 – Example of the fit of the mass and t_z distributions. Black points correspond to data, the prompt J/ψ contribution is shown in the shaded blue, the J/ψ -from- b contribution is shown as a black line, the wrong PV contribution is shown in shaded magenta and the combinatorial fraction is represented in shaded green.

and the offline reconstruction and selection procedures, and this created two sets of the candidates. For the online reconstruction and selection the `Hlt2DiMuonJPsiTurbo` line is used. Offline, J/ψ candidates are combined from opposite-charge muons and filtered by the selection requirements identical to the ones applied in `Hlt2DiMuonJPsiTurbo` line (see

Chapter 5. Measurement of the J/ψ production cross-section

	Online	Offline
Total generated	959006	
Total reconstructed	432111	431433
+ Trigger cuts	347392	346962
+ Offline cuts	310479	310270
+ Overlap > 70%	310478	310270
+ MC-matched	306810	306677

Table 5.4 – Numbers of offline and online (Turbostream) candidates on each step of the reconstruction and selection sequences. Overlap is taken as a fraction of common hits within the LHCb detector between the two candidates. MC-matching procedure selects decay candidates which were correctly reconstructed from the generated decay.

Table 5.2).

The comparison of the reconstruction efficiency of online and offline sequences shows they are identical up to 0.1% precision (see Table 5.4). Distributions of observables relevant for this analysis (see Figure 5.4) are also found to be independent of type of the reconstruction sequence.

Finally, it is explicitly shown that the results of this analysis do not depend on the type of the used reconstruction sequence. The mass of the J/ψ and pseudo proper time distributions of both online and offline samples are fitted with the model described in the Section 5.2.1, yielding identical parameters for the cases (see Table 5.5).

	Offline	Online
Mean value of a double Crystal Ball $\mu_{J/\psi}$, [MeV/c ²]	3097.50 ± 0.06	3097.50 ± 0.06
Width of the first Crystal Ball σ_1 , [MeV/c ²]	11.55 ± 0.05	11.55 ± 0.05
Fraction of J/ψ -from- $b F_b$	0.0982 ± 0.0016	0.0981 ± 0.0016
Bias of $t_z \mu * 1000$, [ps]	-0.6 ± 0.3	-0.6 ± 0.3
Pseudo b lifetime τ_b , [ps]	1.48 ± 0.03	1.48 ± 0.03
Resolution function parameter β	0.044 ± 0.003	0.045 ± 0.003
Resolution function parameter S_1	4.4 ± 0.2	4.4 ± 0.2
Resolution function parameter S_2	1.050 ± 0.005	1.050 ± 0.005
Background yield n_{bkg}	323 ± 44	321 ± 44
Signal yield n_{sig}	48699 ± 224	48730 ± 224

Table 5.5 – Comparison of fit results obtained from the fit of the online and offline candidates.

5.2.5 Overview of the systematic uncertainties

The systematic uncertainties considered are listed in Table 5.6 and described in the following:

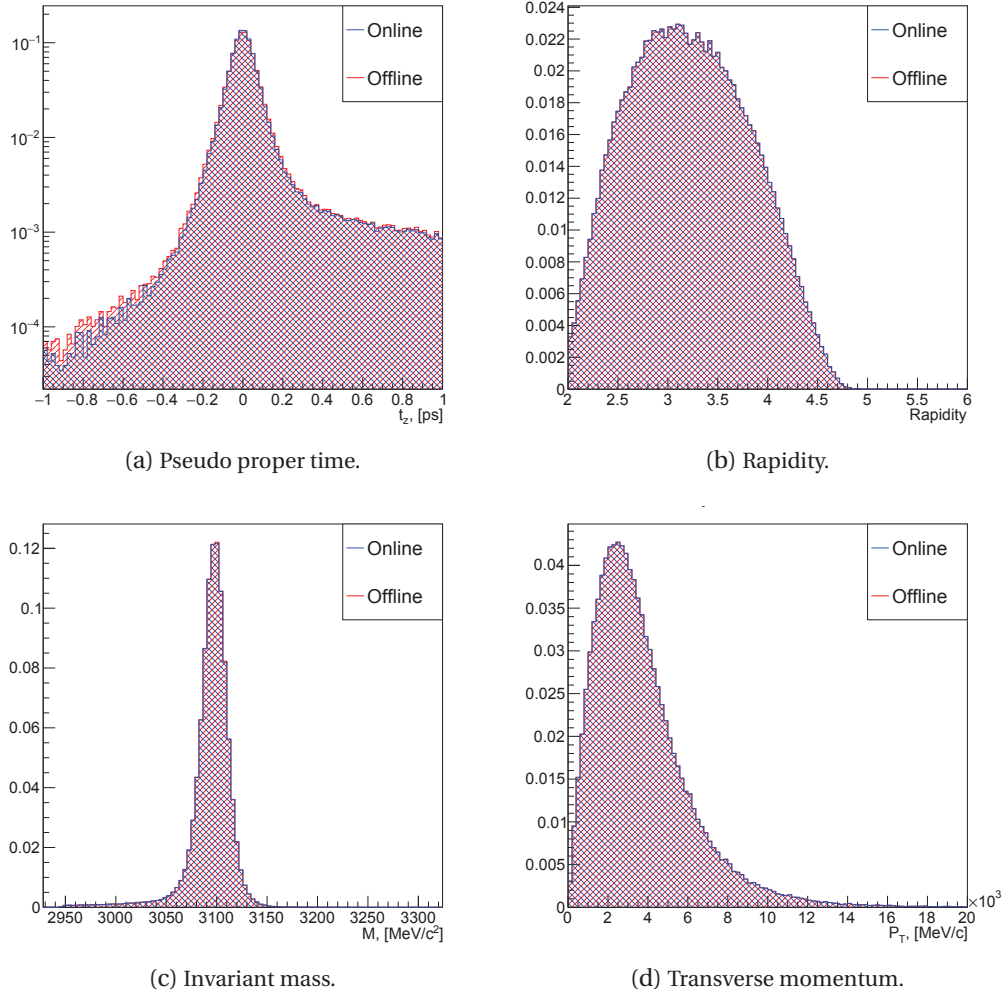


Figure 5.4 – Comparison of the kinematical distribution for the online (blue) and offline (red) reconstructed samples. Normalisation is arbitrary.

Signal shape The systematic uncertainty of the J/ψ yield caused by a possible mismodeling of the mass distribution is estimated from the difference of the yields obtained with the nominal model and an alternative one. The alternative model is an `Hypatia`. This model effectively takes into account an event-by-event variations of the mass resolution, but requires much more computing resources and thus can not be used as the nominal model. The relative difference of the yields estimated with the two models is 1%, and this value is assigned as a systematic uncertainty.

t_z fits An imperfect description of the t_z distribution can be caused by a wrong modeling of the detector resolution or by a mismodeling of the contributions of combinatorial background or “wrong PV” background.

The systematic uncertainty of the fraction of the J/ψ -from- b mesons, F_b , caused by the wrong description of the t_z distribution is estimated from the variation of the nominal

Chapter 5. Measurement of the J/ψ production cross-section

Quantity	Systematic uncertainty
Luminosity	3.9%
L0 Trigger*	0.1-5.9%
Hlt1 Trigger	1.5%
Muon ID	1.8%
Tracking*	1-3%
Radiative tail	1%
Offline selections	0.36%
Signal shape	1%
$\mathcal{B}(J/\psi \rightarrow \mu^+ \mu^-)$	0.6%
p_T - y -spectrum*	0.1 -5.0%
MC statistics*	0.3 -5.0%
t_z fits	0.1%

Table 5.6 – Summary of the systematic uncertainties for the measurement of the double differential production cross-section of the J/ψ mesons at the energies of proton-proton collisions of 13 TeV. For sources marked with * we present limits of systematic uncertainty, while its exact value depends on (p_T, y) bin.

Quantity	Systematic uncertainty	
Luminosity	4.6%	reduced by 30%
Trigger	1.5 %	reduced by 50%
Muon ID	2.2%	
Tracking	1%	reduced by 50%
Signal shape	2%	reduced by up to 80% for some bins
p_T - y -spectrum, MC stat. (t_z fits)	1-8%	

Table 5.7 – Summary of the systematic uncertainties for the measurement of the ratio of the double differential production cross-section of the J/ψ mesons at the energies of proton-proton collisions of 13 TeV to that at 8 TeV. Cancellation shows how the correlation of the uncertainties between the two measurements reduced the systematic uncertainty comparing to the quadratic sum of these uncertainties from these two measurements (totally uncorrelated uncertainties).

t_z fit model:

- An alternative model with the additional third wide Gaussian is used for description of the detector resolution. Variation of the F_b is found to be negligible.
- An alternative shape of the t_z distribution of the combinatorial background is extracted from the mass fit with with the *sPlot* technique [58], which yielded in 0.05% variation of the F_b .
- A double exponential function with equal magnitude for positive and negative slope is used as an alternative model for description of the t_z distribution of the wrong PV background. Utilisation of this model in the fit resulted in 0.075% variation of the F_b .

Muon ID Systematic uncertainty of the estimation of the muon identification efficiency consist of the uncertainty of the correction factor described in Section 5.2.2; choice of the binning schema in the tag-and-probe technique; statistics of the calibration sample; and discrepancy of the muon kinematic distributions between simulation and real data. The overall systematic uncertainty originating from ϵ_{MuonID} is found to be 1.8%.

Tracking Systematic uncertainty on the cross-section from the corrections of the track reconstruction efficiency ranges from 1% to 3% depending on the J/ψ kinematic bin.

Radiative tail Shape of the radiative tail of the J/ψ mass distribution was found to be mismodeled during the comparison of the mass distributions obtained for simulated and real candidates. This is accounted for by a systematic uncertainty of 1.0% of the inclusive yield of the J/ψ candidates.

Offline selections The offline selection of the J/ψ candidates is performed in bins of p_T and y and includes cuts on the mass and vertex χ^2 of the dimuon pair. Discrepancies in the distributions of these variables between the data and simulation samples may bias the efficiency estimation. This is taken into account in the systematic uncertainty of $\epsilon_{\text{Reco\&Sel}}$ term. Discrepancies in the J/ψ vertex χ^2 distributions led to the systematic uncertainty in the efficiency of the vertex fit quality requirement of 0.36%.

p_T - y -spectrum To estimate the systematic uncertainty due to the discrepancy in the p_T and y distributions of the J/ψ mesons, the nominal selection efficiency is compared with that obtained from the simulation sample, reweighted to have (p_T, y) distributions identical to that of the data sample. The resulting systematic uncertainty of this source is found to be in the range 0.1 – 5%, depending on the kinematic bin.

Trigger The trigger efficiency is also cross-checked with data. The hardware trigger efficiency is studied on data with a tag-and-probe method. The tag muon of the J/ψ candidate is chosen to trigger the L0Muon line and the efficiency of a single muon to pass through the L0 selection is defined as the fraction of J/ψ candidate with both muons firing the L0Muon line from the number of the candidates which pass through the software selection. This efficiency $\epsilon_{\mu}^{\text{L0Muon}}$ is calculated in bins of $p_{T\mu}$ and η_{μ} . Taking into account that an event pass the L0 selection if at least one muon fire the L0Muon line, the efficiency of the hardware trigger is defined as

$$\epsilon_{\text{tag-and-probe}}^{\text{L0Muon}} = \frac{\Sigma(1 - (1 - \epsilon_{\mu^+}^{\text{L0Muon}}(p_{\mu^+}, \eta_{\mu^+}))(1 - \epsilon_{\mu^-}^{\text{L0Muon}}(p_{\mu^-}, \eta_{\mu^-})))}{N_{\text{tot}}} \quad (5.7)$$

The relative difference between this and the nominal efficiency varies from 1.0% to 5.9% depending on the kinematic bin of J/ψ , and it is taken as a systematic uncertainty of the hardware trigger efficiency. Systematic uncertainty of the software trigger efficiency is estimated using the TISTOS technique [55] as a ratio of the trigger efficiencies calculated on the subsets of data and simulation samples, which pass the trigger selection without

Chapter 5. Measurement of the J/ψ production cross-section

the studied trigger line. This study is also performed in kinematic bins of J/ψ , and the systematic uncertainty of the efficiency is found to be $\sim 1.5\%$.

MC statistics Limited size of the simulation sample leads to a systematical uncertainty in the efficiency in the range from 0.5% to 5% depending on the bin. In each bin, this systematic uncertainty is at least twice smaller than the statistical one.

Luminosity and $\mathcal{B}(J/\psi \rightarrow \mu^+ \mu^-)$ The relative uncertainty of the luminosity determination amounted to 3.9%, and the branching fraction uncertainty of the $J/\psi \rightarrow \mu^+ \mu^-$ decay was taken to be 0.6% [69].

Listed systematic uncertainties are treated as independent and thus uncertainties of the variable are summed in quadratures and propagated to the cross-section values through equation 5.2.

The measurement of the J/ψ production cross-section at the center-of-mass energies of 13 TeV relative to that of 8 TeV allows to cancel some of the systematic uncertainties, due to the correlation of these uncertainties between the two measurements. Uncertainties for the ratio measurement, as well as the cancellations (comparing to the quadratic sum of the uncertainties for measurements at 13 TeV and 8 TeV) are listed in Table 5.7.

5.3 Results

The production cross-section of prompt J/ψ and J/ψ -from- b mesons within the fiducial region ($p_T < 14 \text{ GeV}/c$, $2.0 < y < 4.5$) are measured to be:

$$\begin{aligned}\sigma(\text{prompt } J/\psi, p_T < 14 \text{ GeV}/c, 2 < y < 4.5) &= 15.35 \pm 0.03 \pm 0.86 \mu\text{b}, \\ \sigma(J/\psi\text{-from-}b, p_T < 14 \text{ GeV}/c, 2 < y < 4.5) &= 2.34 \pm 0.01 \pm 0.13 \mu\text{b},\end{aligned}$$

where the first uncertainty is statistical and the second systematic.

Double differential cross-sections in bins of (p_T, y) for the J/ψ -from- b mesons and for the prompt J/ψ mesons and the fraction of the J/ψ -from- b mesons in bins of (p_T, y) are summarized in Appendix B. The production cross-sections and the fraction of the J/ψ -from- b mesons in bins of p_T and y are presented in Figures 5.5, 5.6 and 5.7

The result of the J/ψ -from- b production cross-section allows to measure $b\bar{b}$ production cross-section in proton-proton collisions at the energies of 13 TeV according to the following equation:

$$\sigma(pp \rightarrow b\bar{b}X) = \alpha_{4\pi} \frac{\sigma(J/\psi\text{-from-}b, p_T < 14 \text{ GeV}/c, 2.0 < y < 4.5)}{2\mathcal{B}(b \rightarrow J/\psi X)}, \quad (5.8)$$

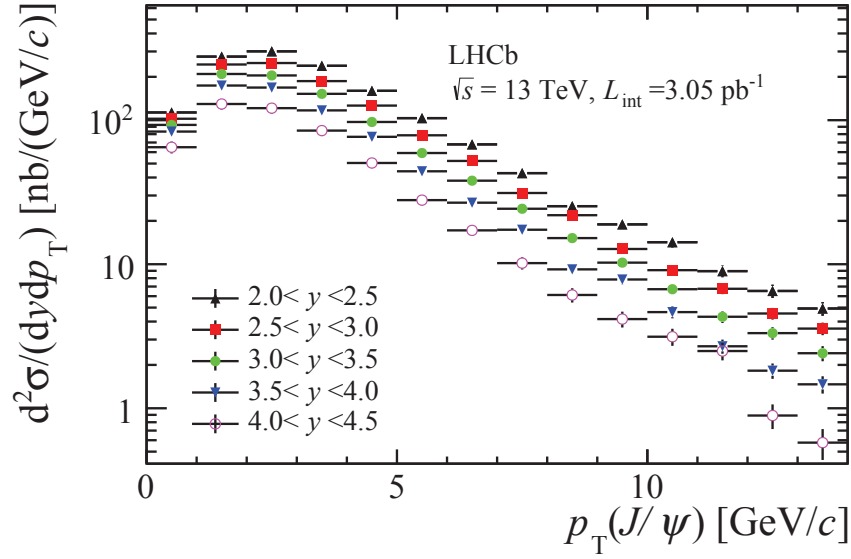


Figure 5.5 – Double differential cross-sections of the the J/ψ -from- b mesons in bins of p_T and y .

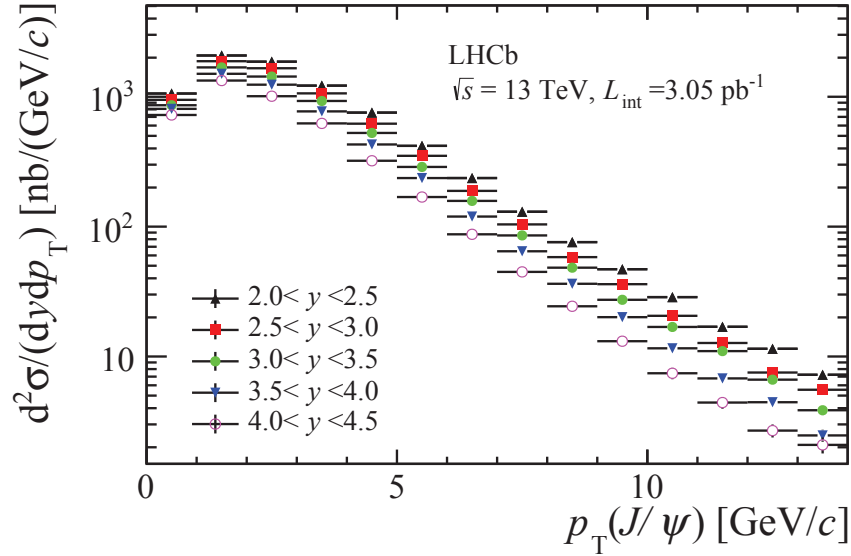


Figure 5.6 – Double differential cross-sections of the prompt J/ψ mesons in bins of p_T and y .

where $\alpha_{4\pi}$ is the extrapolation factor to the full solid angle. Using a tuning of PYTHIA 6 for LHCb this number is found to be 5.2. Together with $\mathcal{B}(b \rightarrow J/\psi X) = 1.16 \pm 0.10\%$ [69] we obtained $\sigma(pp \rightarrow b\bar{b}X) = 515 \pm 2 \pm 52$ mb, where the first uncertainty is statistical and the second is systematic.

The results obtained at the centre-of-mass energy of 13 TeV are compared with that one of smaller energies [85, 86, 91]. The values of the production cross-section measured at lower

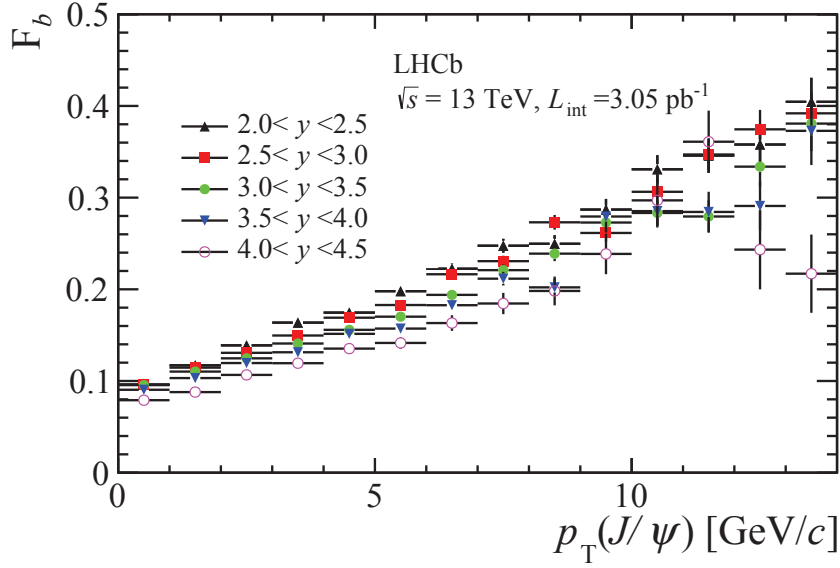


Figure 5.7 – Fraction of the J/ψ -from- b mesons in bins of p_T and y .

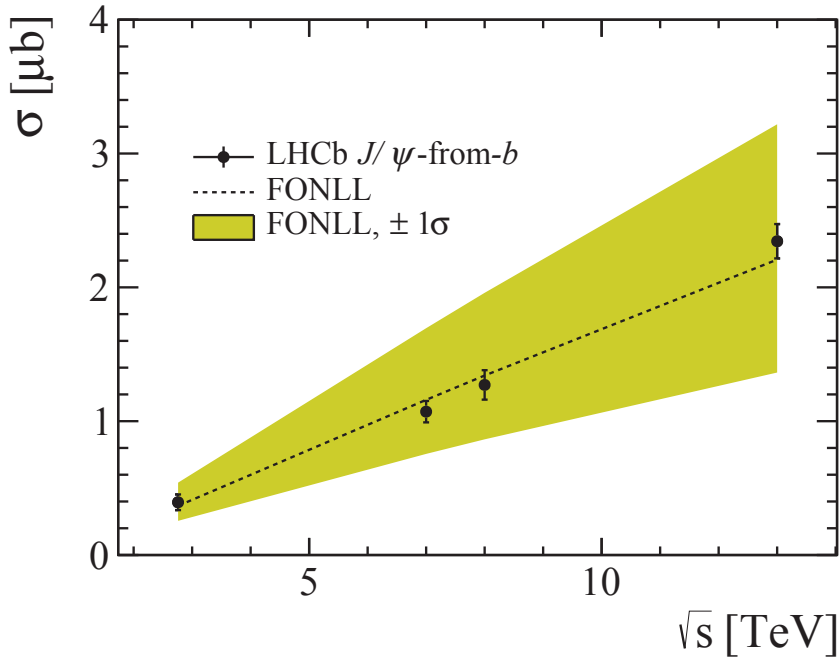


Figure 5.8 – The J/ψ -from- b production cross-section as a function of pp collision energy in the LHCb fiducial region compared to the FONLL calculation [8].

energies are corrected in order to account for the new measurements of the branching fraction value, $\mathcal{B}(J/\psi \rightarrow \mu^+ \mu^-) = (5.961 \pm 0.033)\%$ [69]. The cross-section within LHCb fiducial region of the prompt J/ψ mesons and the J/ψ -from- b mesons at the energies of 2.75 TeV, 7 TeV, 8 TeV

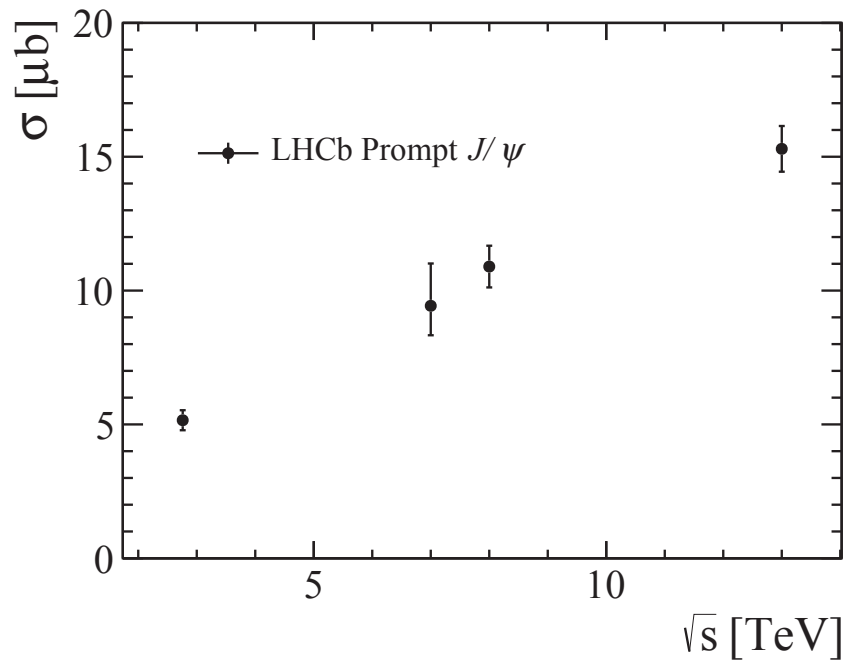


Figure 5.9 – The prompt J/ψ production cross-section as a function of pp collision energy in the LHCb fiducial region.

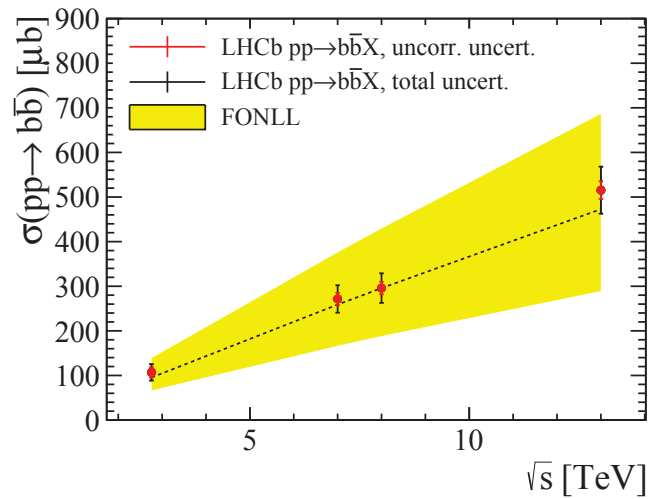


Figure 5.10 – Production cross-section of the b -quark is extrapolated to the full solid angle and compared to the FONLL predictions [8].

and 13 TeV are summarized in Table 5.8. The dependence of the production cross-section of the J/ψ mesons within the LHCb fiducial region and the production cross-section of the b -quark integrated within the full solid angle from the energy of the pp collisions is presented in Figures 5.8, 5.9 and 5.10.

Chapter 5. Measurement of the J/ψ production cross-section

The comparison of the dependencies of the production cross-sections of the prompt J/ψ mesons and the J/ψ -from- b mesons from the transverse momentum and the rapidity measured at the energies of the proton-proton collisions of 13 TeV and 8 TeV are shown in Figure 5.11. The double differential production cross-section measured at $\sqrt{s} = 13$ TeV relative to that at $\sqrt{s} = 8$ TeV for the J/ψ -from- b mesons and for the prompt J/ψ mesons are summarized in Appendix B and are shown in Figure 5.12.

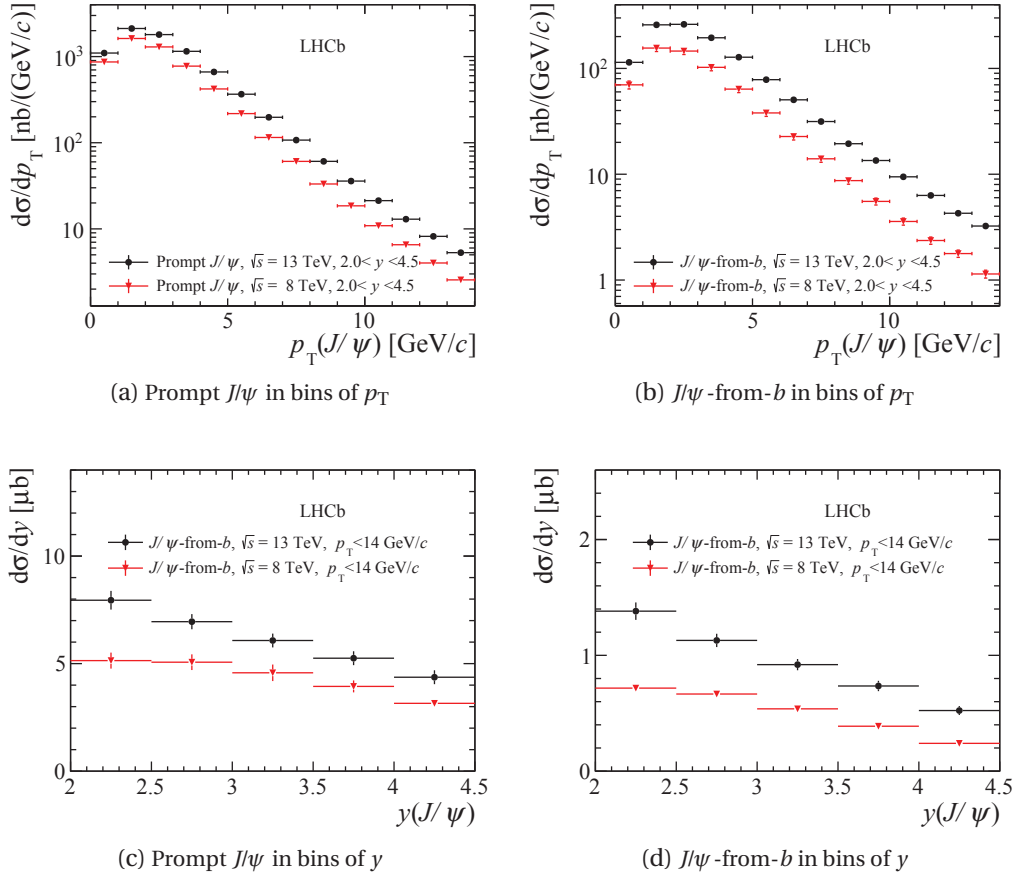


Figure 5.11 – The J/ψ production cross-section for the prompt J/ψ and the J/ψ -from- b mesons as a functions of p_T and y measured at the energies of 13 TeV (black) and 8 TeV (red).

Table 5.8 – Production cross-sections of prompt J/ψ and J/ψ -from- b mesons, integrated over LHCb fiducial region, in pp collisions at various center-of-mass energies. The first is the total uncorrelated uncertainty, and the second the total correlated uncertainty.

σ_{tot} (μ b)	$\sqrt{s} = 2.76$ TeV	$\sqrt{s} = 7$ TeV	$\sqrt{s} = 8$ TeV	$\sqrt{s} = 13$ TeV
Prompt J/ψ	$5.2 \pm 0.3 \pm 0.3$	$9.43 \pm 0.47^{+0.72}_{-0.99}$	$10.9 \pm 0.5 \pm 0.6$	$15.4 \pm 0.6 \pm 0.6$
J/ψ -from- b	$0.40 \pm 0.04 \pm 0.04$	$1.07 \pm 0.05 \pm 0.06$	$1.27 \pm 0.06 \pm 0.09$	$2.36 \pm 0.09 \pm 0.09$

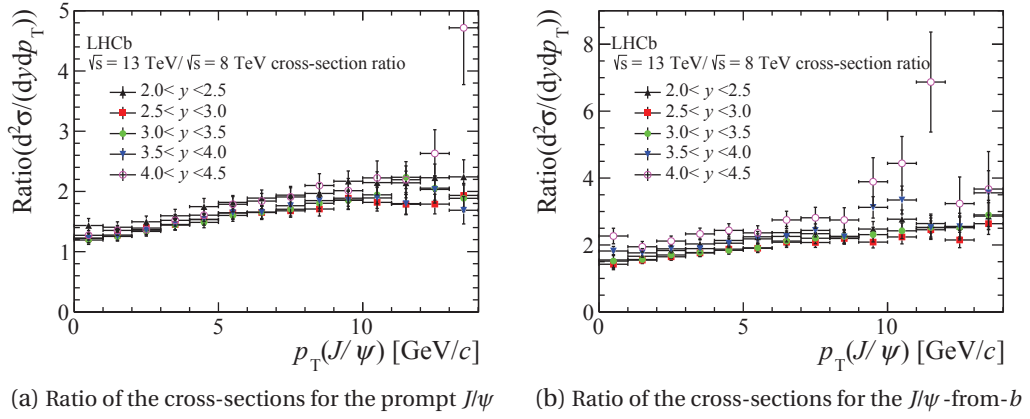


Figure 5.12 – Ratio of the double differential production cross-section of the prompt J/ψ and the J/ψ -from- b mesons measured at the energy of pp collisions of 13 TeV to that at 8 TeV.

5.3.1 Comparison with theoretical results

The measured production cross-sections of the prompt J/ψ and J/ψ -from- b mesons are compared with the predictions of the NRQCD calculations and the FONLL calculations, respectively. Figure 5.13 shows a good agreement of the theoretical predictions with the measured production cross-section values in bins of p_T . As shown in Figure 5.8, the FONLL approach allows to describe well the dependence of the integrated cross-section value on the energy of the pp collisions.

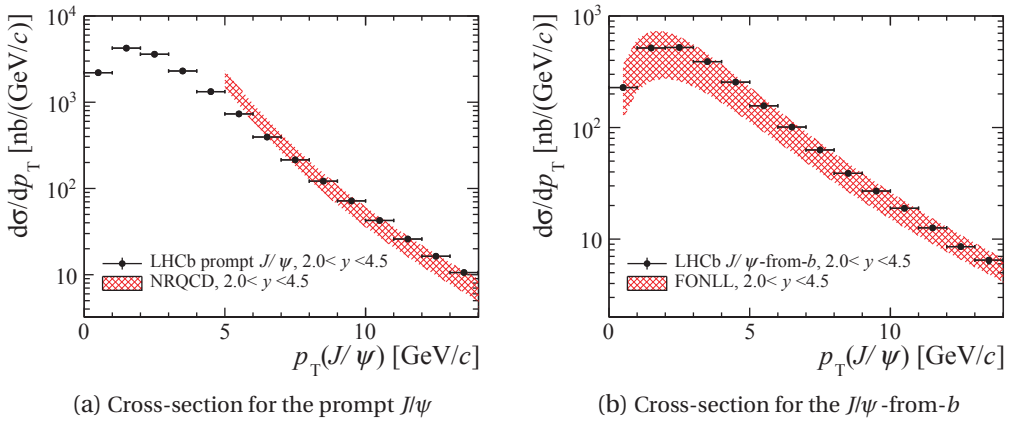


Figure 5.13 – Comparison of the production cross-section of the prompt J/ψ and the J/ψ -from- b mesons in bins of p_T with the theoretical predictions.

As it has been discussed in Section 5.2.5, the calculation of the ratio of the cross-section measurements allows to reduce systematic uncertainties of the measurement. However, the highest benefits of this approach are achieved for the theoretical predictions. For example, the leading uncertainty of the NRQCD prediction, caused by LDME, canceled almost completely.

The calculation of the ratio also allows to improve the FONLL predictions. Since the scale choice made at the two energies (8 TeV and 13 TeV) is correlated, uncertainties of this type are partially canceled. Other parameters such as the heavy quark mass, the fragmentation fractions to specific hadrons, the fragmentation functions and the decay branching ratios are also fully correlated at the different energies and lead to the negligible systematic uncertainties in the cross-section ratios [7]. Thus, the main sources of the remaining uncertainty of FONLL predictions for the cross-section ratios are the scale dependence, the choice of the heavy quark mass and the parton distribution functions (PDF).

The comparison of the measured values of the ratios of the production cross-sections with the theoretical predictions for the prompt J/ψ mesons and the J/ψ -from- b mesons are shown in bins of p_T and y in Figure 5.14. It's interesting to notice that the underestimation of the measured production cross-section in lower y bin by FONLL predictions is also observed in recent measurement of production cross-section of prompt D^0 and D^+ mesons in the early Run II data at LHCb [9] (see Figure 5.15).

5.4 Conclusion

The `Turbostream` technique is used for the first time in this analysis. This proves it to be reliable tool for data analysis and established the procedure for future applications. Moreover, being the first analysis on the Run II data, this study indicated and allowed to fix a number of bugs in the simulation software, which was changed during the shutdown from 2012 to 2015.

Using the data sample corresponding to $3.05 \pm 0.12 \text{ pb}^{-1}$ collected in the pp collisions at the energy of 13 TeV in July 2015, the double differential production cross-sections of the prompt J/ψ and J/ψ -from- b mesons is measured in bins of rapidity and transverse momentum. These measurements leads to the estimation of the integrated production cross-sections and production cross-section of the b -mesons. The ratios of the J/ψ cross-sections in pp collisions at a center-of-mass energy of 13 TeV relative to those at 8 TeV are also determined.

Differential production cross-section of the prompt J/ψ mesons at 13 TeV and its ratio to that at 8 TeV are compared with the expectations from the NRQCD approach. Theoretical predictions are in a good agreement with data.

The FONLL predictions are in an agreement with the measurement of the integrated and the double differential production cross-section for the J/ψ -from- b mesons. However, this prediction underestimates the ratio of the differential production cross-sections obtained at the energies of pp collisions of 13 TeV and 8 TeV.

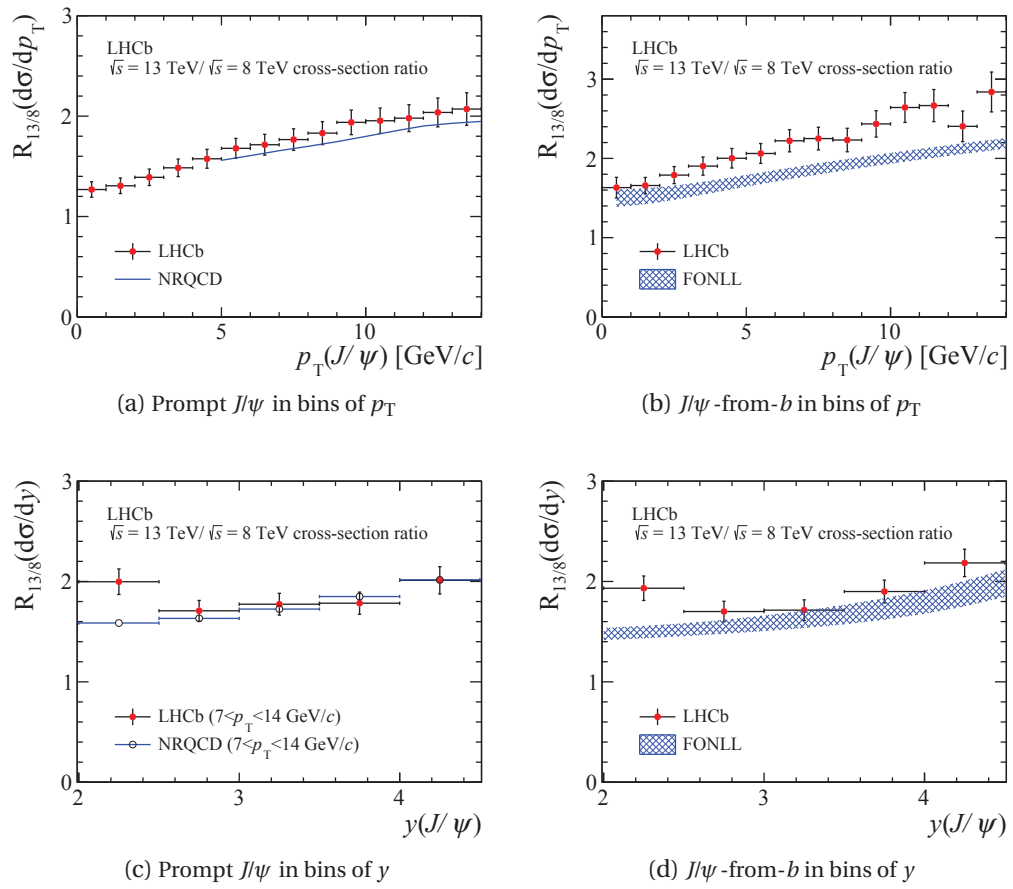


Figure 5.14 – The J/ψ production cross-section for the prompt J/ψ and the J/ψ -from- b mesons as a functions of p_T and y measured at the energies of 13 TeV (black) and 8 TeV (red) compared to the theoretical predictions of the NRQCD and the FONLL. Systematical uncertainty of the NRQCD prediction is not shown.

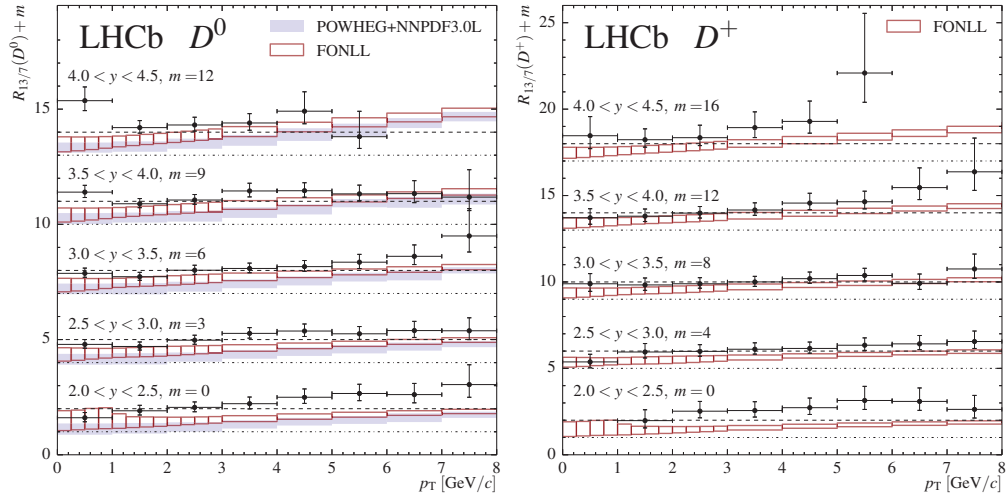
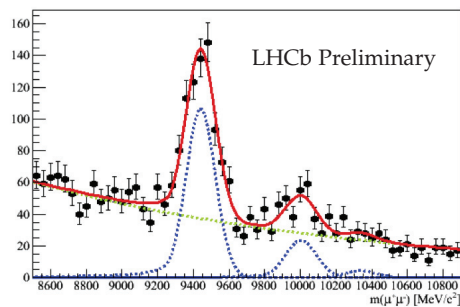


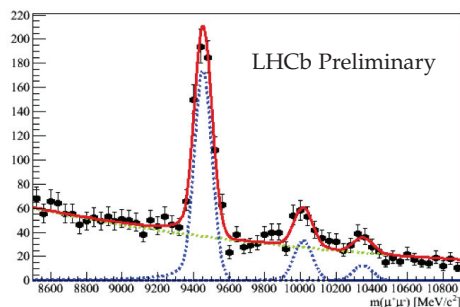
Figure 5.15 – Measurements and predictions of the prompt D^0 (left) and D^+ (right) cross-section ratios. The dash-dotted lines indicate the unit ratio for each of the rapidity intervals and the dashed lines indicate a ratio of two. Each set of measurements and predictions in a given rapidity bin is offset by an additive constant m , which is shown on the plot [9].

6 LHCb Silicon Tracker - Performance and monitoring

Quality of track reconstruction is crucial for nearly every analysis of the LHCb program since it determines momentum resolutions, quality of vertex reconstruction and is an input for particle identification. Permanent monitoring and calibration of the detector is essential to provide good-quality data for the experiment. This chapter is devoted to analysis of the performance of the Silicon Tracker of the LHCb detector and an overview of the framework developed for the online monitoring of its performance.



(a) $\sigma = 92 \text{ MeV}/c^2$



(b) $\sigma = 49 \text{ MeV}/c^2$

Figure 6.1 – Comparison of dimuon mass distribution before (left) and after (right) online-alignment procedure. Usage of outdated alignment information deteriorates mass resolution by a factor of two.

Chapter 6. LHCb Silicon Tracker - Performance and monitoring

The Silicon Tracker (ST) system of the LHCb experiment is divided in two subsystems, the Inner Tracker (IT) and Tracker Turicensis (TT). The IT consists of three identical stations (IT1, IT2 and IT3) placed downstream of the LHCb magnet, while the TT is a single station placed upstream of the magnet. Each station is composed of four layers of silicon sensors. The external layers ($x1$, $x2$) have vertically oriented micro-strips, while strips in the internal layers (u , v) are tilted at $\pm 5^\circ$ degrees from the vertical. Each layer of the station consists of many sensors grouped into readout sectors, as shown in Figure 6.2 for the IT (left) and the TT (right). The TT layers are constructed using identical $500\mu\text{m}$ thick, 9.64 cm wide and 9.44 cm long long sensors, while there are two kinds of sensors in the IT layers: 7.6 cm wide, 11 cm long and $320\mu\text{m}$ or $410\mu\text{m}$ thick. The thinner sensors are located above and below the beam pipe. The alignment of the tracking detector is essential for the physics program. Figure 6.1 shows the difference in mass resolution between dimuon signals reconstructed with and without an aligned tracker.

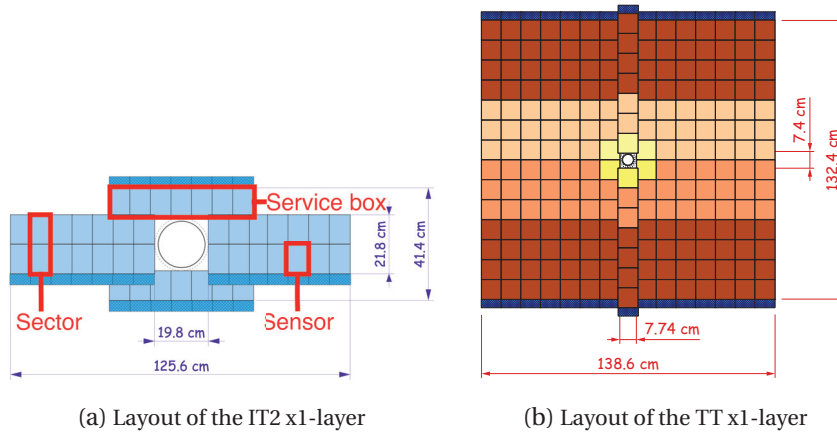


Figure 6.2 – Layout of the (a) IT and (b) TT. Readout sectors in the IT consist of one (upper and lower boxes) or two (left and right boxes) sensors, while the sectors of the TT have one to four vertically grouped sensors according to the color scheme.

6.1 Performance of the LHCb ST

A sketch of a charged particle intercepting an ST sector is shown in Figure 6.3. The track is reconstructed by a Kalman filter [113] algorithm using hits on various layers of the tracking system. Residuals are defined for hits that are associated to a track. A charged particle passing through the microstrips fires several strips (cluster), creating peaking ADC count distributions. A cluster is defined as a group of up to four contiguous strips registering an ADC value that exceeds the noise level of those channels by a factor of 2.5 at least. The hit residual r is defined as the distance between the expected position of the hit and the line parallel to the strips of the given sensor that passes through the centre of the ADC peak in the fired cluster. For each hit we define variance the in the measurement V from the shape of the ADC count distributions and, if the hit is associated to a certain trajectory, the variance in the residual D from the fit of

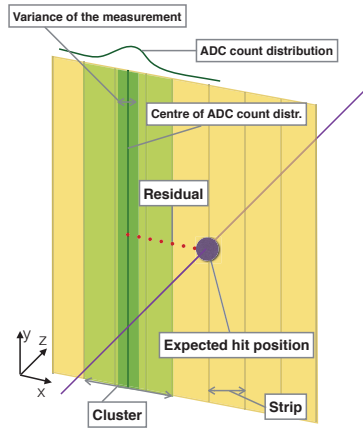


Figure 6.3 – Interception of charged track with ST sector.

the track.

The tracking performance in the ST sectors is characterized by three variables:

- **Hit efficiency** The hit efficiency is the ratio of the number of observed hits over the number of “expected” hits, where the latter are defined as the intercepts of the extrapolation of the reconstructed track with the sensitive regions of the sector. To obtain the “observed hits” after the extrapolation, a search is made for an observed hit within a $\pm 400 \mu\text{m}$ window around its expected position.
- **Hit resolution** For hits associated to tracks, variance in the residual D accounts effect of multiple scattering, which is irrelevant for the resolution of a single sector. Thus we define a new variable, the “r.m.s. unbiased residual” [114] as

$$r^{rms} = r \times \frac{V}{D} \quad (6.1)$$

The width of the r.m.s. distribution for hits collected from different tracks for the same sector depends only on the properties of the sector, and thus is taken as a hit resolution.

- **Hit bias** The “unbiased residual” r^u [115] is introduced to avoid the bias of the track position by the examined hit. Since the track fit provides information on the variance in the measurement V and the variance in the residual D it is possible to find the unbiased residual without refitting the whole track:

$$r^u = r \times \frac{V}{D} \quad (6.2)$$

Chapter 6. LHCb Silicon Tracker - Performance and monitoring

The hit bias is thereby defined for ST sector as a mean of the "hit unbiased residual", r^u , distribution.

This section reports performance of the ST during the 2012 and 2015 data-taking periods. Previous studies are reported in Ref. [116].

6.1.1 Description of the data sets

The analysis of the ST performance in 2012 and 2015 uses track samples enriched in pairs of well-identified detached muons with an invariant mass close to the J/ψ resonance and with transverse momentum larger than $500 \text{ MeV}/c$. In addition to the stripping line requirements, tracks are required to correspond to muons with minimal momentum of $10 \text{ GeV}/c$ and must be "well reconstructed", i.e., they must fulfill the requirements presented in Table 6.1. Values of the performance parameters of the ST sectors are compared with expectations obtained from Monte-Carlo simulated samples of $J/\psi \rightarrow \mu\mu$ events selected as data.

Table 6.1 – Requirements for tracks used in the ST performance analysis. The quantity $\chi^2_{\text{system}}/\text{ndf}$ refers to the track χ^2/ndf contribution from the specific subset of the tracking stations defined in Ref. [10].

Variable	Value
P	$> 10 \text{ GeV}/c$
Track χ^2/ndf	< 2
$\chi^2_{\text{Full}}/\text{ndf} - \chi^2_{\text{Upstream}}/\text{ndf} - \chi^2_{\text{Downstream}}/\text{ndf}$	< 2
Track $\chi^2_{\text{Downstream}}/\text{ndf}$	< 2
Track $\chi^2_{\text{velo}}/\text{ndf}$	< 2
Track type	Long

6.1.2 Results

A summary of the performances averaged between sectors for the TT and IT detectors in 2012 and 2015 is presented in Table 6.2. Some variations in performance between 2012 and 2015 are observed: slight ($\sim 0.1\%$) decrease of the hit efficiency (see figure 6.4); a $\sim 50\%$ reduction in the average bias (see Figure 6.5) caused by the improvements in the alignment procedure; and a $\sim 0.5\%$ resolution deterioration (see Figure 6.6) due to increased multiplicity. A number of observed phenomena remain of difficult interpretation

- A lower hit efficiency for sectors in IT3 (the most distant station from the collision point) compared to that of IT1 and IT2 was observed in 2012 and this effect became more significant in 2015 (see Figure 6.7). This effect is not reproduced by simulation (see Figure 6.8).

6.1. Performance of the LHCb ST

Table 6.2 – Summary of averaged ST performance during the 2012 and 2015 data-taking. Performance variables were weighted with the number of hits during the averaging between the sectors.

	TT		IT	
	2012	2015	2012	2015
Hit efficiency, %	99.7	99.5	99.9	99.8
Abs. bias, μm	6.2	1.6	4.1	2.1
Hit resolution, μm	49.5	49.7	51.1	52.0

Table 6.3 – Changes of hit detection efficiency of TTbXRegionBSector18 during the 2015 caused by progressive malfunctioning of the bond wires.

Month	Efficiency
September	$89.0 \pm 0.1\%$
October	$87.6 \pm 0.7\%$
November	$69.0 \pm 0.2\%$

- Lower efficiency in the outer sectors of the A- and C- side IT boxes (located from left and right sides of the beam pipe) in 2012 compared to other IT sectors. This effect is not reproduced by simulations and disappeared during 2015 (see Figures 6.7 and 6.8).
- Lower r.m.s. of the residual distribution in the x-layers¹ of top and bottom IT boxes, which was observed both in 2012 and 2015, and is not confirmed by simulation. (see Figures 6.9 and 6.10)

The average hit detection efficiency of the ST sectors in 2015 was higher than 99% but three sectors have much lower values (85-97%). Some of the low efficiencies observed in 2012 are explained by the high noise in these sectors. Efficiency of one of the sector decreased during 2015 as shown in Table 6.3, which is explained by progressive breaking of the bond wires that connect the silicon strips to the readout electronics. Problem with this sector was detected very close to start of the 2016 data-taking, which made impossible its replacement with fixed sector.

A full set of performance plots obtained during analysis of data and simulation is presented in Appendix A and the description of a novel software developed for analysis of ST performance may be also found in Appendix 6.2.

¹X-layers are the layers with silicon strips oriented strictly vertically.

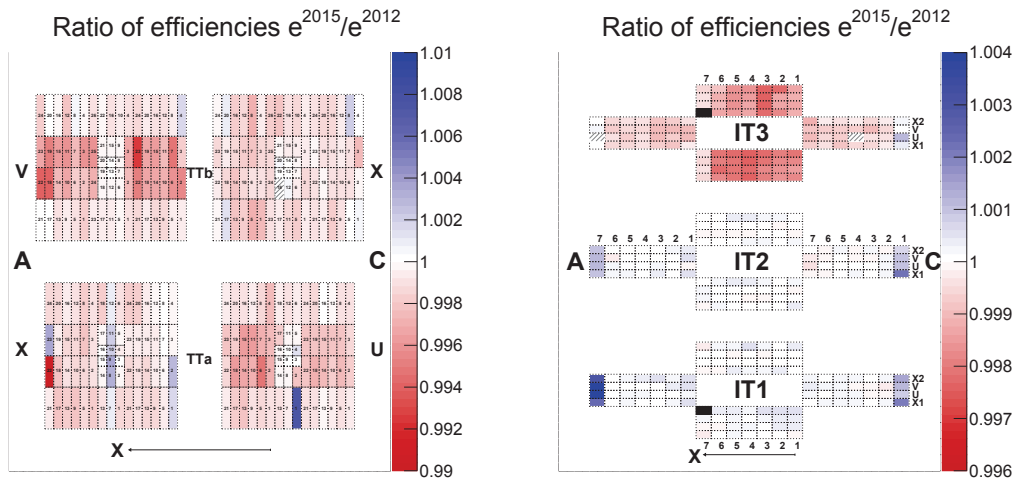


Figure 6.4 – Map of the ratio of hit efficiency in 2015 data to that in 2012 data.

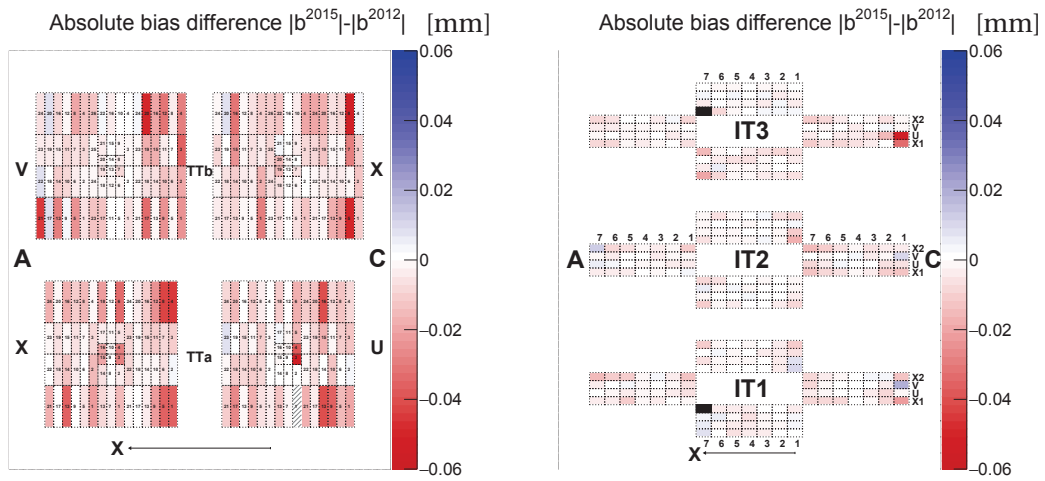


Figure 6.5 – Map of the difference of absolute bias of residual distribution between 2015 and 2012.

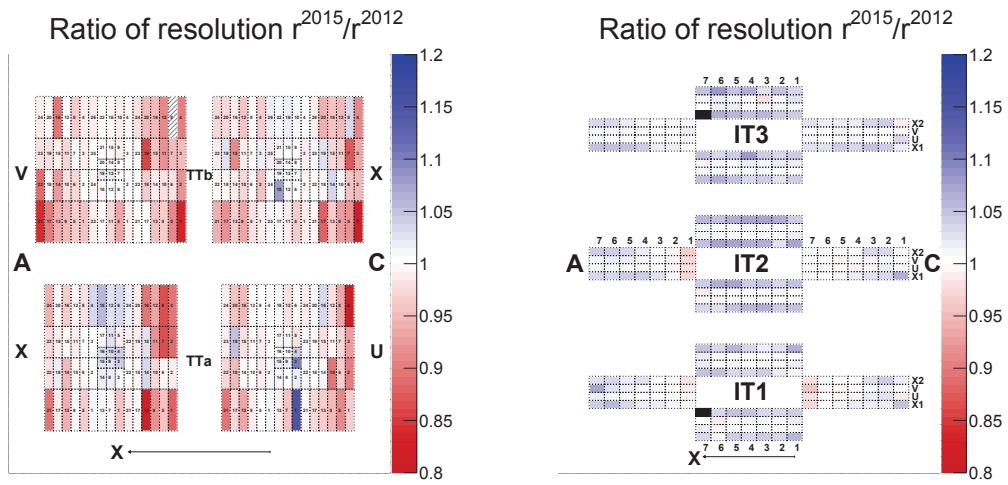


Figure 6.6 – Map of the ratio of resolution in 2015 data to that in 2012 data.

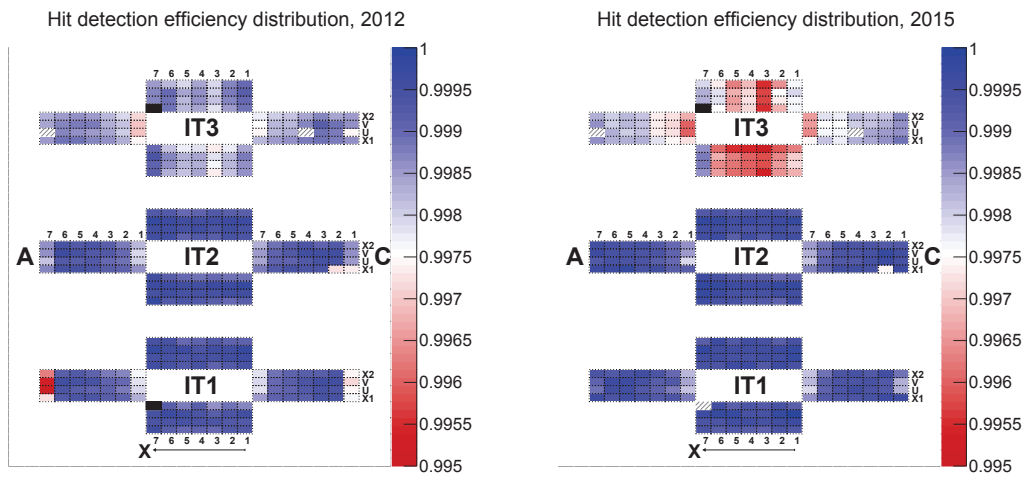


Figure 6.7 – Hit detection efficiency map of IT sectors in 2012 (left) and in 2015 (right). Hashed regions are out of colour scheme.

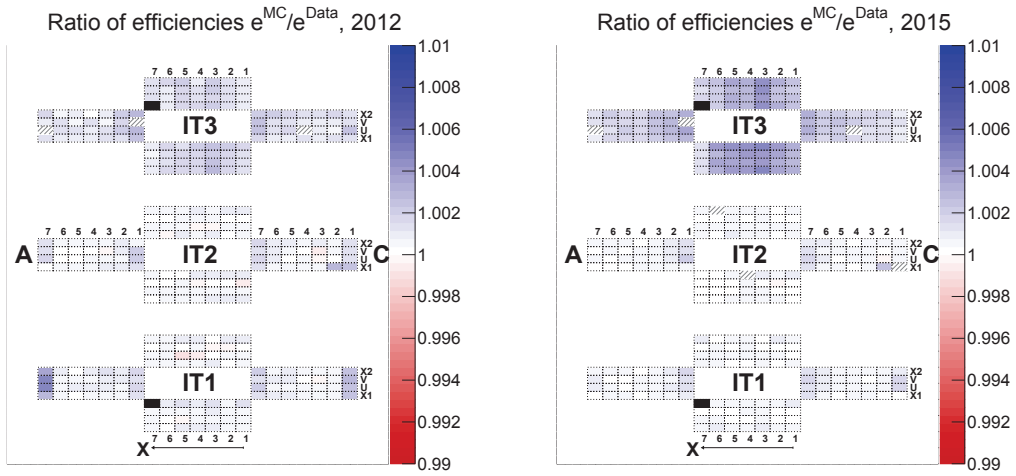


Figure 6.8 – Map of the ratio of hit detection efficiency of IT sectors found in simulation to that found in data for 2012(left) and for 2015 (right). Hashed regions are out of colour scheme.

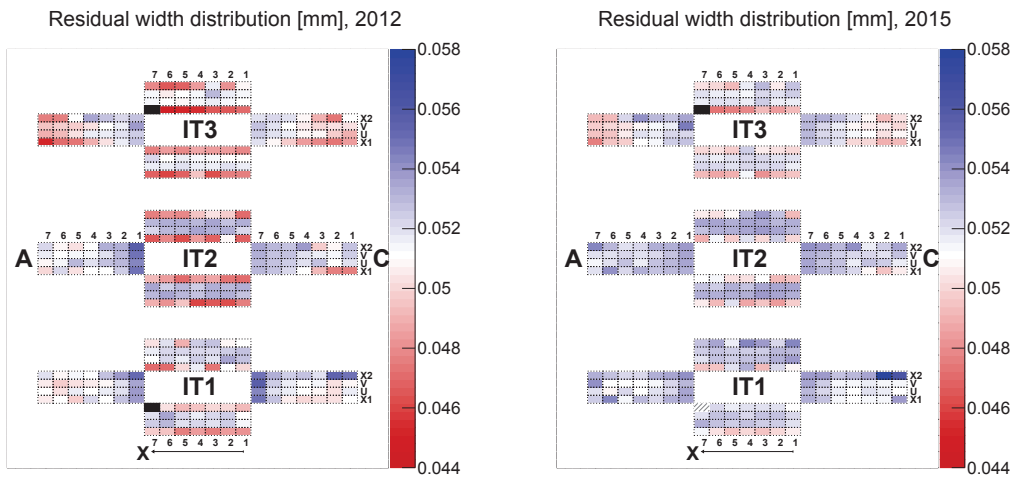


Figure 6.9 – Hit resolution (r.m.s. of the residual distribution) map of IT sectors in 2012 (left) and in 2015 (right). Hashed regions are out of colour scheme.

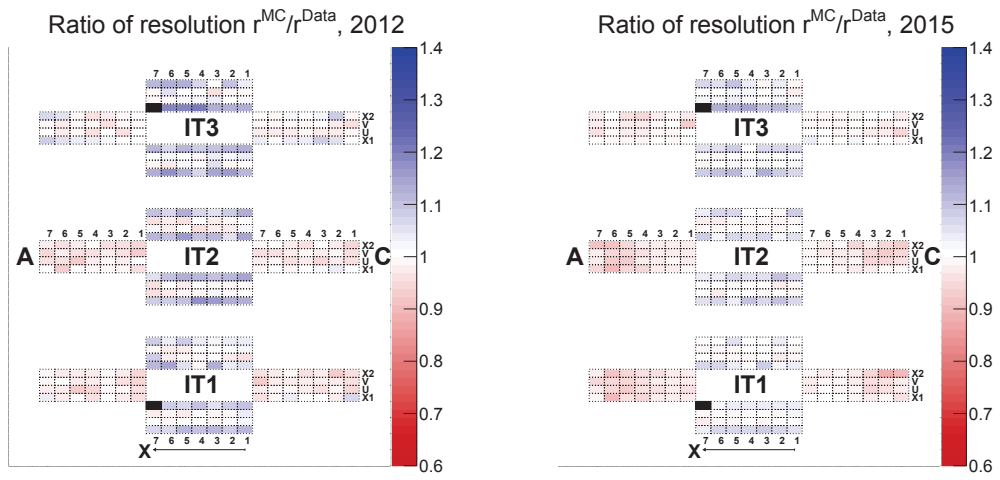


Figure 6.10 – Map of the ratio of hit resolution of IT sectors found in simulation to that found in data for 2012(left) and for 2015 (right). Hashed regions are out of colour scheme.

6.2 ST software development

The TT and IT detectors consist of 280 and 336 readout sectors, respectively. Simultaneous analysis of their performance is possible using 2D histograms mapped to the detector layout. However, the study of the individual sector performance is challenging as there are many individual performance plots, a few plots per each sector. This motivated creation of the novel set of ST analysis tools aimed for simultaneous and interactive study of big number of performance plot. This work includes two major elements, the “STTrackTuple” algorithm and the “ST Interactive Map” described below.

6.2.1 STTrackTuple algorithm

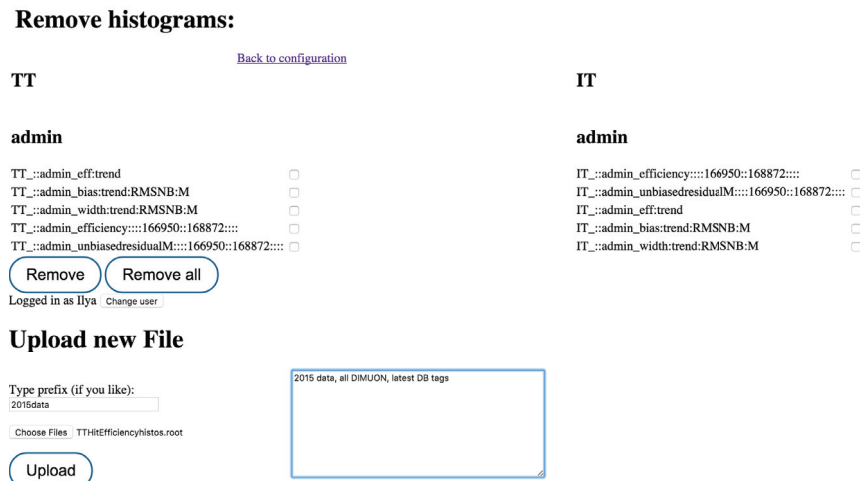
The STTrackTuple algorithm [117] is created as a part of the standard LHCb ST monitoring package and bases on existing algorithms, but produces tuples of track-by-track information instead of histograms, which give access for studies of ST performance dependencies, such as, for example, time variations of ST performance. The algorithm may operate in “Efficiency” or “Monitoring” mode. In both modes, the algorithm iterates over tracks from an input container.

In the “Efficiency” mode, the algorithm propagates tracks through the model of the detector and defines the expected positions of the hits for each readout sector. Then, the algorithm iterates over the hits obtained by the algorithm that identifies clusters and searches for hits within the acceptance window ($\pm 300\mu\text{m}$) of the expected hit position. In case of success, the hit is flagged “found” and the algorithm defines its residual. Otherwise, the hit is flagged “not found”. Each track is represented by a set of expected and found hits in certain sectors. Information on the sectors and hits are stored in arrays, which are written to the tuple. Thus, the information on n -th hit of the given track is stored on n -th position of the arrays in the tuple. In the “Monitoring” mode, the algorithm iterates over the hits that compose the track and stores information on the hits similarly as in the “Efficiency” mode.

The benefit of this approach is to store detailed information associated with every hit, which includes track properties and run number. This allows variations of the ST performance versus time and its dependence on track parameters to be studied. However, the output of the STTrackTuple algorithm needs to be post-processed in order to extract the desired histograms. This is done by means of a dedicated package [118]. With this package, the output from STTrackTuple can be stored in the form of per-sector histograms, which can be analysed in the ST Interactive Map presented in the next section. The package also contains tools for simple analysis of the histograms and creation of the 2D performance plots in publication-ready format. All performance plots in this document were created by this package.

6.2.2 ST Interactive Map

ST Interactive Map (STIM) is a web-based application written in the Flask [119] framework. It automatically maps root files containing histograms for each sector with the detector layout and provides easy access to colour schemes for plots and to the histograms. Root files can be obtained directly as the output of the monitoring algorithms, or they can be obtained with the package that formats the output of the STTrackTuple algorithm to histograms [118].



(a) File management page.



(b) Configuration page.

Figure 6.11 – Screenshots of STIM on the file management page (left) and the histogram configuration page (right).

Users may upload root files through the browser to the STIM (see Figure 6.11 (left)), where they are processed and saved to a mongo-based [120] database. Each entry to the database is a snapshot of the TT or IT detector. In this snapshot, each readout sector has the results

Chapter 6. LHCb Silicon Tracker - Performance and monitoring

of the statistical analysis of the corresponding histogram and reference to the image of this histogram stored in png format. Moreover, every database entry is associated with a set of colour schemes defined for each function useful for the statistical analysis. These schemes allow the detector map to be coloured depending on the mean value, r.m.s., maximal and minimal bin contents and the results of the fit of the histogram with a linear function (this is especially useful in the analysis of time dependences). The user may add information on data-taking condition, software versions, etc, which is visible in the configuration page.

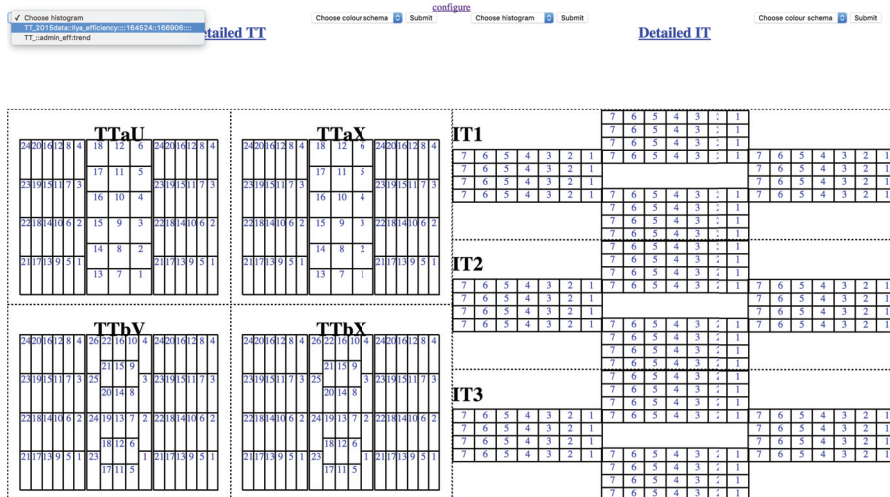


Figure 6.12 – Screenshot of STIM on home page during histogram selection.

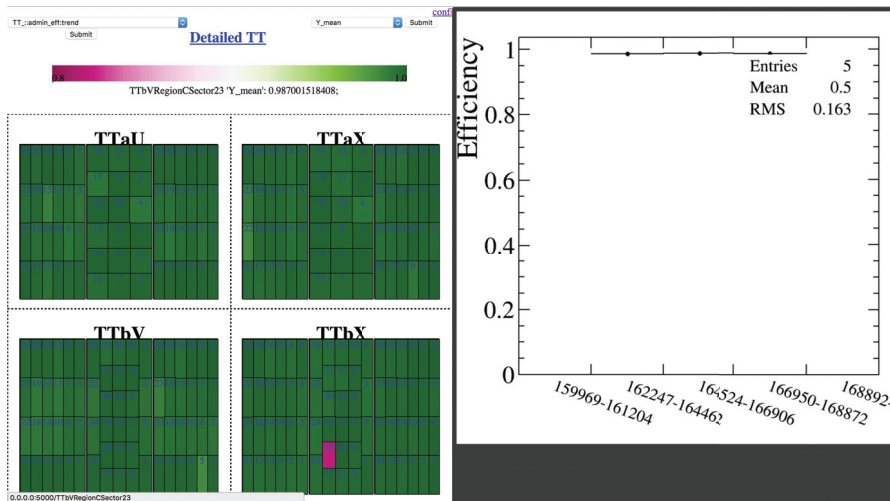


Figure 6.13 – Screenshots of STIM with the TT map coloured with the mean hit efficiency, obtained from efficiency trends. Such a trend is presented for readout sector “TTbVRegionCSector23” on the right side of plot, and it appears there when moving cursor over this sector.

Once files are uploaded, the user may choose histograms of interest in the configuration page (see Figure 6.11 (right)). This page shows all existing detector snapshots, grouped by detector name and owner. Information on a specific set of histograms may be obtained with

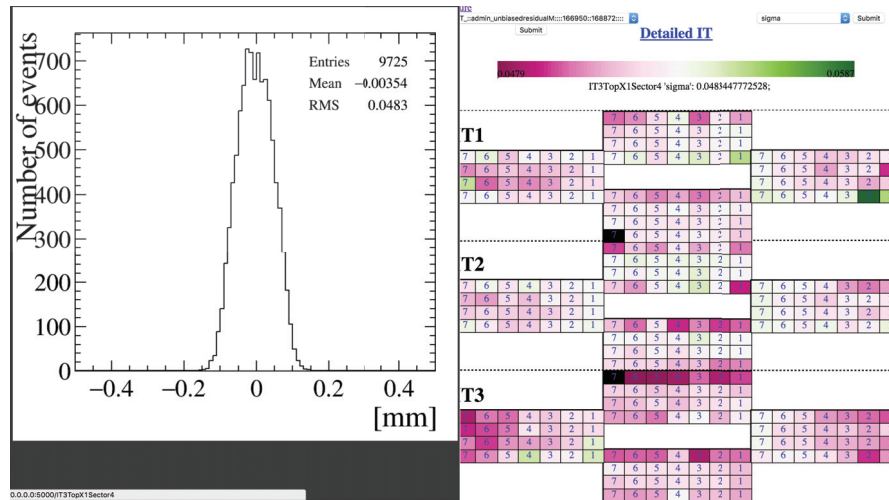


Figure 6.14 – Screenshots of STIM with the IT map coloured with the r.m.s. of the hit residual histogram.

an intuitive cursor-based procedure. As soon as the user chooses a set of histograms, he or she proceeds to the main page, which contains schematic maps of the TT and IT detectors. The top of the page contains pop-down menus, which allow a histogram and colour scheme to be chosen (see Figures 6.12, 6.13 and 6.14). Once the detector is coloured with the chosen colour scheme, it is possible to visualise per-sector histograms by placing the cursor over the sector.

6.3 ST performance monitoring

The implementation of an online alignment procedure allows for performing nearly online (*i.e.*, once per fill) performance monitoring of the ST as well. The online alignment runs on a small subset of data (approximately 50×10^3 events) collected at the beginning of every fill. Preliminary studies shows that these data, enriched with J/ψ decays analogously to Section 6.1, are sufficient to control the main performance variables for most of the ST sectors, with the exception of a few outer sectors of TT, which are expected to have less than one hit per every 500 events.

We implement online ST performance monitoring through two complimentary components. The first part will be run by the standard LHCb monitoring facilities, which aims to alert data managers² of sudden malfunctions of the detector. This branch of the monitoring activities is described in Section 6.3.1. The second component of the online monitoring is described in Section 6.3.2, and aims at providing interactive information about the current performance of the ST and its historical changes. It is designed to be used by detector and alignment experts.

Both elements of the monitoring system use the same information, which is processed during the online alignment. Algorithms gathering this information are grouped in a python script,

²data managers are people providing online data monitoring and data quality control directly during the data-taking

Chapter 6. LHCb Silicon Tracker - Performance and monitoring

which is part of the standard monitoring package. As a part of the online alignment master program, the algorithm adds summary performance plots to the standard alignment output file for a penalty of a 5% increase of the timing budget and the size of the output histogram file.

The summary performance plots of the hit bias and hit resolution consist of 2D histograms where each entry corresponds to a hit associated with a track in the ST with the hit residual (unbiased residual for bias and r.m.s. unbiased residual for resolution) on the Y-axis, organised in bins corresponding to different readout sectors. One-dimensional histograms obtained by slicing the summary histograms in X bins are residual distributions for the corresponding ST sectors and thus contain information on the bias and resolution.

The summary plots of the efficiency consist of 1D histograms containing the number of expected and observed hits, sector-by-sector, which allows to determine hit detection efficiency of each sector.

6.3.1 Data manager monitoring

The main purpose of this component of the performance monitoring is to alert the LHCb data manager to sudden malfunctions of the detector through the alarm panel. Having added performance histograms to the presenter [121], it is possible to detect anomalies in the distribution of key observables, thus triggering an alarm that is handled by the data manager. The data manager is expected to monitor performance histograms of ST displaying hit detection efficiency, bias and resolution of sectors. The information required to fill these histograms will be taken from the output of the online alignment job, and the histograms themselves will be created and added to the histogram database by a dedicated monitoring process.

6.3.2 Expert monitoring

The “expert” component for ST performance monitoring is called “ST Interactive Monitor” and its functional scheme is shown in Figure 6.15. The interactive monitor is an application running on an online computer, which provides information on the ST performance through a web interface. The operation of this tool is provided by three entities: a histogram processing daemon that collects the data output from alignment jobs and writes it to the performance database; the performance database, containing performance summaries from previous runs; and a server that queries this database and displays its content through a web interface.

While LHCb has a centralised database to store monitoring histograms, we developed a stand-alone dedicated database, which provides much faster response and better organisation of data because it is tailored for the specific task at hand. Unlike the official LHCb histogram database, our database does not store performance histograms themselves, but just performance variables for each sector. In this database, data are structured in two types of documents, “snapshots” and “sectors”. A sector document contains performance information

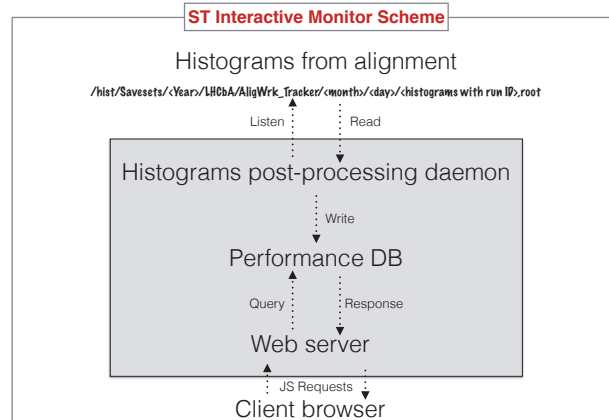


Figure 6.15 – Functional scheme of ST interactive monitor. Gray area contain instances running on LHCb online machine.

for some ST sector estimated for some fill, while a snapshot document contains links to all sector documents corresponding to the same fill, which is schematically presented in Figure 6.16. In order to operate with the database, we use python scripts providing the following functionalities

- Check of availability of the new output of the online alignment. This script is ran automatically every 30 seconds with standard OS tools;
- Parsing of the output file of the online alignment job and filling of the database with corresponding performance numbers. This function is called by the script described above if a new alignment output is found;
- Clean the whole database or remove specific entry from it;
- Fill database with random data.

The server application query the database with a list of fills to display, gets a python dictionary with performance numbers in response and renders the web page using it. An example of the application web page is shown in Figure 6.17. The page has controls to define the displayed information on the left and the rest of the screen is divided in two parts to display maps of the TT and IT detectors.

The ST sectors are coloured according to the selected statistics (minimum, maximum or mean) and with user-defined scale boundaries for the set of chosen performance observables (hit detection efficiency, bias or resolution) in the given run range. The observable to view and the associated statistics can be selected on the left side of the page using the “Trend” and “Property” options. Locating the cursor over a sector will give access to extra information, as

Chapter 6. LHCb Silicon Tracker - Performance and monitoring

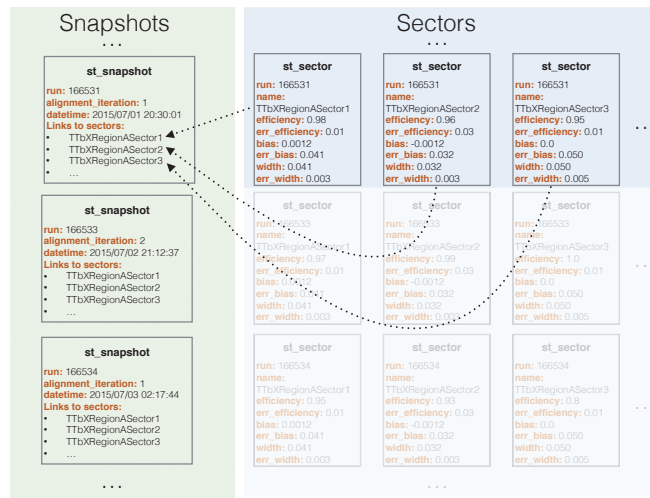


Figure 6.16 – Relation between documents in the database.

the full distributions of the all three observables will be displayed in a in pop-up window that can be maximized by clicking on the sector.

6.3. ST performance monitoring

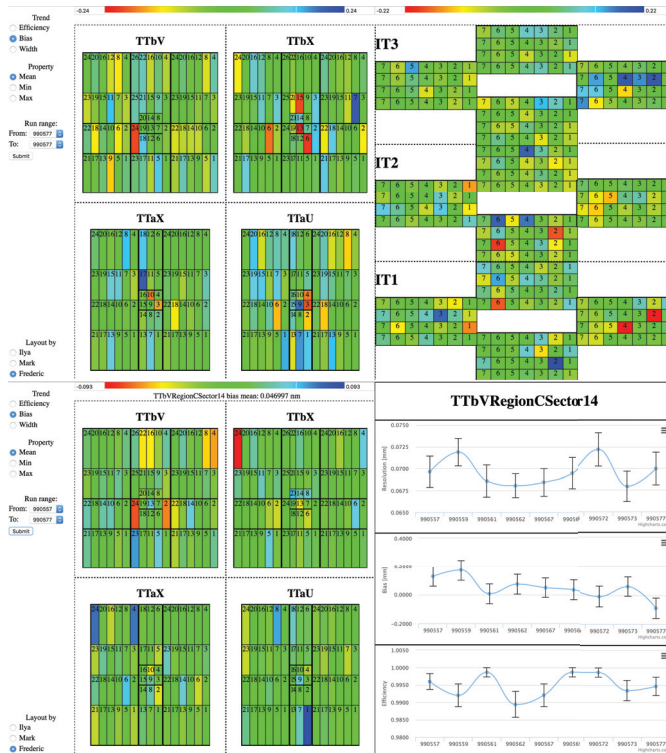


Figure 6.17 – Screen shots of the ST interactive monitor web page. Database used for these screen shots was filled with random data.

7 Conclusions and Outlook

Search for a New Physics is the chief goal of today's high energy physics. Since direct searches might be soon close to exhausting their potential for decades to come, indirect searches are increasingly more promising to probe high-energy scales. The FCNC decays of B-mesons offer among the best indirect probes. I report the first observation of the $B_s^0 \rightarrow \pi^+ \pi^- \mu^+ \mu^-$ decays and the first evidence of the $B^0 \rightarrow \pi^+ \pi^- \mu^+ \mu^-$ decays, which are governed by FCNC $b \rightarrow (s, d)$ transitions and were unobserved prior to my work. The branching ratios of these decays are measured to be $\mathcal{B}(B_s^0 \rightarrow \pi^+ \pi^- \mu^+ \mu^-) = (8.6 \pm 1.5 \text{ (stat)} \pm 0.7 \text{ (syst)} \pm 0.7 \text{ (norm)}) \times 10^{-8}$ and $\mathcal{B}(B^0 \rightarrow \pi^+ \pi^- \mu^+ \mu^-) = (2.11 \pm 0.51 \text{ (stat)} \pm 0.15 \text{ (syst)} \pm 0.16 \text{ (norm)}) \times 10^{-8}$, where the third uncertainty is due to the branching fraction of the decay $B^0 \rightarrow J/\psi (\rightarrow \mu^+ \mu^-) K^* (892)^0 (\rightarrow K^+ \pi^-)$, used for normalisation. The precision of the measurement is already superior to the precision of theoretical predictions. While our results generally agree with the SM expectations, they seem to favor phenomenological models for calculations of $B \rightarrow f_0(980)$ form-factors described in Refs. [33, 37, 38] and disfavour that described in Ref. [34]. This analysis has been published in *Physics Letters B* 743, 46 (2015).

In Run II, LHC increased the energy of the pp collisions to 13 TeV, which offers access to increased potential for direct searches, and richer opportunities for indirect searches as well, because of the increased rate of b and c mesons production. Increasing signal yields enhances sensitivity to New Physics, but a novel and complex environment requires scrupulous studies to fully exploit the physics opportunities. In this work we also report one of the first LHC results obtained at 13 TeV, the measurement of the differential production cross-section of forward J/ψ mesons, which is essential for refining the understanding of phenomenological models describing charmonium production. Along with the challenge of understanding and controlling new data-taking conditions, the stringent time scale was one of the main challenges of this analysis: its results were reported just after three weeks from the start of the data-taking, which is nearly a record time with the complex infrastructures associated with LHC experiments. Production cross-sections integrated over the kinematic coverage are found to be $15.30 \pm 0.03 \text{ (stat)} \pm 0.86 \text{ (syst)} \mu\text{b}$ for prompt J/ψ and $2.34 \pm 0.01 \text{ (stat)} \pm 0.13 \text{ (syst)} \mu\text{b}$ for J/ψ from b -hadron decays, assuming unpolarized J/ψ mesons. The results are used to infer

Chapter 7. Conclusions and Outlook

the total production cross-section of $b\bar{b}$ pairs in proton-proton collisions at 13 TeV, to be $512 \pm 2(\text{stat}) \pm 53(\text{syst}) \mu\text{b}$. The analysis has been published in *Journal of High Energy Physics* 10, 172 (2015).

Bibliography

- [1] J. Charles, Andreas Hocker, H. Lacker, S. Laplace, F. R. Le Diberder, J. Malcles, J. Ocariz, M. Pivk, and L. Roos. CP violation and the CKM matrix: Assessing the impact of the asymmetric B factories. *Eur. Phys. J.*, C41:1–131, 2005. updated results and plots available at: <http://ckmfitter.in2p3.fr>.
- [2] Brian D. Fields, Paolo Molaro, and Subir Sarkar. Big-bang nucleosynthesis. *Chin. Phys.*, C38:090001, 2014.
- [3] Roel Aaij et al. LHCb Detector Performance. *Int. J. Mod. Phys.*, A30(07):1530022, 2015.
- [4] M. Adinolfi et al. Performance of the LHCb RICH detector at the LHC. *Eur. Phys. J.*, C73:2431, 2013.
- [5] R. Aaij et al. Tesla : an application for real-time data analysis in High Energy Physics, 2016.
- [6] G Corti, Ph Charpentier, M Clemencic, J Closier, B Couturier, M Kreps, Z Mathe, D O Hanlon, P Robbe, V Romanovsky, F Stagni, and A Zhelezov. How the monte carlo production of a wide variety of different samples is centrally handled in the lhcb experiment. *Journal of Physics: Conference Series*, 664(7):072014, 2015.
- [7] Matteo Cacciari, Michelangelo L. Mangano, and Paolo Nason. Gluon PDF constraints from the ratio of forward heavy-quark production at the LHC at $\sqrt{s} = 7$ and 13 TeV. *Eur. Phys. J.*, C75(12):610, 2015.
- [8] Matteo Cacciari, Mario Greco, and Paolo Nason. The p_T spectrum in heavy flavor hadroproduction. *JHEP*, 05:007, 1998.
- [9] Roel Aaij et al. Measurements of prompt charm production cross-sections in pp collisions at $\sqrt{s} = 13$ TeV. *JHEP*, 03:159, 2016.
- [10] J Van Tilburg and M Merk. *Track simulation and reconstruction in LHCb*. PhD thesis, Vrije U. Amsterdam, Amsterdam, 2005. Presented on 01 Sep 2005.
- [11] Georges Aad et al. Observation of a new particle in the search for the Standard Model Higgs boson with the ATLAS detector at the LHC. *Phys. Lett.*, B716:1–29, 2012.

Bibliography

- [12] Serguei Chatrchyan et al. Observation of a new boson at a mass of 125 GeV with the CMS experiment at the LHC. *Phys. Lett.*, B716:30–61, 2012.
- [13] John Ellis. Outstanding questions: physics beyond the standard model. *Philosophical Transactions of the Royal Society of London A: Mathematical, Physical and Engineering Sciences*, 370(1961):818–830, 2012.
- [14] Sean Benson, Vladimir Gligorov, Mika Anton Vesterinen, and John Michael Williams. The LHCb Turbo Stream. *J. Phys.: Conf. Ser.*, 664(LHCb-PROC-2015-013. CERN-LHCb-PROC-2015-013. 8):082004. 8 p, May 2015.
- [15] F Englert and R. Brout. Broken symmetry and the mass of gauge vector mesons. *Phys. Rev. Lett.*, 13:321–323, Aug 1964.
- [16] Peter W. Higgs. Broken symmetries and the masses of gauge bosons. *Phys. Rev. Lett.*, 13:508–509, Oct 1964.
- [17] G. S. Guralnik, C. R. Hagen, and T. W. B. Kibble. Global conservation laws and massless particles. *Phys. Rev. Lett.*, 13:585–587, Nov 1964.
- [18] Jean Iliopoulos. Introduction to the Standard Model of the Electro-Weak Interactions. In *Proceedings, 2012 European School of High-Energy Physics (ESHEP 2012)*, pages 1–30, 2014.
- [19] Lincoln Wolfenstein. Parametrization of the kobayashi-maskawa matrix. *Phys. Rev. Lett.*, 51:1945–1947, Nov 1983.
- [20] Andrzej J. Buras and Robert Fleischer. Quark mixing, CP violation and rare decays after the top quark discovery. *Adv. Ser. Direct. High Energy Phys.*, 15:65–238, 1998.
- [21] S. L. Glashow, J. Iliopoulos, and L. Maiani. Weak Interactions with Lepton-Hadron Symmetry. *Phys. Rev.*, D2:1285–1292, 1970.
- [22] T Head. The lhcb trigger system. *Journal of Instrumentation*, 9(09):C09015, 2014.
- [23] Giulio Dujany and Barbara Storaci. Real-time alignment and calibration of the LHCb Detector in Run II, Apr 2015.
- [24] Torbjörn Sjöstrand, Stephen Mrenna, and Peter Skands. A brief introduction to PYTHIA 8.1. *Comput.Phys.Commun.*, 178:852–867, 2008.
- [25] D. J. Lange. The EvtGen particle decay simulation package. *Nucl. Instrum. Meth.*, A462:152–155, 2001.
- [26] LHCb. The Geant4 toolkit. <http://lhcb-release-area.web.cern.ch/LHCb-release-area/DOC/geant4/>.
- [27] Roel Aaij et al. Measurement of the track reconstruction efficiency at LHCb. *JINST*, 10(02):P02007, 2015.

-
- [28] R. Aaij et al. Measurement of form-factor-independent observables in the decay $B^0 \rightarrow K^*(892)^0 \mu^+ \mu^-$. *Phys. Rev. Lett.*, 111:191801, Nov 2013.
- [29] R. Aaij et al. Differential branching fraction and angular analysis of the decay $B^0 \rightarrow K^{*0} \mu^+ \mu^-$. *JHEP*, 1308:131, 2013.
- [30] R Aaij et al. Differential branching fraction and angular analysis of the decay $B_s^0 \rightarrow \phi \mu^+ \mu^-$. *JHEP*, 1307:084, 2013.
- [31] Run-Hui Li, Cai-Dian Lu, Wei Wang, and Xiao-Xia Wang. $b \rightarrow s$ Transition Form Factors in the PQCD approach. *Phys.Rev.*, D79:014013, 2009.
- [32] Yan-Jun Sun, Zuo-Hong Li, and Tao Huang. $b \rightarrow s$ transitions in the light cone sum rules with the chiral current. *Phys.Rev.*, D83:025024, 2011.
- [33] Pietro Colangelo, Fulvia De Fazio, and Wei Wang. $B_s \rightarrow f_0(980)$ form factors and B_s decays into $f_0(980)$. *Phys.Rev.*, D81:074001, 2010.
- [34] N. Ghahramany and R. Khosravi. Analysis of the rare semileptonic decays of B_s^0 to $f_0(980)$ and $K^*(1430)^0$ scalar mesons in QCD sum rules. *Phys.Rev.*, D80:016009, 2009.
- [35] R. Mohanta. Study of some B_s^0 to $f_0(980)$ decays in the fourth generation model. *Phys.Rev.*, D84:014019, 2011.
- [36] V. Bashiry and K. Azizi. Systematic analysis of the $B_s \rightarrow f_0 \ell^+ \ell^-$ in the universal extra dimension. *JHEP*, 1202:021, 2012.
- [37] F. Kruger and L.M. Sehgal. CP violation in the exclusive decays $B \rightarrow \pi e^+ e^-$ and $B \rightarrow \rho e^+ e^-$. *Phys.Rev.*, D56:5452–5465, 1997.
- [38] D Melikhov and N V Nikitin. Form factors for rare decays $B \rightarrow (\pi, \rho, K, K^*) l^+ l^-$ in quark model. Technical Report hep-ph/9609503, Moscow State U., Sep 1996.
- [39] P. Colangelo, F. De Fazio, Pietro Santorelli, and E. Scrimieri. QCD sum rule analysis of the decays $B \rightarrow K \ell^+ \ell^-$ and $B \rightarrow K^* \ell^+ \ell^-$. *Phys.Rev.*, D53:3672–3686, 1996.
- [40] E.O. Iltan. The Exclusive $\bar{B} \rightarrow \pi e^+ e^-$ and $\bar{B} \rightarrow \rho e^+ e^-$ decays in the two Higgs doublet model with flavor changing neutral currents. *Int.J.Mod.Phys.*, A14:4365–4394, 1999.
- [41] T.M. Aliev and M. Savci. Exclusive $B \rightarrow \pi l^+ l^-$ and $B \rightarrow \rho l^+ l^-$ decays in two Higgs doublet model. *Phys.Rev.*, D60:014005, 1999.
- [42] Jian-Jun Wang, Ru-Min Wang, Yuan-Guo Xu, and Ya-Dong Yang. Rare decays $B^+ \rightarrow \pi^+ l^+ l^-$, $\rho^+ l^+ l^-$ and $B^0 \rightarrow l^+ l^-$ in the R-parity violating supersymmetry. *Phys. Rev. D*, 77:014017, Jan 2008.
- [43] J. Beringer et al. Review of particle physics. *Phys. Rev.*, D86:010001, 2012.
- [44] R. Aaij et al. The LHCb trigger and its performance in 2011. *JINST*, 8:P04022, 2013.

Bibliography

- [45] V. V. Gligorov and M. Williams. Efficient, reliable and fast high-level triggering using a bonsai boosted decision tree. *JINST*, 8:2013P, 2013.
- [46] Johannes Albrecht, V. V. Gligorov, G. Raven, and S. Tolk. Performance of the LHCb High Level Trigger in 2012. *J. Phys. Conf. Ser.*, 513:012001, 2014.
- [47] LHCb. The stripping project. <http://lhcb-release-area.web.cern.ch/LHCb-release-area/DOC/stripping/>.
- [48] Andreas Hoecker, Peter Speckmayer, Joerg Stelzer, Jan Therhaag, Eckhard von Toerne, and Helge Voss. TMVA: Toolkit for Multivariate Data Analysis. *PoS, ACAT:040*, 2007.
- [49] Root. <https://root.cern.ch/>.
- [50] G. Punzi. Sensitivity of searches for new signals and its optimization. In L. Lyons, R. Mount, and R. Reitmeyer, editors, *Statistical Problems in Particle Physics, Astrophysics, and Cosmology*, page 79, 2003.
- [51] R. Aaij et al. Measurement of the fragmentation fraction ratio f_s/f_d and its dependence on B meson kinematics. *JHEP*, 04:001, 2013. f_s/f_d value updated in LHCb-CONF-2013-011.
- [52] LHCb. PIDCalib Package. <https://twiki.cern.ch/twiki/bin/view/LHCb/PIDCalibPackage>.
- [53] N. Nikitin, A. Popov, and D. Savrina. The EvtGen based Monte-Carlo generator model for the rare radiative leptonic B -mesons decays.
- [54] I. Komarov, N. Nikitin, and D. Savrina. The EvtGen-based model for the rare semileptonic B -decays generation.
- [55] S Tolk, J Albrecht, F Dettori, and A Pellegrino. Data driven trigger efficiency determination at LHCb. Technical Report LHCb-PUB-2014-039. CERN-LHCb-PUB-2014-039, CERN, Geneva, May 2014.
- [56] K. De Bruyn, R. Fleischer, R. Kneegjens, P. Koppenburg, M. Merk, and N. Tuning. Branching ratio measurements of B_s^0 decays. *Phys.Rev.*, D86:014027, 2012.
- [57] Y. Amhis et al. Averages of b -hadron, c -hadron, and τ -lepton properties as of summer 2014, 2014.
- [58] Muriel Pivk and Francois R. Le Diberder. sPlot: A statistical tool to unfold data distributions. *Nucl.Instrum.Meth.*, A555:356–369, 2005.
- [59] W Verkerke and D. Kirkby. The RooFit toolkit for data modeling, 2003.
- [60] R. Aaij et al. Measurement of the polarization amplitudes in $B^0 \rightarrow J/\psi K^*(892)^0$ decays. *Phys. Rev.*, D88:052002, Sep 2013.

-
- [61] H. Albrecht et al. Measurement of the polarization in the decay $B \rightarrow J/\psi K^*$. *Physics Letters B*, 340(3):217 – 220, 1994.
- [62] R. Aaij et al. Analysis of the resonant components in $B^0 \rightarrow J/\psi \pi^+ \pi^-$. *Phys. Rev.*, D87:052001, Mar 2013.
- [63] R. Aaij et al. Analysis of the resonant components in $B_s^0 \rightarrow J/\psi \pi^+ \pi^-$. *Phys. Rev. D*, 86:052006, Sep 2012.
- [64] S. S. Wilks. The large-sample distribution of the likelihood ratio for testing composite hypotheses. *Ann. Math. Statist.*, 9(1):60–62, 03 1938.
- [65] F. James and M. Roos. Minuit: A System for Function Minimization and Analysis of the Parameter Errors and Correlations. *Comput. Phys. Commun.*, 10:343–367, 1975.
- [66] B. Aubert et al. Evidence for the $B^0 \rightarrow p \bar{p} K^* (892)^0$ and $B^+ \rightarrow \eta_c K^* (892)^+$ decays and study of the decay dynamics of B meson decays into $p \bar{p} h$ final states. *Phys.Rev.*, D76:092004, 2007.
- [67] K. Abe et al. Measurements of branching fractions and decay amplitudes in $B^0 \rightarrow J/\psi K^* (892)^0$ decays. *Phys.Lett.*, B538:11–20, 2002.
- [68] C.P. Jessop et al. Measurement of the decay amplitudes and branching fractions of $B^0 \rightarrow J/\psi K^* (892)^0$ and $B^+ \rightarrow J/\psi K^+$ decays. *Phys.Rev.Lett.*, 79:4533–4537, 1997.
- [69] K. A. Olive et al. Review of particle physics. *Chin. Phys.*, C38:090001, 2014.
- [70] N. Brambilla et al. Heavy quarkonium: progress, puzzles, and opportunities. *Eur. Phys. J.*, C71:1534, 2011.
- [71] C.E. Carlson and R. Suaya. Hadronic production of the ψ/J meson. *Phys.Rev.*, D14:3115, 1976.
- [72] A. Donnachie and P.V. Landshoff. Production of lepton pairs, J/ψ and charm with hadron beams. *Nucl.Phys.*, B112:233, 1976.
- [73] S.D. Ellis, Martin B. Einhorn, and C. Quigg. Comment on hadronic production of psions. *Phys.Rev.Lett.*, 36:1263, 1976.
- [74] Harald Fritzsch. Producing heavy quark flavors in hadronic collisions: A test of quantum chromodynamics. *Phys.Lett.*, B67:217, 1977.
- [75] M. Gluck, J.F. Owens, and E. Reya. Gluon contribution to hadronic J/ψ production. *Phys.Rev.*, D17:2324, 1978.
- [76] Chao-Hsi Chang. Hadronic production of J/ψ associated with a gluon. *Nucl.Phys.*, B172:425–434, 1980.

Bibliography

- [77] R. Baier and R. Rückl. Hadronic production of J/ψ and Υ : Transverse momentum distributions. *Phys.Lett.*, B102:364, 1981.
- [78] J. P. Lansberg. J/ψ , ψ' and ψ production at hadron colliders: A Review. *Int. J. Mod. Phys.*, A21:3857–3916, 2006.
- [79] N. Brambilla et al. Heavy quarkonium physics. 2004.
- [80] Geoffrey T. Bodwin, Eric Braaten, and G. Peter Lepage. Rigorous QCD analysis of inclusive annihilation and production of heavy quarkonium. *Phys.Rev.*, D51:1125–1171, 1995.
- [81] Peter L. Cho and Adam K. Leibovich. Color-octet quarkonia production. *Phys.Rev.*, D53:150–162, 1996.
- [82] Peter L. Cho and Adam K. Leibovich. Color-octet quarkonia production. II. *Phys.Rev.*, D53:6203–6217, 1996.
- [83] F. Abe et al. Inclusive J/ψ , $\psi(2S)$ and b quark production in $\bar{p}p$ collisions at $\sqrt{s} = 1.8$ TeV. *Phys. Rev. Lett.*, 69:3704–3708, 1992.
- [84] B. Abelev et al. Inclusive J/ψ production in pp collisions at $\sqrt{s} = 2.76$ TeV. *Phys.Lett.*, B718:295–306, 2012.
- [85] R. Aaij et al. Measurement of J/ψ production in pp collisions at $\sqrt{s} = 2.76$ TeV. *JHEP*, 02:041, 2013.
- [86] R. Aaij et al. Measurement of J/ψ production in pp collisions at $\sqrt{s} = 7$ TeV. *Eur. Phys. J.*, C71:1645, 2011.
- [87] Vardan Khachatryan et al. Prompt and non-prompt J/ψ production in pp collisions at $\sqrt{s} = 7$ TeV. *Eur.Phys.J.*, C71:1575, 2011.
- [88] Georges Aad et al. Measurement of the differential cross-sections of inclusive, prompt and non-prompt J/ψ production in proton-proton collisions at $\sqrt{s} = 7$ TeV. *Nucl.Phys.*, B850:387–444, 2011.
- [89] K. Aamodt et al. Rapidity and transverse momentum dependence of inclusive J/ψ production in pp collisions at $\sqrt{s} = 7$ TeV. *Phys.Lett.*, B704:442–455, 2011.
- [90] Serguei Chatrchyan et al. J/ψ and $\psi(2S)$ production in pp collisions at $\sqrt{s} = 7$ TeV. *JHEP*, 02:011, 2012.
- [91] R. Aaij et al. Production of J/ψ and Υ mesons in pp collisions at $\sqrt{s} = 8$ TeV. *JHEP*, 06:064, 2013.
- [92] Matteo Cacciari, Stefano Frixione, Nicolas Houdeau, Michelangelo L. Mangano, Paolo Nason, et al. Theoretical predictions for charm and bottom production at the LHC. *JHEP*, 1210:137, 2012.

-
- [93] Yan-Qing Ma, Kai Wang, and Kuang-Ta Chao. Complete next-to-leading order calculation of the J/ψ and ψ' production at hadron colliders. *Phys.Rev.*, D84:114001, 2011.
- [94] Bin Gong, Xue Qian Li, and Jian-Xiong Wang. QCD corrections to J/ψ production via color-octet states at Tevatron and LHC. *Phys.Lett.*, B673:197–200, 2009.
- [95] Mathias Butenschoen and Bernd A. Kniehl. Reconciling J/ψ production at HERA, RHIC, Tevatron, and LHC with nonrelativistic QCD factorization at next-to-leading order. *Phys.Rev.Lett.*, 106:022003, 2011.
- [96] Matteo Cacciari, Mario Greco, Michelangelo L. Mangano, and Andrea Petrelli. Charmonium production at the Tevatron. *Phys.Lett.*, B356:553–560, 1995.
- [97] Eric Braaten and Sean Fleming. Color-octet fragmentation and the ψ' surplus at the Fermilab Tevatron. *Phys.Rev.Lett.*, 74:3327–3330, 1995.
- [98] M. Beneke and I.Z. Rothstein. ψ' polarization as a test of colour octet quarkonium production. *Phys.Lett.*, B372:157–164, 1996.
- [99] Kuang-Ta Chao, Yan-Qing Ma, Hua-Sheng Shao, Kai Wang, and Yu-Jie Zhang. J/ψ polarization at hadron colliders in nonrelativistic QCD. *Phys.Rev.Lett.*, 108:242004, 2012.
- [100] Bin Gong, Lu-Ping Wan, Jian-Xiong Wang, and Hong-Fei Zhang. Polarization for prompt J/ψ and $\psi(2S)$ production at the Tevatron and LHC. *Phys.Rev.Lett.*, 110:042002, 2013.
- [101] Mathias Butenschoen and Bernd A. Kniehl. J/ψ polarization at Tevatron and LHC: Nonrelativistic-QCD factorization at the crossroads. *Phys.Rev.Lett.*, 108:172002, 2012.
- [102] A. Abulencia et al. Polarization of J/ψ and $\psi(2S)$ mesons produced in $p\bar{p}$ collisions at $\sqrt{s} = 1.96$ TeV. *Phys.Rev.Lett.*, 99:132001, 2007.
- [103] V.M. Abazov et al. Measurement of the polarization of the $\Upsilon(1S)$ and $\Upsilon(2S)$ states in $p\bar{p}$ collisions at $\sqrt{s} = 1.96$ TeV. *Phys.Rev.Lett.*, 101:182004, 2008.
- [104] Betty Abelev et al. J/ψ polarization in pp collisions at $\sqrt{s} = 7$ TeV. *Phys.Rev.Lett.*, 108:082001, 2012.
- [105] Serguei Chatrchyan et al. Measurement of the prompt J/ψ and $\psi(2S)$ polarizations in pp collisions at $\sqrt{s} = 7$ TeV. *Phys.Lett.*, B727:381–402, 2013.
- [106] Serguei Chatrchyan et al. Measurement of the $\Upsilon(1S)$, $\Upsilon(2S)$ and $\Upsilon(3S)$ polarizations in pp collisions at $\sqrt{s} = 7$ TeV. *Phys.Rev.Lett.*, 110:081802, 2013.
- [107] R. Aaij et al. Measurement of J/ψ polarization in pp collisions at $\sqrt{s} = 7$ TeV. *Eur. Phys. J.*, C73:2631, 2013.
- [108] R. Aaij et al. Measurement of $\psi(2S)$ polarisation in pp collisions at $\sqrt{s} = 7$ TeV. *Eur. Phys. J.*, C74:2872, 2014.

Bibliography

- [109] S. Kullback and R.Á. Leibler. On information and sufficiency. *Ann. Math. Statist.*, 22:79, 1951.
- [110] S. Kullback. Letter to editor: the Kullback-Leibler distance. *The American Statistician*, 41:340, 1987.
- [111] M Needham. Clone Track Identification using the Kullback-Liebler Distance. Technical Report LHCb-2008-002. CERN-LHCb-2008-002. LPHE-2008-002, CERN, Geneva, Jan 2008.
- [112] Tomasz Skwarnicki. *A study of the radiative cascade transitions between the Upsilon-prime and Upsilon resonances*. PhD thesis, Institute of Nuclear Physics, Krakow, 1986. DESY-F31-86-02.
- [113] Rudolph Emil Kalman. A new approach to linear filtering and prediction problems. *Transactions of the ASME—Journal of Basic Engineering*, 82(Series D):35–45, 1960.
- [114] Wouter Donovan Hulsbergen. *A Study of Track Reconstruction and Massive Dielectron Production in Hera-B*. PhD thesis, UNIVERSITEIT VAN AMSTERDAM, Amsterdam, 2012.
- [115] Makel Rainer. Application of the kalman filter technique in the hera-b track reconstruction.
- [116] Frederic Guillaume Dupertuis. *Measurements of b-hadron lifetimes and the calibration and performance of the LHCb tracking system*. PhD thesis, EPFL, Lausanne, 2014.
- [117] LHCb. STTrackTuple class. https://lhcb-release-area.web.cern.ch/LHCb-release-area/DOC/rec/latest_doxygen/df/d02/class_s_t_track_tuple.html.
- [118] Ilya Komarov. Tuptohist package repository. <https://github.com/mozgit/tuptohist>.
- [119] Armin Ronacher et al. Flask microframework. <http://flask.pocoo.org/>.
- [120] The mongoDB. <https://www.mongodb.org/>.
- [121] LHCb. LHCb preseneter. <https://lbtwiki.cern.ch/bin/view/Online/HistogramPresenter>.

A Summary of the LHCb ST performance in 2012/2015

We report plots characterising the performance of the LHCb ST in 2012 and 2015 data-taking conditions, obtained from data and simulations. The ST performances obtained from simulation and data are compared separately for 2012 and 2015 conditions.

The performance plots are structured as $[2 \times 3]$ matrices where the left column corresponds to TT sectors, the right refers to IT, and the lines show the efficiency, bias and resolution variables.

Figures A.1 and A.2 are summary distributions of the performance variables for the ST sectors in 2015 and 2012 data-taking conditions, respectively. Each entry corresponds to the performance of a single ST sector. In Figures A.3 and A.4, these performance variables are mapped to the layout of the TT and IT sectors. The ST performance during 2012 and 2015 data-taking conditions is compared in Figures A.5. This figure contains the layouts of the ST where the z-axis is coloured and shows ratio of the hit detection efficiency, and hit resolution, measured in 2012 to that for 2015, and the difference of the absolute values of bias for these two years. Figures A.2 and A.7 show a comparison of the ST performance measured on data and that estimated from simulations.

Appendix A. Summary of the LHCb ST performance in 2012/2015

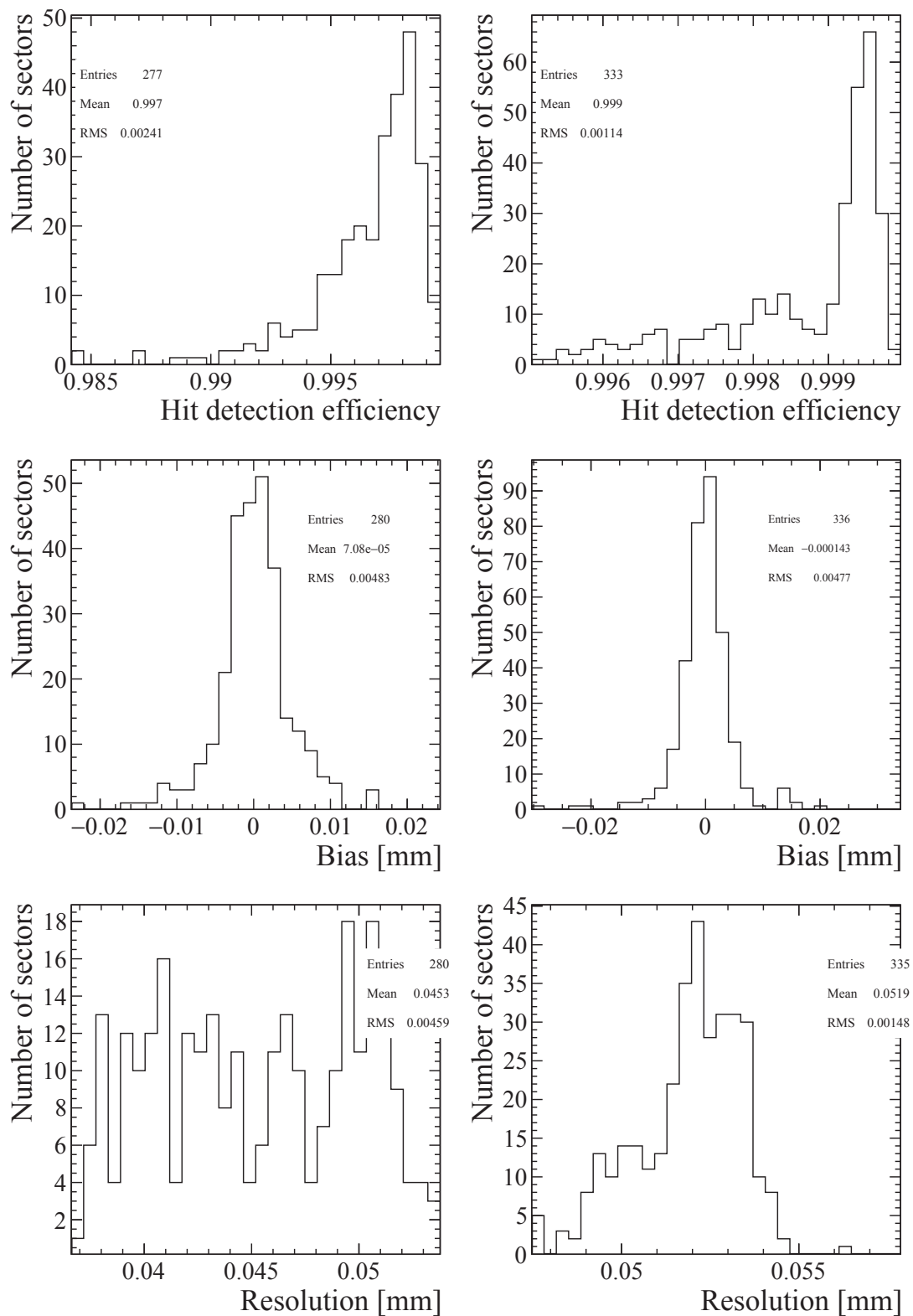


Figure A.1 – Summary distributions of the ST performance variables in 2015 for TT (left column) and IT (right column).

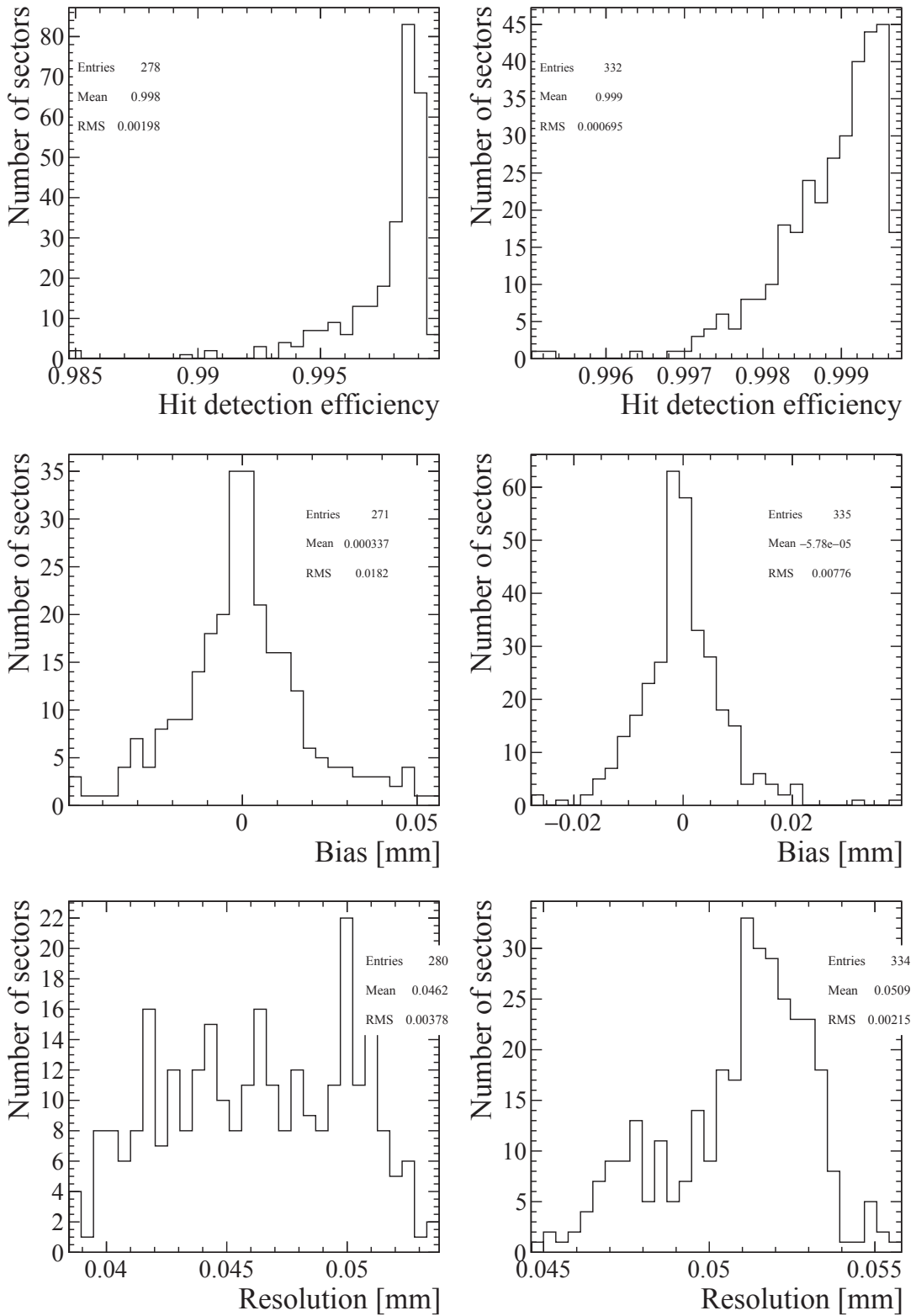


Figure A.2 – Summary distributions of the ST performance variables in 2012 for TT (left column) and IT (right column).

Appendix A. Summary of the LHCb ST performance in 2012/2015

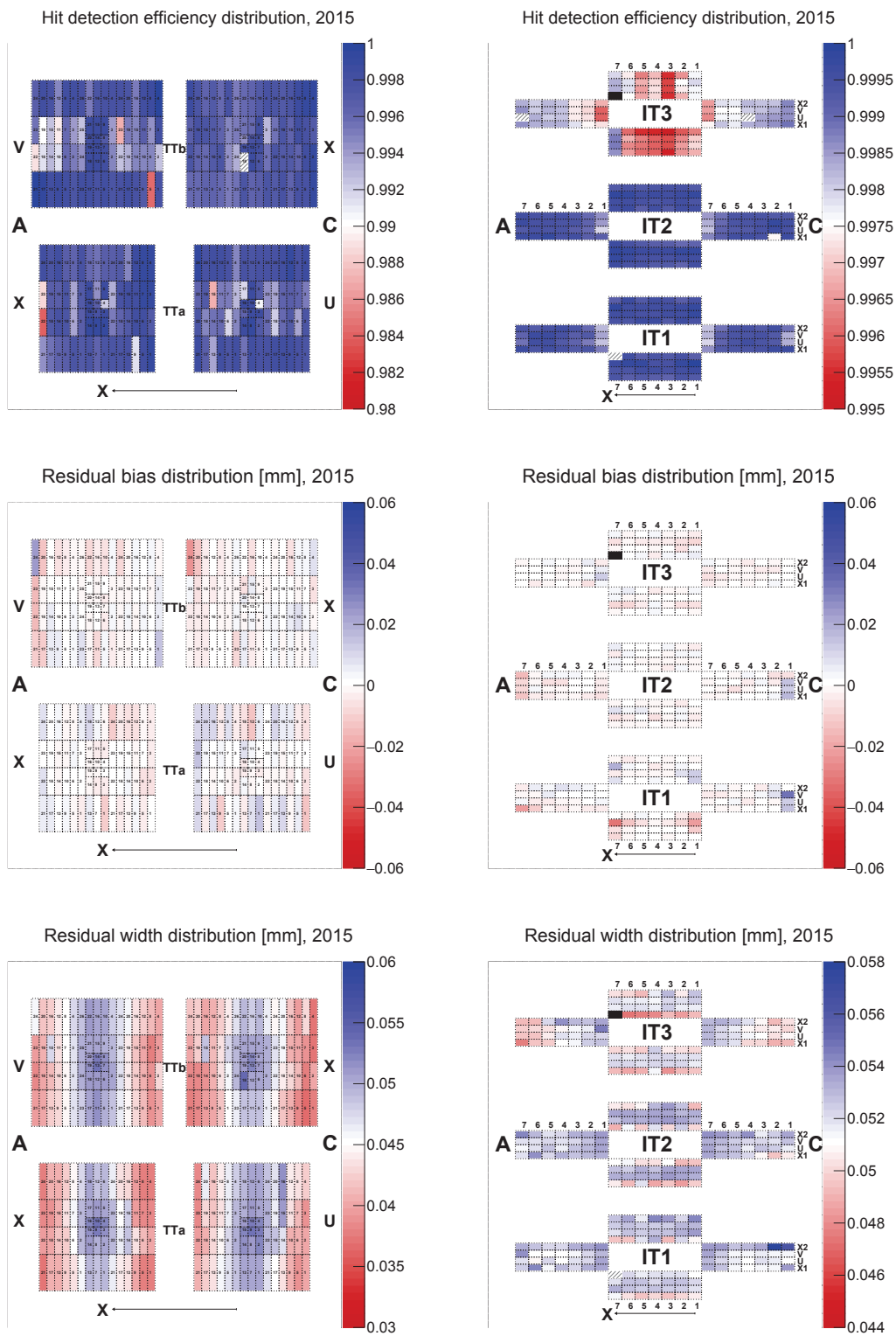


Figure A.3 – ST performance values for 2015 data-taking conditions. Hashed regions are sectors where the measured value is out of the colour scheme scale.

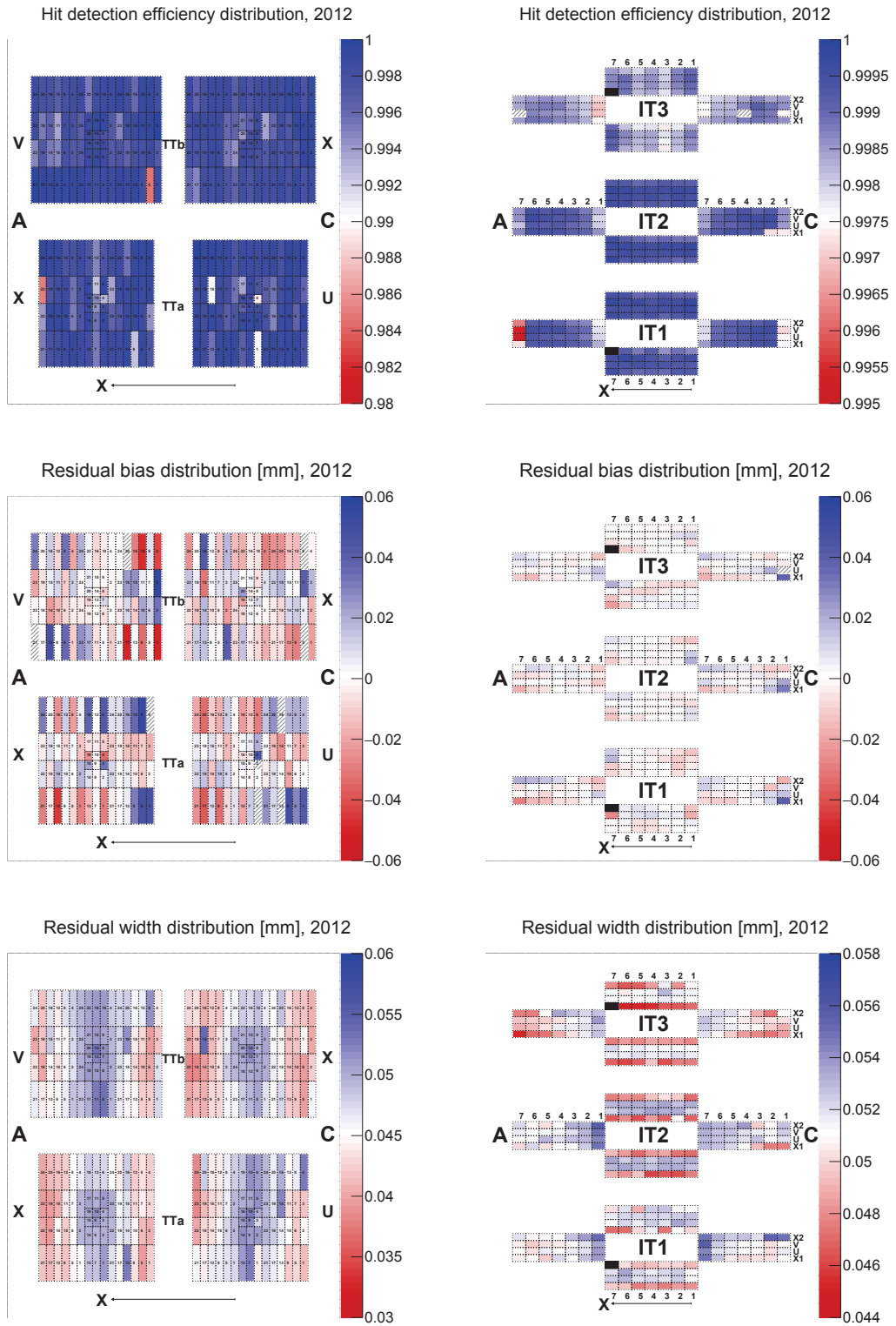


Figure A.4 – ST performance values for 2012 data-taking conditions. Hashed regions are sectors where the measured value is out of the colour scheme scale.

Appendix A. Summary of the LHCb ST performance in 2012/2015

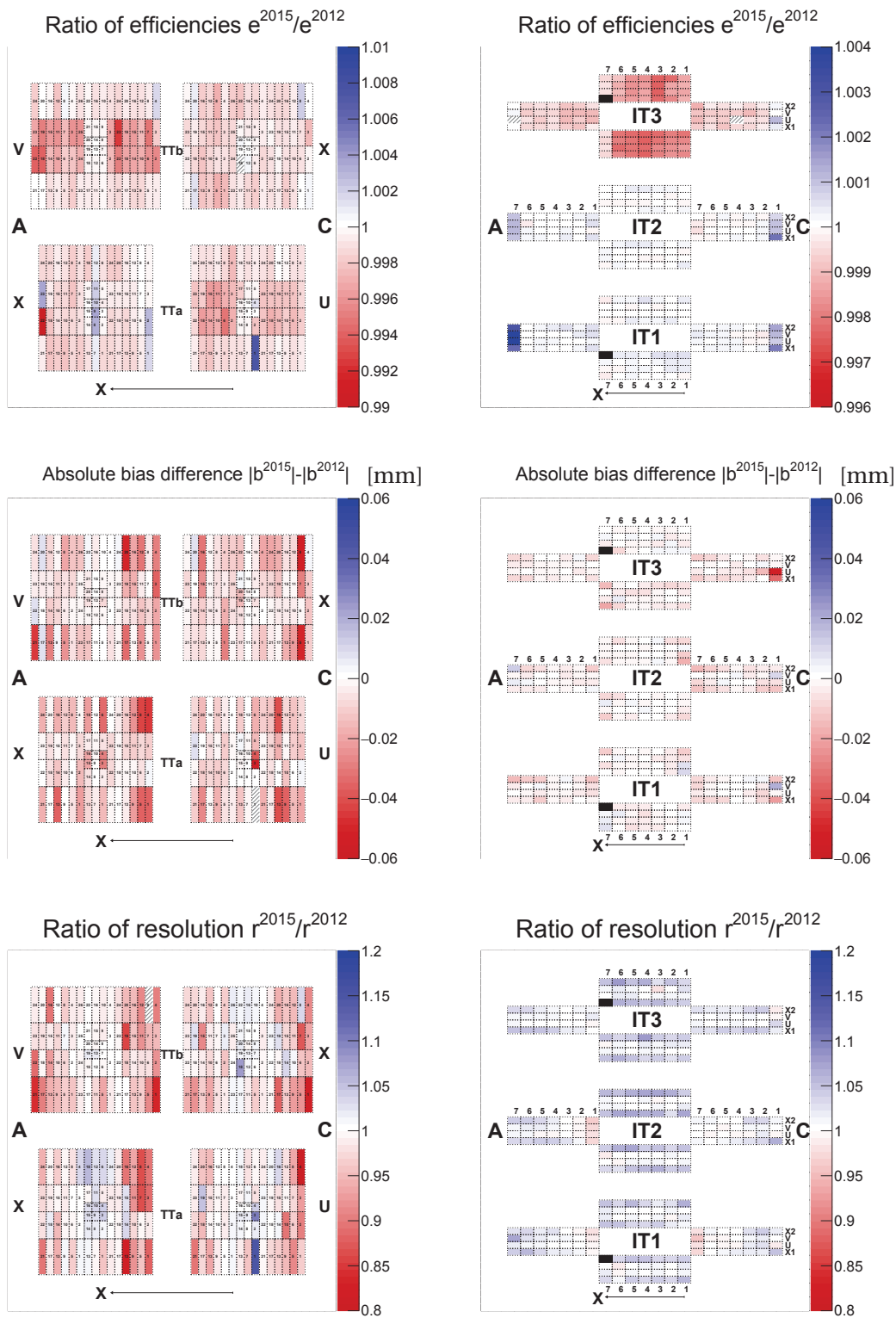


Figure A.5 – Comparison of ST performance between 2012 and 2015 data-taking conditions. Hashed regions are sectors where the measured value is out of the colour scheme scale.

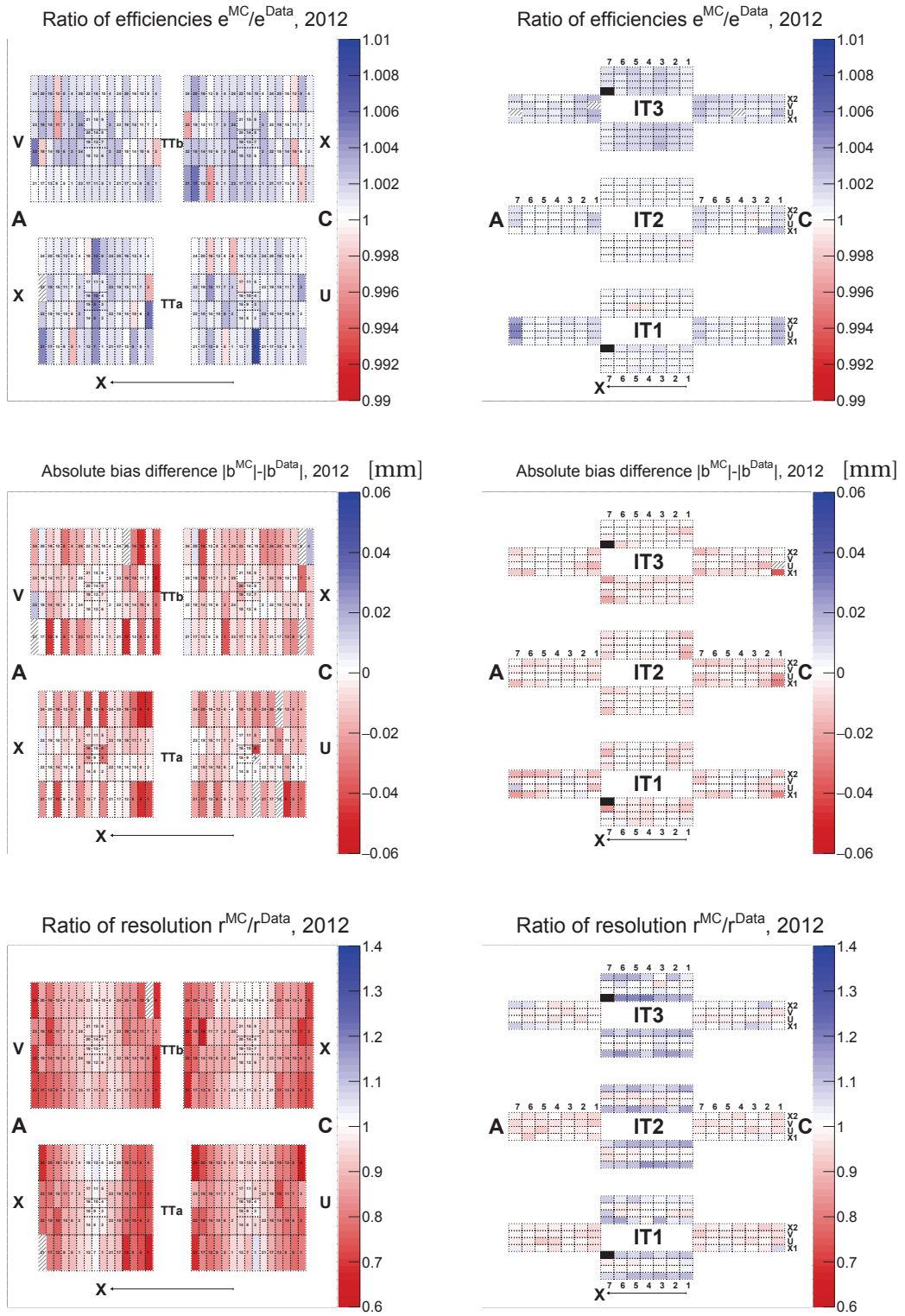


Figure A.6 – Comparison between ST performance in simulation and data for 2015 data-taking conditions. Hashed regions are sectors where the measured value is out of the colour scheme scale.

Appendix A. Summary of the LHCb ST performance in 2012/2015

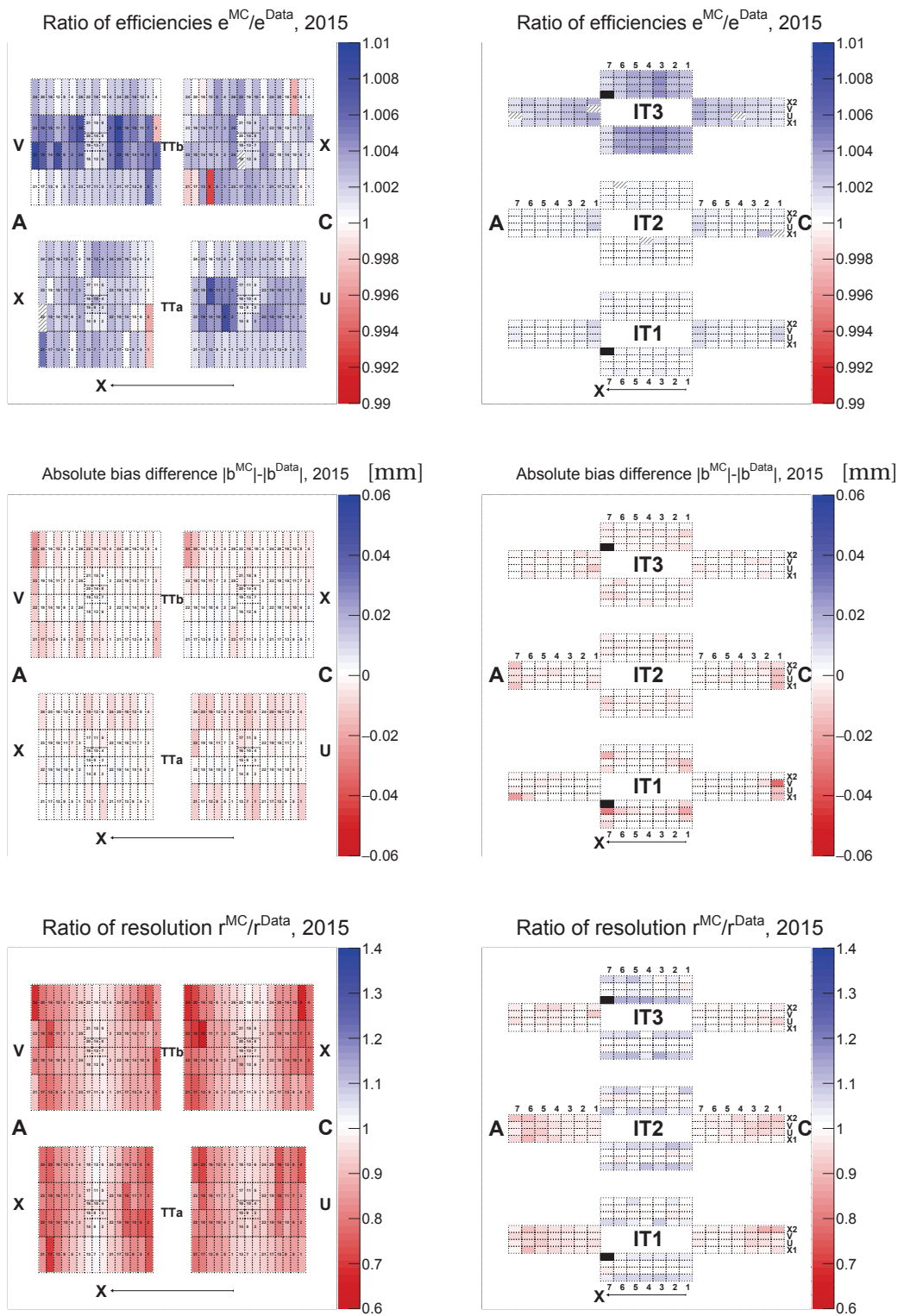


Figure A.7 – Comparison between ST performance in simulation and data for 2015 data-taking conditions. Hashed regions are sectors where the measured value is out of the colour scheme scale.

B Numerical results of the measurement of the J/ψ production cross-section

The double differential production cross-sections in bins of (p_T, y) are summarised in Table B.1 for the J/ψ -from- b mesons and in Table B.2 for the prompt J/ψ mesons. The cross-section measured at $\sqrt{s} = 13$ TeV relative to that at $\sqrt{s} = 8$ TeV is presented in Table B.3 for the J/ψ -from- b mesons and in Table B.4 for the prompt J/ψ mesons. The fraction of J/ψ -from- b mesons in bins of (p_T, y) is summarised in Table B.5.

Appendix B. Numerical results of the measurement of the J/ψ production cross-section

Table B.1 – Double differential production cross-section in bins of (p_T, y) in nb for J/ψ -from- b mesons. The first uncertainty is statistical, the second is the correlated systematic uncertainty shared between the bins and the last one is the uncorrelated systematic uncertainty.

p_T (GeV/ c)	$2.0 < y < 2.5$		$2.5 < y < 3.0$		$3.0 < y < 3.5$	
0– 1	$111.1 \pm 5.3 \pm 6.4 \pm 3.7$		$101.7 \pm 2.9 \pm 5.2 \pm 1.1$		$93.2 \pm 2.7 \pm 5.0 \pm 0.8$	
1– 2	$272.5 \pm 6.8 \pm 15.0 \pm 3.4$		$242.9 \pm 3.9 \pm 12.3 \pm 2.0$		$210.8 \pm 3.3 \pm 11.4 \pm 1.3$	
2– 3	$297.6 \pm 6.3 \pm 15.8 \pm 4.1$		$249.6 \pm 3.6 \pm 12.5 \pm 2.5$		$206.1 \pm 3.0 \pm 10.9 \pm 1.4$	
3– 4	$237.0 \pm 5.3 \pm 12.4 \pm 4.0$		$187.7 \pm 2.9 \pm 9.3 \pm 1.7$		$153.9 \pm 2.4 \pm 7.9 \pm 1.2$	
4– 5	$159.6 \pm 3.8 \pm 8.2 \pm 2.9$		$127.4 \pm 2.2 \pm 6.3 \pm 1.3$		$98.4 \pm 1.8 \pm 4.9 \pm 0.8$	
5– 6	$103.6 \pm 2.8 \pm 5.2 \pm 1.9$		$79.5 \pm 1.6 \pm 3.9 \pm 0.9$		$60.0 \pm 1.3 \pm 3.0 \pm 0.6$	
6– 7	$68.4 \pm 2.1 \pm 3.4 \pm 2.4$		$52.9 \pm 1.2 \pm 2.6 \pm 0.7$		$38.6 \pm 1.0 \pm 1.9 \pm 0.4$	
7– 8	$43.3 \pm 1.5 \pm 2.2 \pm 1.5$		$31.7 \pm 0.9 \pm 1.6 \pm 0.5$		$24.7 \pm 0.8 \pm 1.2 \pm 0.3$	
8– 9	$25.6 \pm 1.1 \pm 1.3 \pm 0.7$		$22.3 \pm 0.8 \pm 1.1 \pm 0.4$		$15.4 \pm 0.6 \pm 0.8 \pm 0.3$	
9–10	$19.2 \pm 0.9 \pm 1.0 \pm 0.7$		$13.0 \pm 0.6 \pm 0.7 \pm 0.3$		$10.4 \pm 0.5 \pm 0.5 \pm 0.2$	
10–11	$14.4 \pm 0.8 \pm 0.7 \pm 0.5$		$9.3 \pm 0.5 \pm 0.5 \pm 0.2$		$6.8 \pm 0.4 \pm 0.3 \pm 0.2$	
11–12	$9.1 \pm 0.6 \pm 0.5 \pm 0.4$		$6.9 \pm 0.4 \pm 0.4 \pm 0.2$		$4.4 \pm 0.3 \pm 0.2 \pm 0.1$	
12–13	$6.6 \pm 0.5 \pm 0.3 \pm 0.3$		$4.6 \pm 0.3 \pm 0.2 \pm 0.2$		$3.4 \pm 0.3 \pm 0.2 \pm 0.1$	
13–14	$5.0 \pm 0.4 \pm 0.3 \pm 0.3$		$3.7 \pm 0.3 \pm 0.2 \pm 0.1$		$2.5 \pm 0.2 \pm 0.1 \pm 0.1$	
	$3.5 < y < 4.0$		$4.0 < y < 4.5$			
0– 1	$84.3 \pm 2.8 \pm 5.3 \pm 0.8$		$65.9 \pm 3.8 \pm 4.7 \pm 1.1$			
1– 2	$175.9 \pm 3.3 \pm 11.4 \pm 1.2$		$131.4 \pm 4.3 \pm 10.1 \pm 2.1$			
2– 3	$170.3 \pm 2.9 \pm 10.7 \pm 1.3$		$123.1 \pm 3.8 \pm 9.5 \pm 2.2$			
3– 4	$118.3 \pm 2.3 \pm 7.0 \pm 1.0$		$86.0 \pm 3.0 \pm 6.3 \pm 1.8$			
4– 5	$77.7 \pm 1.6 \pm 4.3 \pm 0.8$		$51.3 \pm 2.0 \pm 3.4 \pm 1.4$			
5– 6	$44.8 \pm 1.2 \pm 2.4 \pm 0.5$		$28.3 \pm 1.4 \pm 1.7 \pm 0.7$			
6– 7	$27.2 \pm 0.9 \pm 1.4 \pm 0.4$		$17.5 \pm 1.0 \pm 1.0 \pm 0.4$			
7– 8	$17.6 \pm 0.7 \pm 0.9 \pm 0.3$		$10.3 \pm 0.7 \pm 0.6 \pm 0.4$			
8– 9	$9.4 \pm 0.5 \pm 0.5 \pm 0.2$		$6.2 \pm 0.5 \pm 0.3 \pm 0.3$			
9–10	$8.0 \pm 0.5 \pm 0.4 \pm 0.2$		$4.2 \pm 0.4 \pm 0.2 \pm 0.2$			
10–11	$4.7 \pm 0.3 \pm 0.2 \pm 0.1$		$3.2 \pm 0.3 \pm 0.2 \pm 0.2$			
11–12	$2.7 \pm 0.3 \pm 0.1 \pm 0.1$		$2.5 \pm 0.3 \pm 0.1 \pm 0.1$			
12–13	$1.9 \pm 0.2 \pm 0.1 \pm 0.1$		$0.9 \pm 0.2 \pm 0.1 \pm 0.1$			
13–14	$1.5 \pm 0.2 \pm 0.1 \pm 0.1$		$0.6 \pm 0.1 \pm 0.0 \pm 0.1$			

Table B.2 – Double differential production cross-section in bins of (p_T, y) in nb for prompt J/ψ mesons. The first uncertainty is statistical, the second is the correlated systematic uncertainty shared between the bins and the last one is the uncorrelated systematic uncertainty.

p_T (GeV/ c)	$2.0 < y < 2.5$	$2.5 < y < 3.0$	$3.0 < y < 3.5$
0– 1	$1039.7 \pm 16.1 \pm 44.6 \pm 31.3$	$941.4 \pm 8.9 \pm 37.8 \pm 7.9$	$865.0 \pm 7.7 \pm 39.0 \pm 4.8$
1– 2	$2049.7 \pm 21.3 \pm 87.1 \pm 17.1$	$1872.6 \pm 12.2 \pm 75.0 \pm 11.2$	$1694.7 \pm 10.2 \pm 77.2 \pm 6.2$
2– 3	$1844.9 \pm 17.8 \pm 77.3 \pm 17.2$	$1659.3 \pm 10.5 \pm 66.4 \pm 12.7$	$1442.4 \pm 8.6 \pm 63.9 \pm 5.2$
3– 4	$1210.4 \pm 12.8 \pm 50.3 \pm 14.3$	$1067.2 \pm 7.4 \pm 42.7 \pm 5.8$	$937.3 \pm 6.1 \pm 39.5 \pm 3.4$
4– 5	$753.5 \pm 8.5 \pm 30.9 \pm 9.3$	$625.8 \pm 4.8 \pm 25.0 \pm 4.3$	$532.9 \pm 4.0 \pm 21.9 \pm 2.0$
5– 6	$419.7 \pm 5.5 \pm 17.1 \pm 4.5$	$355.2 \pm 3.3 \pm 14.2 \pm 2.3$	$292.2 \pm 2.8 \pm 11.9 \pm 1.3$
6– 7	$238.2 \pm 3.7 \pm 9.6 \pm 7.4$	$191.2 \pm 2.3 \pm 7.6 \pm 1.3$	$160.2 \pm 2.0 \pm 6.5 \pm 0.9$
7– 8	$131.4 \pm 2.5 \pm 5.3 \pm 3.8$	$105.8 \pm 1.6 \pm 4.2 \pm 0.8$	$87.0 \pm 1.4 \pm 3.5 \pm 0.6$
8– 9	$76.9 \pm 1.8 \pm 3.1 \pm 1.4$	$59.3 \pm 1.2 \pm 2.4 \pm 0.6$	$49.1 \pm 1.0 \pm 2.0 \pm 0.4$
9–10	$47.6 \pm 1.4 \pm 1.9 \pm 1.1$	$36.8 \pm 0.9 \pm 1.5 \pm 0.4$	$27.8 \pm 0.8 \pm 1.1 \pm 0.3$
10–11	$29.1 \pm 1.1 \pm 1.2 \pm 0.6$	$21.0 \pm 0.7 \pm 0.8 \pm 0.4$	$17.2 \pm 0.6 \pm 0.7 \pm 0.2$
11–12	$17.2 \pm 0.8 \pm 0.7 \pm 0.5$	$13.0 \pm 0.5 \pm 0.5 \pm 0.2$	$11.2 \pm 0.5 \pm 0.4 \pm 0.2$
12–13	$11.7 \pm 0.6 \pm 0.5 \pm 0.4$	$7.7 \pm 0.4 \pm 0.3 \pm 0.2$	$6.8 \pm 0.4 \pm 0.3 \pm 0.1$
13–14	$7.4 \pm 0.5 \pm 0.3 \pm 0.3$	$5.7 \pm 0.3 \pm 0.2 \pm 0.1$	$3.9 \pm 0.3 \pm 0.2 \pm 0.1$
	$3.5 < y < 4.0$	$4.0 < y < 4.5$	
0– 1	$816.2 \pm 7.2 \pm 45.8 \pm 4.9$	$734.7 \pm 8.5 \pm 48.5 \pm 8.8$	
1– 2	$1519.3 \pm 9.5 \pm 88.0 \pm 6.0$	$1352.3 \pm 11.3 \pm 96.5 \pm 17.6$	
2– 3	$1252.4 \pm 8.2 \pm 69.5 \pm 5.1$	$1025.1 \pm 9.9 \pm 73.9 \pm 14.6$	
3– 4	$780.7 \pm 5.8 \pm 40.3 \pm 3.2$	$633.6 \pm 7.8 \pm 42.6 \pm 10.9$	
4– 5	$434.8 \pm 3.8 \pm 20.5 \pm 2.0$	$326.9 \pm 4.9 \pm 19.1 \pm 7.4$	
5– 6	$240.0 \pm 2.6 \pm 10.8 \pm 1.2$	$171.9 \pm 3.1 \pm 9.3 \pm 3.5$	
6– 7	$121.4 \pm 1.8 \pm 5.3 \pm 0.8$	$88.7 \pm 2.1 \pm 4.5 \pm 1.1$	
7– 8	$65.7 \pm 1.3 \pm 2.8 \pm 0.5$	$45.5 \pm 1.4 \pm 2.2 \pm 1.3$	
8– 9	$36.9 \pm 0.9 \pm 1.5 \pm 0.3$	$24.7 \pm 1.0 \pm 1.2 \pm 1.0$	
9–10	$20.4 \pm 0.7 \pm 0.8 \pm 0.2$	$13.3 \pm 0.7 \pm 0.6 \pm 0.4$	
10–11	$11.8 \pm 0.5 \pm 0.5 \pm 0.2$	$7.5 \pm 0.5 \pm 0.3 \pm 0.4$	
11–12	$6.9 \pm 0.4 \pm 0.3 \pm 0.1$	$4.5 \pm 0.4 \pm 0.2 \pm 0.2$	
12–13	$4.5 \pm 0.3 \pm 0.2 \pm 0.1$	$2.7 \pm 0.2 \pm 0.1 \pm 0.1$	
13–14	$2.5 \pm 0.2 \pm 0.1 \pm 0.1$	$2.1 \pm 0.2 \pm 0.1 \pm 0.1$	

Appendix B. Numerical results of the measurement of the J/ψ production cross-section

Table B.3 – The ratio of cross-sections between measurements at 13 TeV and 8 TeV in different bins of p_T and y for J/ψ -from- b mesons.

p_T (GeV/ c)	$2 < y < 2.5$	$2.5 < y < 3$	$3 < y < 3.5$	$3.5 < y < 4$	$4 < y < 4.5$
0 – 1	1.55 ± 0.25	1.42 ± 0.16	1.52 ± 0.19	1.82 ± 0.13	2.27 ± 0.23
1 – 2	1.66 ± 0.12	1.55 ± 0.10	1.56 ± 0.10	1.76 ± 0.13	1.95 ± 0.16
2 – 3	1.83 ± 0.13	1.65 ± 0.11	1.70 ± 0.11	1.88 ± 0.12	2.12 ± 0.15
3 – 4	2.03 ± 0.15	1.76 ± 0.11	1.77 ± 0.11	1.89 ± 0.13	2.33 ± 0.17
4 – 5	2.13 ± 0.18	1.88 ± 0.12	1.84 ± 0.12	2.05 ± 0.13	2.44 ± 0.20
5 – 6	2.24 ± 0.16	1.90 ± 0.13	1.91 ± 0.13	2.18 ± 0.15	2.36 ± 0.21
6 – 7	2.37 ± 0.18	2.08 ± 0.16	2.12 ± 0.15	2.26 ± 0.17	2.75 ± 0.26
7 – 8	2.34 ± 0.19	2.07 ± 0.15	2.20 ± 0.16	2.44 ± 0.19	2.81 ± 0.31
8 – 9	2.25 ± 0.21	2.19 ± 0.17	2.25 ± 0.19	2.24 ± 0.21	2.75 ± 0.37
9 – 10	2.48 ± 0.23	2.09 ± 0.17	2.31 ± 0.22	3.12 ± 0.32	3.89 ± 0.72
10 – 11	2.77 ± 0.28	2.24 ± 0.21	2.42 ± 0.23	3.34 ± 0.42	4.44 ± 0.80
11 – 12	2.64 ± 0.28	2.45 ± 0.26	2.52 ± 0.29	2.52 ± 0.36	6.87 ± 1.49
12 – 13	2.55 ± 0.31	2.15 ± 0.23	2.52 ± 0.32	2.55 ± 0.40	3.24 ± 0.80
13 – 14	2.86 ± 0.40	2.64 ± 0.32	2.90 ± 0.44	3.56 ± 0.66	3.67 ± 1.12

Table B.4 – The ratio of cross-sections between measurements at 13 TeV and 8 TeV in different bins of p_T and y for prompt J/ψ mesons.

p_T (GeV/ c)	$2 < y < 2.5$	$2.5 < y < 3$	$3 < y < 3.5$	$3.5 < y < 4$	$4 < y < 4.5$
0 – 1	1.43 ± 0.12	1.22 ± 0.08	1.19 ± 0.07	1.22 ± 0.07	1.27 ± 0.08
1 – 2	1.41 ± 0.09	1.28 ± 0.08	1.25 ± 0.07	1.26 ± 0.08	1.35 ± 0.08
2 – 3	1.50 ± 0.10	1.39 ± 0.09	1.34 ± 0.08	1.36 ± 0.08	1.37 ± 0.08
3 – 4	1.60 ± 0.11	1.45 ± 0.09	1.44 ± 0.09	1.45 ± 0.09	1.52 ± 0.10
4 – 5	1.75 ± 0.14	1.54 ± 0.09	1.49 ± 0.09	1.53 ± 0.09	1.61 ± 0.11
5 – 6	1.82 ± 0.11	1.64 ± 0.10	1.60 ± 0.10	1.65 ± 0.10	1.79 ± 0.13
6 – 7	1.89 ± 0.13	1.65 ± 0.12	1.65 ± 0.10	1.65 ± 0.10	1.84 ± 0.13
7 – 8	1.94 ± 0.15	1.68 ± 0.11	1.70 ± 0.11	1.76 ± 0.12	1.91 ± 0.15
8 – 9	1.97 ± 0.16	1.71 ± 0.12	1.80 ± 0.13	1.85 ± 0.13	2.10 ± 0.20
9 – 10	2.17 ± 0.17	1.89 ± 0.13	1.85 ± 0.15	1.86 ± 0.15	2.01 ± 0.20
10 – 11	2.15 ± 0.18	1.82 ± 0.14	1.94 ± 0.15	1.89 ± 0.17	2.23 ± 0.28
11 – 12	2.14 ± 0.19	1.79 ± 0.16	2.24 ± 0.19	1.80 ± 0.18	2.19 ± 0.30
12 – 13	2.23 ± 0.23	1.79 ± 0.16	2.05 ± 0.20	2.03 ± 0.23	2.63 ± 0.39
13 – 14	2.24 ± 0.28	1.93 ± 0.20	1.89 ± 0.22	1.69 ± 0.23	4.72 ± 0.94

Table B.5 – The fraction of J/ψ -from- b mesons (in %) in bins of the J/ψ transverse momentum and rapidity. The uncertainty is only statistical. The systematic uncertainty is negligible.

p_T (GeV/ c)	$2 < y < 2.5$	$2.5 < y < 3$	$3 < y < 3.5$	$3.5 < y < 4$	$4 < y < 4.5$
0–1	9.6 ± 0.4	9.6 ± 0.3	9.6 ± 0.3	9.0 ± 0.3	7.9 ± 0.5
1–2	11.7 ± 0.3	11.5 ± 0.2	11.0 ± 0.2	10.3 ± 0.2	8.8 ± 0.3
2–3	13.9 ± 0.3	13.1 ± 0.2	12.5 ± 0.2	12.0 ± 0.2	10.7 ± 0.3
3–4	16.4 ± 0.3	15.0 ± 0.2	14.1 ± 0.2	13.1 ± 0.2	11.9 ± 0.4
4–5	17.5 ± 0.4	16.9 ± 0.3	15.6 ± 0.3	15.1 ± 0.3	13.5 ± 0.5
5–6	19.8 ± 0.5	18.3 ± 0.3	17.0 ± 0.3	15.7 ± 0.4	14.2 ± 0.6
6–7	22.2 ± 0.6	21.6 ± 0.5	19.4 ± 0.5	18.3 ± 0.5	16.3 ± 0.9
7–8	24.8 ± 0.8	23.1 ± 0.6	22.1 ± 0.6	21.2 ± 0.7	18.5 ± 1.2
8–9	25.0 ± 0.9	27.3 ± 0.8	23.9 ± 0.8	20.2 ± 0.9	19.8 ± 1.6
9–10	28.7 ± 1.2	26.1 ± 1.0	27.3 ± 1.1	27.9 ± 1.3	23.9 ± 2.2
10–11	33.1 ± 1.5	30.6 ± 1.3	28.3 ± 1.4	28.5 ± 1.8	29.7 ± 2.8
11–12	34.6 ± 1.9	34.7 ± 1.6	27.9 ± 1.8	28.4 ± 2.2	36.1 ± 3.4
12–13	35.8 ± 2.3	37.4 ± 2.1	33.4 ± 2.2	29.1 ± 2.6	24.3 ± 4.3
13–14	40.4 ± 2.6	39.2 ± 2.4	38.1 ± 3.0	37.3 ± 3.7	21.7 ± 4.3

C Pseudo-experiments studies in searches for $B \rightarrow \pi\pi\mu\mu$ decays

Appendix C. Pseudo-experiments studies in searches for $B \rightarrow \pi\pi\mu\mu$ decays

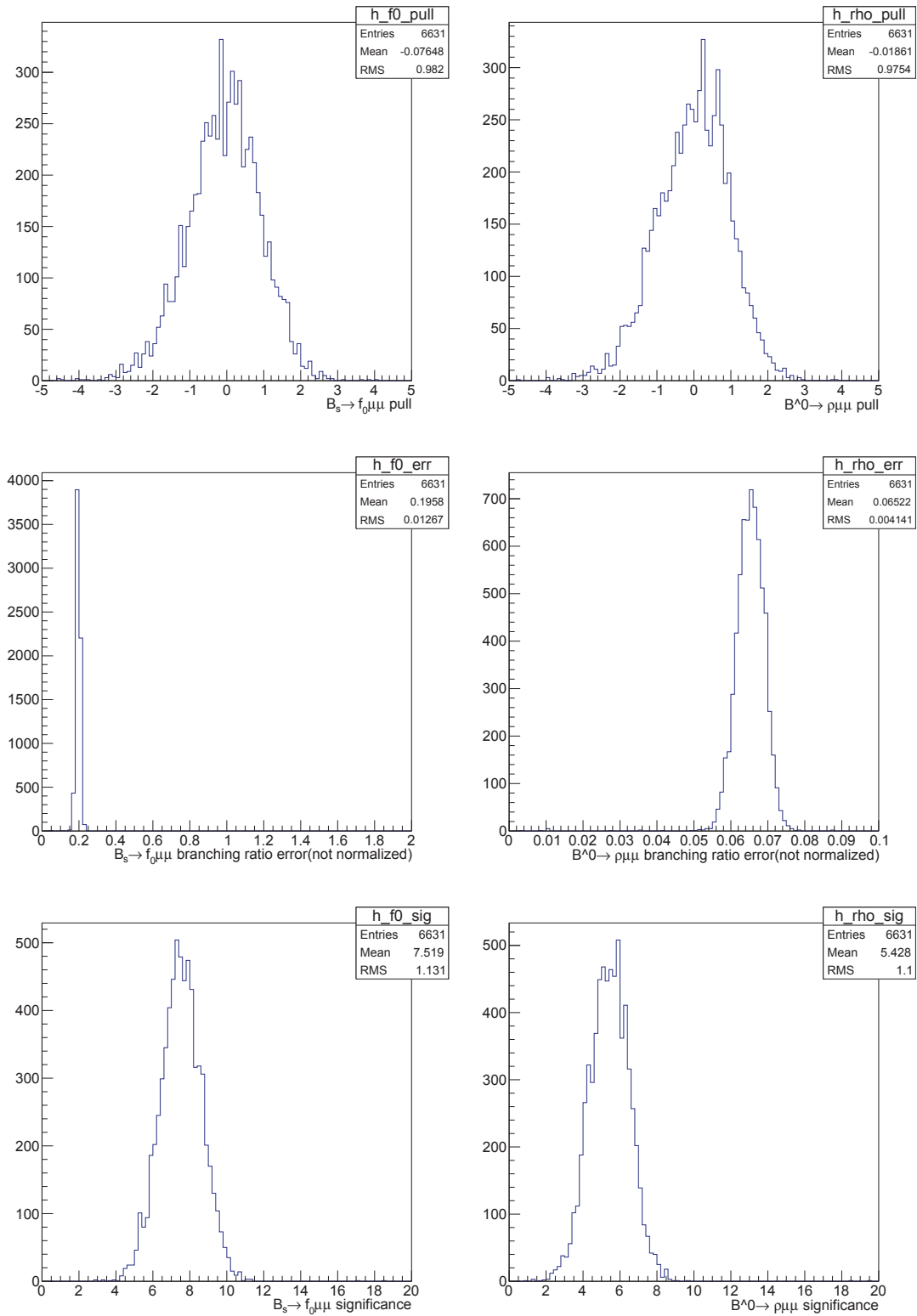


Figure C.1 – Results of pseudo-experiments generated with signal yields according to the values found in data. Distributions of pull, error and significance of B_s^0 and B^0 signals (left and right columns, respectively).

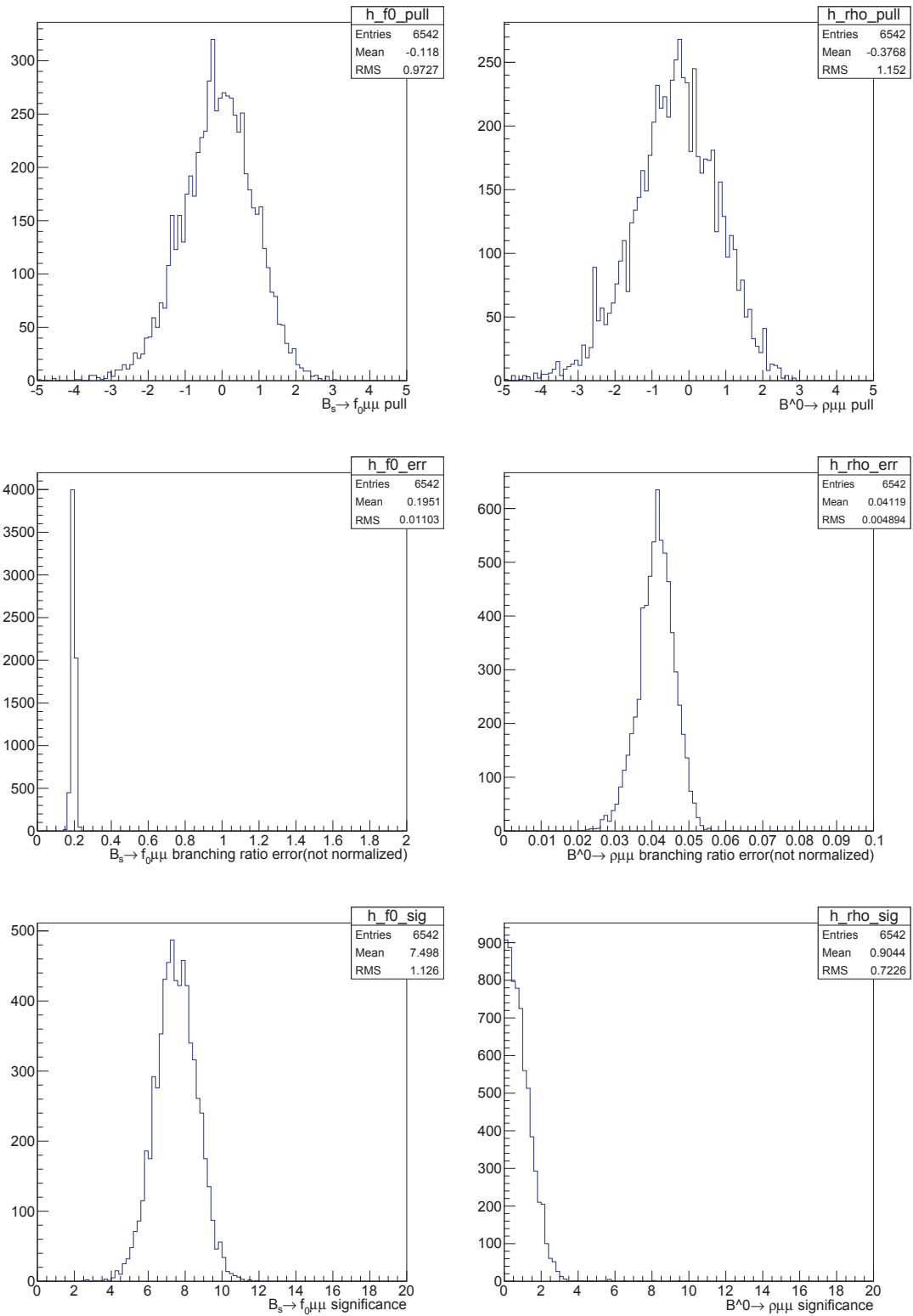


Figure C.2 – Results of pseudo-experiments generated without $B^0 \rightarrow \pi^+ \pi^- \mu^+ \mu^-$ events. Distributions of pull, error and significance of B_s^0 and B^0 signals (left and right columns, respectively).

Appendix C. Pseudo-experiments studies in searches for $B \rightarrow \pi\pi\mu\mu$ decays

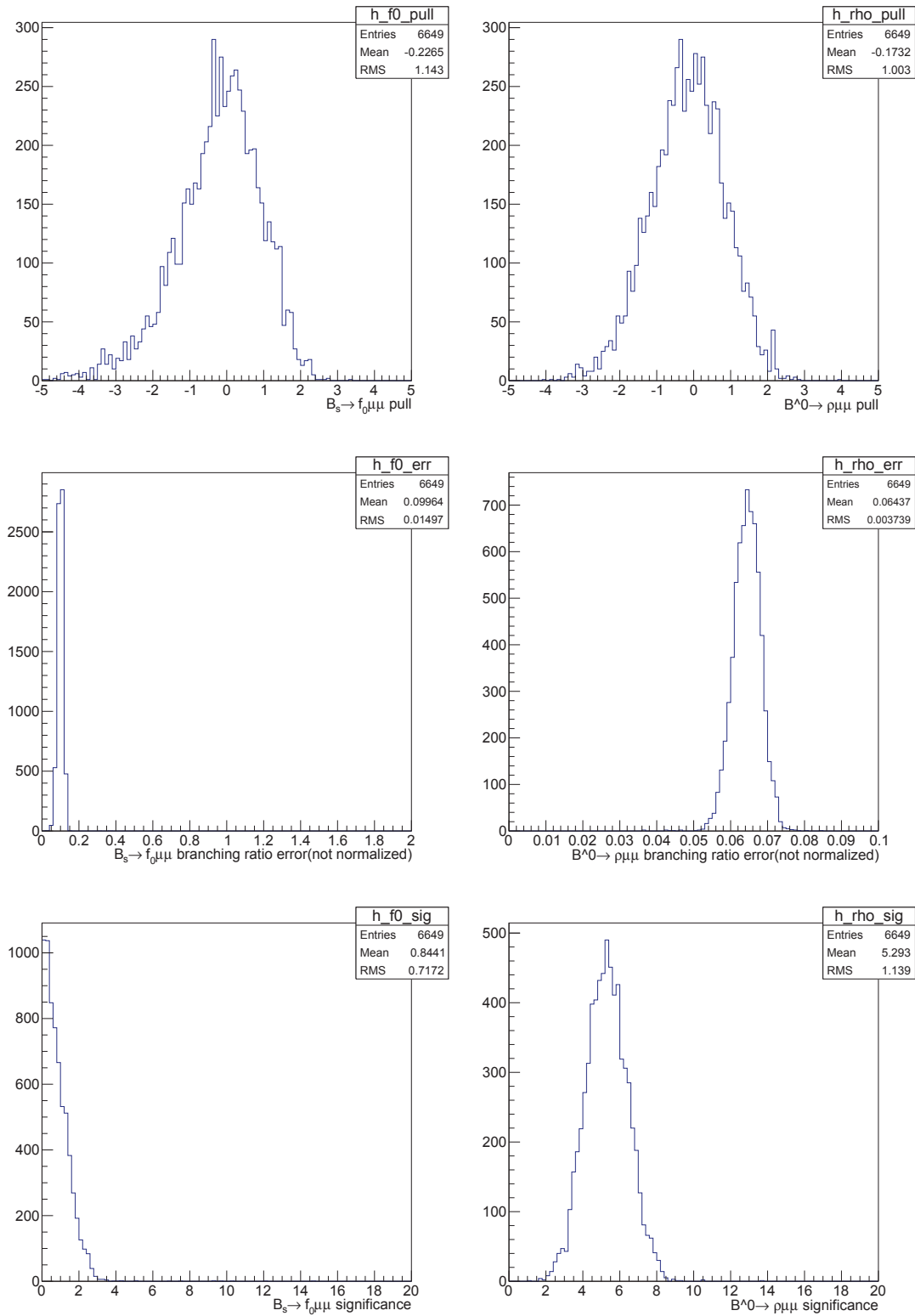


Figure C.3 – Results of pseudo-experiments without $B_s^0 \rightarrow \pi^+ \pi^- \mu^+ \mu^-$ events. Distributions of pull, error and significance of B_s^0 and B^0 signals (left and right columns, respectively).



Personal Information

ADDRESS Rue de la Boulangerie 2, 1337 Vallorbe, Switzerland
EMAIL ila.komarov@cern.ch
NATIONALITY Russian
DATE OF BIRTH 02.08.1989
LANGUAGE SKILLS English (advanced), French (intermediate), Russian (native)

Executive summary

I am a highly motivated young experimental particle physicist with extensive background and strong skills in data analysis and software development. My research focuses on the physics of the weak interactions of quarks as a probe for the new particles or interactions. I gave primary direct contributions to two high-impact papers of the LHCb collaboration at CERN, to the development of official software of the experiment and I created novel web-based projects. I am proficient in physics, statistics and programming and I have excellent problem-solving, communication, and teamwork abilities. I have conducted both independent research and research within large teams. I seek research opportunities to diversify and strengthen my background.

I am looking for a post-doctoral position to further broaden my achievements by leading or playing important roles in high-impact particle-physics measurements.

Education & experience

2012-PRESENT ÉCOLE POLYTECHNIQUE FÉDÉRALE DE LAUSANNE
POSITION Doctoral assistant (PhD in physics expected in June 2016)
QUALIFIED COURSES Statistics for Physicists, Hands-on Python, Non-LHC Physics Beyond the Standard Model, Quantum Field Theory and Renormalization Group, Silicon Photo-Detectors : theory and practice
RESPONSIBILITIES

- Analysis of experimental data from the LHCb experiment
- Development of silicon tracker software for LHCb (alignment and monitoring)
- Teaching duties
- Maintenance of laboratory web page

2009-2012 LOMONOSOV MOSCOW STATE UNIVERSITY
POSITION Laboratory assistant
DIPLOMA **Diploma with highest honours of specialist in Physics (equivalent to Master in Physics).**

Invited conference talks

LHCC OPEN SESSION	“Measurement of J/ψ and open charm cross-sections at 13 TeV” Mar 16, Geneva
OEPG2015	“Search for $B_s \rightarrow \pi\pi\mu\mu$ decays at LHCb” Sep 15, Vienna
EPS HEP	“First LHCb results from the 13 TeV LHC data” Jul 15, Vienna
LHCC OPEN SESSION	“Observation of $B_s \rightarrow \pi\pi\mu\mu$ decays at LHCb” Mar 15, Geneva
SPS	“Search for $B_s \rightarrow \pi\pi\mu\mu$ decays at LHCb” Jul 14, Fribourg
SCIENTIFIC SCHOOLS	2015 – CERN Latin-American school, Quito 2013, 2015 – CHIPP PhD Winter School, Grindelwald 2011 – CERN summer school, Geneva

Teaching experience

EXPERIMENTAL PHYSICS	Assistantship to third-year students on lab practice in nuclear physics.
TEACHING ASSISTANCE	Introductory courses of field theory (master students), basics of relativistic mechanics, and thermodynamics (first year).

Other activities

“FSTATE PROJECT”	Proposed and implemented the “ fstate ” project, a web service aimed to simplify searches on particle properties listings, providing the possibility to get decays based on user-specified final states (fstate.epfl.ch).
OUTREACH	Organisation of Physics career day, Geneva, Mar 2015 Video lecture “On irreversibility of time and Einstein’s theory”, “Experimentanium” Museum, Moscow, Oct 15 Interview “On the nature of the Universe”, “Mayak” national radio station, Jan 14

RESEARCH EXPERIENCE

My research has mainly been focusing on searches for rare decays of particles containing a bottom quark (B-mesons), which offer indirect but far-reaching sensitivity to non-Standard Model (SM) physics at energies much higher than those directly attainable.

For my master project I measured the ratio of decay branching-fractions $\text{Br}(B_s^0 \rightarrow \phi\mu^+\mu^-)/\text{Br}(B_s^0 \rightarrow \phi\mu^+\mu^-)$ using early data collected by the LHCb experiment at CERN in 2011. Being suppressed in the SM at leading order, the $B_s^0 \rightarrow \phi\mu^+\mu^-$ decay proceeds through quantum loops, where heavy non-SM particles could be exchanged, showing observable signs of their existence. The chief challenge of this analysis is the rareness of the decay, which occurs only about one per million B_s^0 mesons produced. To cope with that, I developed a selection based on computer simulation, pursued effective suppression of possible backgrounds, and implemented a sophisticated fit of the sample composition. This led to the world's most precise measurement of $\text{Br}(B_s^0 \rightarrow \phi\mu^+\mu^-)$. The method I developed was later used by the collaboration for the analysis of the full data set.

Building upon that experience, for my PhD I headed the study of the $B_{(s)}^0 \rightarrow \pi^+\pi^-\mu^+\mu^-$ decays in the LHCb data set collected in 2011 and 2012. These suppressed decays were not observed yet, and offered promising possibilities to test various QCD approaches that model the decay dynamics, in addition to offering a powerful indirect probe for non-SM physics. As the main contributor of this analysis, I worked on all its steps, from the sample selection, through the identification and suppression of backgrounds and the development of a fit model to determine the presence of signal, to the preparation of the publication. Since the decay is very rare (with about one occurrence per every billion of produced B-mesons), I developed a sophisticated selection procedure based on multivariate algorithms, developed novel data-driven techniques to control backgrounds and pursued robust and redundant validation studies. The results showed the first observation of $B_s^0 \rightarrow \pi^+\pi^-\mu^+\mu^-$ decays and the first evidence of $B^0 \rightarrow \pi^+\pi^-\mu^+\mu^-$ decays and are published in Physics Letters (Phys. Lett. B 743 (2015) 46).

In early 2015, by the end of my PhD work, LHCb was preparing for a new period of data taking at increased collision energy. It was essential to demonstrate the experiment's ability to collect data in novel conditions, thus I used this opportunity to broaden my experience in data analysis by volunteering to join the task force formed on purpose for the study of the J/ψ production cross-section in early data. The main challenge here was the need to analyse and understand, on a very short timescale, new data collected in a previously unexplored environment and reconstructed with novel software. Results of this analysis were reported just after 3 weeks of data taking, which is nearly a record time with the complex infrastructures associated with LHC experiments. Along with crucial validation information, this analysis provided novel powerful tests of QCD calculations, leading to improved precision in tests of QCD predictions. My task was to perform extensive simulation studies and thanks to my contributions I was chosen as one of the contact authors of the resulting paper now published in the Journal of High Energy Physics (JHEP 10 (2015) 172).

During my analysis work, I realised that a significant effort is spent in identifying the possible contributions to a given, specified final state, which is one of the most pressing challenges in searches for rare decays. In order to simplify this task, I developed the “fstate project”. This is a web-based application aimed at providing an automated search tool for possible background for decays studied in collider experiments. Basing on the list of known particle decays, I built a database containing all possible cascade decays and created a web interface that yield all decays that lead to any user-specified final state. The project is under beta-test and available at fstate.epfl.ch. We aim to have a stable, final, release later this year.

While the core of my expertise is the analysis of experimental data, I also contributed to hardware and operation projects. I participated in the maintenance and development of the LHCb Silicon Tracker (ST), one of the key detectors of the LHCb charged-particle tracking system. Well-understood and controlled ST performance is essential during data taking, to guarantee the quality of physics data. Therefore I have developed a software framework for analysis of efficiency and alignment of this subsystem which is routinely used by collaborators for ST studies.

PUBLICATIONS

Here I only list publications for which I gave a primary and direct contribution.

Papers:

- Measurement of the differential production cross-section of J/ψ at $\sqrt{s}=13$ TeV at LHCb experiment

JHEP 10 (2015) 172

- Search for $B_{(s)}^0 \rightarrow \pi^+\pi^-\mu^+\mu^-$ decays

Phys. Lett. B 743 (2015) 46

Public documents:

- Measurement of J/ψ and open charm cross-sections at $\sqrt{s}=13$ TeV

CERN-Poster-2016-529

- Measurement of J/ψ production cross-section in pp collisions at $\sqrt{s}=13$ TeV at LHCb

PoS(EPS-HEP2015)436

- Study of the rare B^0 and B_s^0 decays into the $\pi\pi\mu\mu$ final state at LHCb

CERN-Poster-2015-481

- Measurement of the ratio of branching fractions for $B_s^0 \rightarrow \phi\mu^+\mu^-$ and $B_s^0 \rightarrow J/\psi\phi$

LHCb-CONF-2012-003

